國立交通大學
光電工程研究所
碩士論文

金屬孔洞陣列造成增強性兆赫輻射穿透時孔洞內介質的效應

Effects of Hole material on Enhanced Terahertz Transmission through Metallic Hole Arrays

研究生：羅誠

指導老師：潘犀靈 教授

中華民國九十四年七月

金屬孔洞陣列造成增強性兆赫輻射穿透時孔洞內介質的效應

Effects of Hole material on Enhanced Terahertz Transmission through Metallic Hole Arrays

研究生： 羅 誠　　Student: Cheng Lo

指導老師：潘犀靈 教授　　Advisor: Prof. Ci-Ling Pan

國立交通大學
光電工程研究所
碩士論文

A Thesis
Submitted to Department of Photonics &
Institute of Electro-Optical Engineering
College of Electrical Engineering
National Chiao Tung University
In partial Fulfillment of the Requirements
for the Degree of
Master of Engineering
In
Electro-Optical Engineering

July 2005
Hsinchu, Taiwan, Republic of China

中華民國九十四年七月

國立交通大學

論文口試委員會審定書

本校光電工程研究所碩士班 羅誠 君

所提論文 金屬孔洞陣列造成增強性兆赫輻射穿透時孔洞內介質的效應

合於碩士資格標準、業經本委員會評審認可。

口試委員：賴暎杰　　　　趙如蘋

賴暎杰 教授　　　　趙如蘋 教授

洪勝富

洪勝富 教授

指導教授：潘犀靈

潘犀靈 教授

所　　長：賴暎杰 教授

賴暎杰 教授

系 主 任：潘犀靈 教授

潘犀靈 教授

中華民國 94 年 7 月 25 日

摘要

二維週期次波長孔洞陣列的金屬薄板(2D-MHA)可以在某些特定的兆赫頻率(THz)造成異常高的穿透，這種增強性的穿透被認為是由於入射光與在金屬與介電質之間的表面電漿極化子(SPP)發生了共振耦合。我們利用實驗與模擬研究2D-MHA中洞裡介質在穿透特性中的角色，發現當洞裡填入介電質材料時有新的現象產生，當洞裡填入UV膠時，兆赫波的穿透特徵與2D-MHA的厚度有強烈的相關，且改變2D-MHA週遭介質的穿透特質也和以往不同；當孔洞深度較深時，SPP展現出兩種不同的模態（耦合與非耦合），這也在利用時域有限差分法(FDTD)的電場模擬結果中獲得確認。

Abstract

Metal plates perforated with two-dimensional periodic arrays of sub-wavelength holes (2D-MHAs) exhibit high transmission at selective terahertz frequencies. This mechanism of the enhanced transmission characteristic is usually attributed to the resonant coupling between the incident light and surface plasmon-polaritons (SPPs) which are located at the metal-dielectric surfaces. We experimentally and numerically investigate the role of material in the holes on transmission characteristics of the 2D-MHA. New phenomena, however, appear when holes of the 2D-MHA are filled with dielectric material. We find distinctive THz transmission characteristics depending on the thickness and properties of the adjacent medium for the 2D-MHA of which holes are filled with UV-gel. For deeper holes, SPP can exhibit two distinct modes, coupled and uncoupled types as confirmed in the simulated results for the electric field using finite-difference time-domain (FDTD) algorithm.

Acknowledgement（誌謝）

碩士班兩年的日子真的很快，回顧這兩年，真的讓我成長了很多。懵懵懂懂地踏入了超快光電的領域，如今已經寫完了論文，今年似乎少了畢業的感傷，但對接下來的人生卻有著更多的期待。

首先要感謝我的指導教授潘犀靈老師，從大學專題生時就一直受到他的照顧，口試委員賴暎杰老師、趙如蘋老師、洪勝富老師在口試時所給的建議也讓我獲益良多，光電所裡謝文峰老師、許根玉老師在問題上的教導也讓我的觀念更加清晰;實驗室裡的夥伴們:專題時期就帶我的藍玉屏學姐跟黃銘傑學長，學姊教導的光學儀器、雷射知識以及對光技巧讓我受用無窮，總是被我纏著一直問問題卻都耐心替我解答的老劉學長，你是我在THz 遇到困難時最大的靠山，教我許多光學觀念的 chuck，提供良好雷射的 moya，教導我很多實驗室事務的 mika，帶領我進入 THz 領域的之揚，當初每次深夜時你的傾囊相授，讓我一步步地熟悉系統，是我碩士班最扎實的基礎，一起討論 THz 以及光子晶體卻常常找我集合的卓帆隊長，你是我心情不好時最好的傾訴對象，教導我怎麼製作液晶樣品的家任，提供我很多意見的昭遠、阿達、信穎、宇泰和已經畢業的上屆學長姊們，以及一起打拼衝刺，一起討論一起加油的同學們:跟我難兄難弟的宗翰、一起架設系統的阿隆、教我很多電腦知識的小冷、很會消失但超聰明的小壯、憨厚正直的小高、查資料超強的 cc 和多才多藝的仔仔，還有可愛的學弟妹:乃今、國騰與佳瑩，是你們讓我在實驗室有著無數歡樂的回憶;電子所楊玉麟學長在 FullWAVE 軟體上的教導，機械工廠莊師傅在樣品製作上的幫忙，都是我論文後的最大推手。

家人們的陪伴更是我最大的力量，媽媽總是無時無刻地掛念著我，回家時陪著我聊天談心，讓我可以在學業上無憂無慮地衝刺，是我最安定的力量，大姐、二姐、姊夫你們都是我最親愛的家人，當然還有詩敏，每天跟妳講電話以及每次的見面都是我最快樂的時光，這麼多年來的關懷與包容是我最溫暖的寶貝。

接下來的人生或許更加辛苦，但我會帶著你們滿滿的祝福開心地走下去!

羅誠　2005 年 7 月 于新竹交大

Contents

List of Figures

1 Introduction

Every region of frequency domain is a treasury in nature. The terahertz region of the electromagnetic spectrum ranges from frequencies of about 100 GHz to 10 THz (10 x 10^{12} Hz) as shown in Fig. 1-1 has wide and unexplored applications. This corresponds to wavelengths between about 3 and 0.03 mm, and lies between the microwave and infrared regions of the spectrum. At lower frequencies, microwaves and millimeter-waves can be generated by "electronic" devices such as those components in mobile phones. At higher frequencies, near-infrared or visible light is generated by "optical" devices such as semiconductor lasers, in which electrons emit light when they jump across the semiconductor band gap. Unfortunately, neither electronic nor optical devices cannot conveniently make work in the terahertz region because the terahertz frequency range sits between the electronic and optical regions of the electromagnetic spectrum.

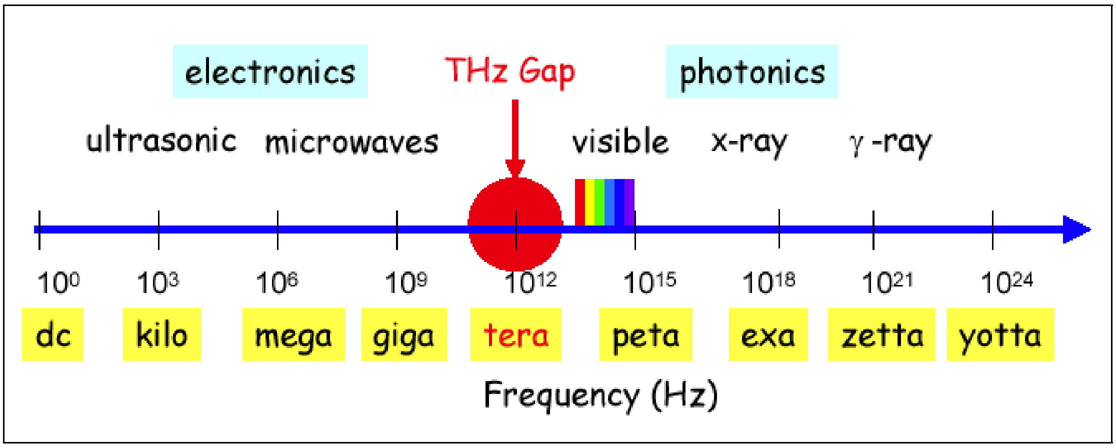

Fig. 1-1 Electromagnetic spectrum. The terahertz region ranges from frequencies of about 100 GHz to 10 THz.

Refer to http://www.wse.jhu.edu/~cmsd/Thz/

This situation changed in the 80's with the appearance of ultrashort pulse lasers of about 100 femtosecond pulse duration. Ultrashort pulses can generate broadband THz radiation when they impinge on semiconductors. Mourou and Auston et al. first demonstrated generation and detection of pulsed THz radiation by photoconducting switch with advantages of time resolution of picosecond and sensitivity enhanced by phase-lock technique [1-2]. In 1996, Zhang et al. developed free-space electro-optic sampling (FS-EOS) technique to enhance signal to noise ratio (S/N ratio) up to 10000 and to achieve much large dynamic range [3]. These techniques have now developed to a level for spectroscopy and sensing. The spectroscopic technique using pulsed THz radiation is called "THz time-domain spectroscopy (THz-TDS)" [4].

On the other hand, microstructured devices, such as dichroic filters [5], terahertz plasmonic filters [6], and terahertz photonic crystals [7] have received growing interests. These frequency-selective components play an important role in the development of terahertz technology. In 1998, Ebbesen et al. first explored extraordinary transmission of light in optical frequencies through a metal film perforated by an array of sub-wavelength holes (MHA) [8]. Many researchers have paid much great concentration on this field. Since the period of hole arrays must lie on the order of wavelength, so the most difficult challenge to studying periodical hole array is the manufacture in visible light. Fortunately, the wavelength in THz region is much longer than visible light. For this reason, it is much easier to fabricate periodical hole arrays in THz region. Furthermore, the loss of metal in THz region is negligible so metals are good candidates for periodical hole arrays [9].

However, theories to describe this phenomenon are still ambiguous. The most scientists consider these unusual phenomena are caused by the coupling between the incident waves and the surface plasmon polaritons (SPPs) [10]. Base on the theory of SPPs, the maximum transmittance peak should to be independent of the hole's diameter and the material stuffed with the holes [11]. However, in our experimental results, when the holes filled with the UV-gel, the number of the transmittance peak is changed from single to multeity, and the peak frequency will change with the thickness of the samples. Further, we attach translucent ScotchTM tapes on the incident side of MHA filled with UV-gel. Peaks shift to the left and decrease as the SPP resonances approach the cutoff frequencies. These phenomena are analogous with previous reports elucidated in terms of the SPP [12]. However, upon increasing the number of the tape, a side peak on the high frequency side grew gradually and red-shifted. For the number of tapes up to fifteen layers, the trend of shift still persists. We also discovered that different peaks have different SPP-like surface wave modes as confirmed in the simulated results using Finite-Difference Time-Domain (FDTD) for the electric field. These findings are important for understanding the fundamental mechanisms of enhanced transmission and will be vital in designing devices based on this effect.

2 Basic Theories and Conceptions

2.1 Terahertz (THz) Field

Terahertz (THz) fields is a generic term for electromagnetic waves with a spectrum between 0.1 and 10 THz (where 1 THz is 10^{12} cycles/second). From the viewpoint of wavelength, it includes millimeter and submillimeter waves. THz signals were until recently an almost unexplored area of research due to the difficulties in generation and detection of electromagnetic fields at these wavelengths. The use of ultrafast lasers to generate subpicosecond pulses of electromagnetic radiation, THz pulses, has evolved into a very active research field during the past two decades. In the other hand, THz detection is also a quite difficult work since the power of emitted THz signals is weak. Owning to the high signal-to-noise ratio, the use of photoconductive antennas to detect THz wave is a very popular method.

2.1.1 Generation of THz Radiation Using Photoconductive Antennas

When the photoconductive antenna is illuminated by ultrashort optical pulse, where the photon energy is greater than the bandgap of the semiconductor, a planar photoconductor absorbs the incident light, coherently exciting free electron-hole pairs. Photo carrier acceleration results from an applied bias on the electrodes, which produces a transient surface current. The expression can be described from the current-surge model [13].

Current-surge model:

Initially, the radiating source is defined as time-varying parameter, including charge density $\rho(x,y,z,t)$, current density $\vec{J}(x,y,z,t)$, electric field $\vec{E}(x,y,z,t)$, or magnetic flux $\vec{B}(x,y,z,t)$. And then, it is necessary to construct Maxwell's equation before deducing current-surge model.

Maxwell's equation:

$$\nabla \times \vec{E} = -\frac{\partial \vec{B}}{\partial t} \qquad \text{(Faraday's Law)} \tag{2.1.1}$$

$$\nabla \cdot \vec{E} = \frac{\rho}{\varepsilon} \qquad \text{(Gauss' Law)} \tag{2.1.2}$$

$$\nabla \times \vec{H} = \vec{J} + \frac{\partial \vec{D}}{\partial t} \qquad \text{(Ampere's Law)} \tag{2.1.3}$$

$$\nabla \cdot \vec{B} = 0 \tag{2.1.4}$$

From (2.1.1) and

$$\vec{B} = \nabla \times \vec{A} \tag{2.1.5}$$

$$\nabla \times \vec{E} = -\frac{\partial \vec{B}}{\partial t} = -\frac{\partial}{\partial t}\left(\nabla \times \vec{A}\right) = \nabla \times \left(-\frac{\partial \vec{A}}{\partial t}\right)$$

$$\Rightarrow \nabla \times \left(\vec{E} + \frac{\partial \vec{A}}{\partial t}\right) = 0 \tag{2.1.6}$$

And then, some non-vector value, V, is induced in the equation.

From (2.1.6)

$$\text{Set } -\nabla V = \vec{E} + \frac{\partial \vec{A}}{\partial t} \tag{2.1.7}$$

$$\text{And then, } \nabla \times \left(-\nabla \vec{A}\right) = 0 \tag{2.1.8}$$

From (2.1.7),

$$\vec{E} = -\nabla V - \frac{\partial \vec{A}}{\partial t} \tag{2.1.9}$$

Next, the two inhomogeneous wave equations written in terms of A and V could also be deduced from the inhomogeneous Maxwell equations:

From (2.1.3),

$$\nabla \times \vec{H} = \vec{J} + \frac{\partial \vec{D}}{\partial t}$$

$$\Rightarrow \frac{\nabla \times \vec{B}}{\mu} = \vec{J} + \varepsilon \frac{\partial \vec{E}}{\partial t} \tag{2.1.10}$$

As $\vec{H} = \frac{\vec{B}}{\mu}$ and $\vec{D} = \varepsilon \vec{E}$

From (2.1.10), (2.1.5) and (2.1.9) can be written as

$$\nabla \times \left(\nabla \times \vec{A}\right) = \mu\left(\vec{J} + \varepsilon \frac{\partial \vec{E}}{\partial t}\right) = \mu\left[\vec{J} + \varepsilon \frac{\partial}{\partial t}\left(-\nabla V - \frac{\partial \vec{A}}{\partial t}\right)\right] \tag{2.1.11}$$

$$\begin{aligned} &\nabla\left(\nabla \cdot \vec{A}\right) - \nabla^2 \vec{A} = \mu \vec{J} - \nabla\left(\mu\varepsilon \frac{\partial V}{\partial t}\right) - \mu\varepsilon \frac{\partial^2 \vec{A}}{\partial t^2} \\ &\Rightarrow \nabla^2 \vec{A} - \mu\varepsilon \frac{\partial^2 \vec{A}}{\partial t^2} = -\mu \vec{J} + \nabla\left(\nabla \cdot \vec{A} + \mu\varepsilon \frac{\partial V}{\partial t}\right) \end{aligned} \tag{2.1.12}$$

From (2.1.2),

$$\nabla \cdot \vec{D} = \rho$$

$$\Rightarrow \nabla \cdot \left(\varepsilon \vec{E}\right) = -\nabla \cdot \left[\varepsilon\left(\nabla V + \frac{\partial \vec{A}}{\partial t}\right)\right] = \rho \tag{2.1.13}$$

$$\Rightarrow \nabla^2 V + \frac{\partial}{\partial t}\left(\nabla \cdot \vec{A}\right) = -\frac{\rho}{\varepsilon}$$

Set $\nabla \cdot \vec{A} + \varepsilon\mu \frac{\partial V}{\partial t} = 0$ (Lorentz gauge) (2.1.14)

So that, (2.1.12) becomes as

$$\nabla^2 \vec{A} - \mu\varepsilon \frac{\partial^2 \vec{A}}{\partial t^2} = -\mu \vec{J} \tag{2.1.15}$$

From (2.1.14), $\nabla \cdot \vec{A} = -\mu\varepsilon \frac{\partial V}{\partial t}$

As a result, (2.1.13) can be written as

$$\nabla^2 V - \mu\varepsilon \frac{\partial^2 V}{\partial t^2} = -\frac{\rho}{\varepsilon} \tag{2.1.16}$$

Finally, the two inhomogeneous wave equations expressed in (2.1.15) and (2.1.16) are demonstrated. These equations here are used to determine a functional, time dependent form of the radiated electric field in the far field.

From (2.1.3), the continuity equation of the free carriers, which is generated in the biased semiconductor after the absorption of an optical pulse, is obtained.

$$\nabla\cdot\left(\nabla\times\vec{H}\right)=\nabla\cdot\left(\vec{J}+\frac{\partial\vec{D}}{\partial t}\right)=\nabla\cdot\vec{J}+\frac{\partial\rho}{\partial t}=0 \tag{2.1.17}$$

Actually, the current in the bias photoconductor is a transverse current, which is parallel to the surface of the photoconductor and perpendicular to the direction of propagation, so that

$$\nabla\cdot\vec{J}=0 \tag{2.1.18}$$

Equation (2.1.17) and (2.1.9) imply that the charge density dose not vary in time and not contribute to the time-dependent radiated electric field. As a result, from (2.1.9) the electric field is

$$\vec{E}_{rad}(t)=-\frac{\partial}{\partial t}\vec{A}(t) \tag{2.1.19}$$

The solution to the wave equation (2.1.15) and hence for the vector potential $\vec{A}$ leads to the expression for the time-dependent radiated electric field $\vec{E}_{rad}=(\vec{r},t)$ at a displacement $\vec{r}$ from the center of the photoconductor:

$$\vec{E}_{rad}(\vec{r},t)=-\frac{1}{4\pi\varepsilon_0 c^2}\frac{\partial}{\partial t}\int\frac{J_s\left(\vec{r}\,',t-\frac{|\vec{r}-\vec{r}\,'|}{c}\right)}{|\vec{r}-\vec{r}\,'|}da' \tag{2.1.20}$$

where ε_0 is the permittivity of free space, c is the speed of light in vacuum, $\vec{J}_s$ is the surface current in the photoconductor evaluated at the retarded time, and da' is the increment of surface area at a displacement $\vec{r}'$ from the center of the emitter. Integration is taken over the optically illuminated area of the photoconductor. In the far field,

$$|\vec{r}-\vec{r}'| = r\left(1-\frac{\hat{n}\cdot\vec{r}'}{r}\right) \approx r \tag{2.1.21}$$

At the same time, the gap between the electrodes of the photoconductor is assumed to be uniformly illuminated by the optical Therefore, the surface current $\vec{J}_s$ can be assumed to be constant at all points on the surface of the emitter. And then, the radiated electric field can be written as

$$\vec{E}_{rad}(\vec{r},t) = -\frac{1}{4\pi\varepsilon_0 c^2}\frac{A}{\left(x^2+y^2+z^2\right)^{1/2}}\frac{d}{dt}\vec{J}_s\left(t-\frac{r}{c}\right), \tag{2.1.22}$$

where A is the illuminated area of the emitter. It is considered that the radiation emitted (and detect) on axis (i.e. x=y=0), and let $t \to t-\left(\frac{z}{c}\right)$. Thus,

$$\vec{E}_{rad}(\vec{r},t) \cong -\frac{1}{4\pi\varepsilon_0 c^2}\frac{A}{z}\frac{d}{dt}\vec{J}_s(t) \tag{2.1.23}$$

There is a result for the surface current

$$\vec{J}_s(t) = \frac{\sigma_s \vec{E}_b}{\dfrac{\sigma_s(t)\eta_0}{1+n}+1} \tag{2.1.24}$$

where n is the index of refraction of the photoconductor at submillimeters, η_0 is the impedance of free space which is equal to 377Ω, and the surface conductivity defined as

$$\sigma_s = \frac{e(1-R)}{\hbar\omega}\int_{-\infty}^{t} dt' m(t,t') I_{opt}(t') \exp\left[\frac{-(t-t')}{\tau_{car}}\right] \tag{2.1.25}$$

where e is the electric charge, R is the optical reflectivity of the photoconductor, $\hbar\omega$ is the photon energy , $m(t,t')$ is the carrier mobility at time t of a carrier created at time t' , I_{opt} is the time-dependent optical intensity, and τ_{car} is the lifetime of the excited carriers. For the present derivation, a constant carrier mobility is assumed:

$$m(t,t') = m \tag{2.1.26}$$

Also, the carrier lifetime is long, i.e. $\tau_{car} \rightarrow \infty$. Finally a Gaussian intensity profile of the optical beam is assumed:

$$I_{opt}(t') = I_0 \exp\left(\frac{-t'^2}{\tau^2}\right). \tag{2.1.27}$$

With these assumption s the surface conductivity becomes

$$\sigma_s = \frac{e(1-R)}{\hbar\omega} I_0 \int_{-\infty}^{t} dt' m \exp\left(\frac{-t'^2}{\tau^2}\right) \tag{2.1.28}$$

Equations (2.1.23), (2.1.24), and (2.1.28) lead to the expression

$$\vec{E}_{rad}(t) = -\frac{\vec{E}_b}{4\pi\varepsilon_0 c^2} \frac{A}{z} \frac{e(1-R)}{\hbar\omega} I_0 m \exp\left(\frac{-t^2}{\tau^2}\right) \times \left[1 + \frac{\eta_0 e(1-R) I_0 m}{(n+1)\hbar\omega} \int_{-\infty}^{t/\tau} \tau \exp(-x^2) dx\right]^{-2} \tag{2.1.29}$$

As the comparison with the result from experiment, it is necessary to rewrite the equation in terms of the experimental parameters E_b, the bias electric field applied across the photoconductor, and F_{opt}, the incident optical fluence, which is defined as

$$F_{opt} = \int_{\infty}^{-\infty} I_0 \exp\left(\frac{-t^2}{\tau^2}\right) dt = \sqrt{\pi} I_0 \tau \equiv \frac{E_{opt}}{A} \tag{2.1.30}$$

where E_{opt} is the average optical energy and A is the area of the optical beam, where r is the measured $\frac{1}{e}$ radius of the optical beam. Set

$$B = \frac{Ae(1-R)m}{4\pi\varepsilon_0 c^2 z\hbar\omega\sqrt{\pi}} \qquad (\mathrm{m}^2 s/J) \tag{2.1.31}$$

$$D = \frac{\eta_0 e(1-R)m}{(n+1)\hbar\omega\sqrt{\pi}} \qquad (\mathrm{m}^2/J). \tag{2.1.32}$$

And then, the electric field in the far field can be written as

$$E_{rad}(t) = -BE_b \frac{F_{opt}}{\tau} \exp\left(\frac{-t^2}{\tau^2}\right) \times \left[1 + DF_{opt} \int_{-\infty}^{t/\tau} \exp(-x^2)dx\right]^{-2}. \tag{2.1.33}$$

We can also discuss on the viewpoint of the carrier dynamics in semiconductor to analyze the THz generation by Drude-Lorentz model when using the photoconductive antenna [14, 15].

Drude-Lorentz model:

When a biased semiconductor is pumped by a laser pulse with photon energies greater than the band gap of the semiconductor, electrons and holes are created in the conduction band and valence band, respectively. The time dependence of carrier density is given by the following equation:

$$\frac{dn}{dt} = -\frac{n}{\tau_c} + G \tag{2.1.34}$$

where n is the density of the carrier, G is the generation rate of the carrier by the laser pulse, and τ_c is the carrier trapping time. The generated carriers will be accelerated in the bias electric field. The acceleration of electrons (holes) in the electric field is given by

$$\frac{dv_{e,h}}{dt} = -\frac{v_{e,h}}{\tau_s} + \frac{q_{e,h}}{m_{e,h}} E \tag{2.1.35}$$

where $v_{e,h}$ is the average velocity of the carrier, $q_{e,h}$ is the charge of an electron (a hole), $m_{e,h}$ is the effective mass of the electron (hole), τ_s is the momentum relaxation time, and E is the local electric field. The subscripts e and h represent electron and hole, respectively. The local electric field E is smaller than the applied bias electric field, E_b, due to the screening effects of the space charges,

$$E = E_b - \frac{P}{\alpha\varepsilon} \tag{2.1.36}$$

where P is the polarization induced by the spatial separation of the electron and hole, ε is the dielectric constant of the substrate, and α is the geometrical factor of the photoconductive material. The geometrical factor α is equal to three for an isotropic dielectric material. It is noted that both, the free and trapped carriers contribute to the screening of the electric field. The time dependence of polarization P can be written as

$$\frac{dP}{dt} = -\frac{P}{\tau_r} + J \tag{2.1.37}$$

where τ_r is the recombination time between an electron and hole. In eq. (2.1.37), J is the density of the current contributed by an electron and hole,

$$J = env_h - env_e \tag{2.1.38}$$

where e is the charge of a proton. The change of electric currents leads to electromagnetic radiation according to Maxwell's equations. In a simple Hertzian dipole theory, the far-field of the radiation E_{THz} is given by

$$E_{THz} \propto \frac{\partial J}{\partial t} \tag{2.1.39}$$

To simplify the following calculations, we introduce a relative speed v between an electron and hole,

$$v = v_h - v_e \tag{2.1.40}$$

Then the electric field of radiation can be expressed as

$$E_{THz} \propto ev\frac{\partial n}{\partial t} + en\frac{\partial v}{\partial t} \tag{2.1.41}$$

The first term on the right-hand side of eq. (2.1.41) represents the electromagnetic radiation due to the carrier density change, and the second term represents the electromagnetic radiation which is proportional to the acceleration of the carrier under the electric field.

The simulated THz waveform in time domain by solving the differential equations in Drude-Lorentz model is shown in Fig. 2-1 referring to [13]. The momentum relaxation time is 30 fs, the carrier trapping time for the emitter is 0.5 ps, and the carrier recombination time τ_r is taken as 10 ps. The carrier generation density is 10^{18} cm^{-3} and the applied bias electric field is 20 KV/cm.

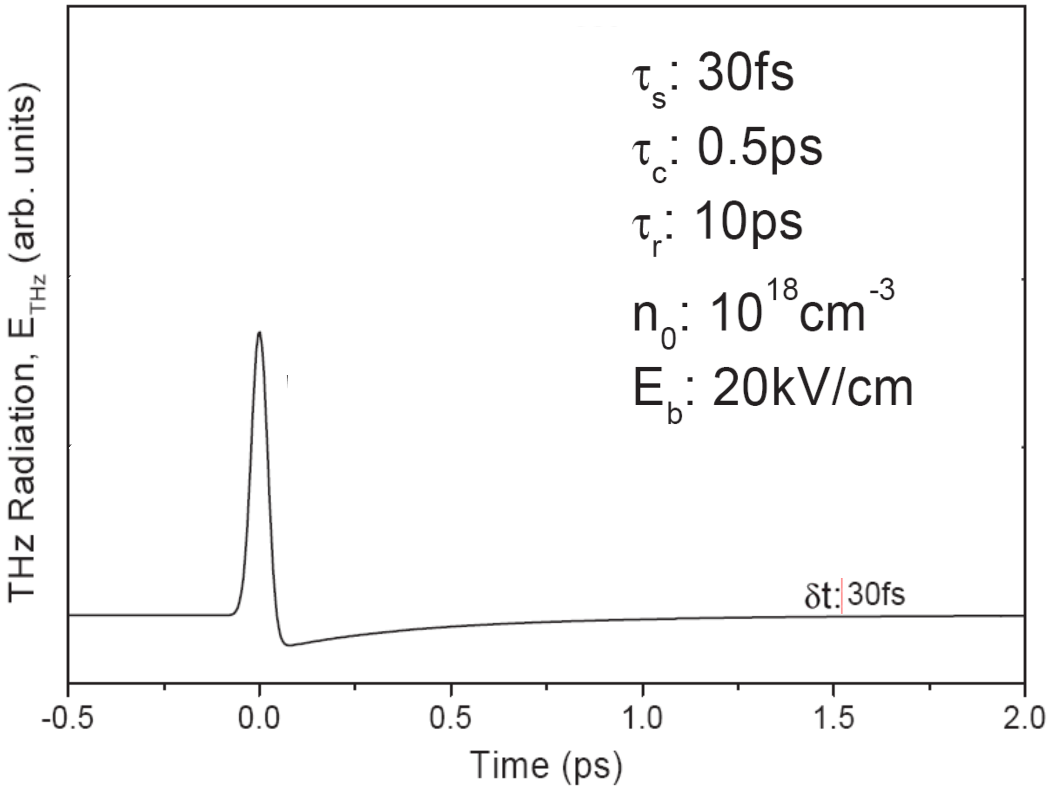

Fig. 2-1 Simulated THz time domain waveform by solving the differential equations in Drude-Lorentz model referring to [13].

2.1.2 Detection of THz Radiation Using Photoconductive Antennas

Actually, the measurement of THz signal is the measurement of the photocurrent induced in the detector by the simultaneous arrival of the THz pulse and the gating optical pulse [13]. Because of the non-instantaneous conductivity of the detector σ_d, a measurement of the photocurrent j induced by the arrival of the peak of the radiated electric field of the THz pulse at the detector at time t_p is actually a convolution of the radiated electric field and the conductivity of the detector after time t_p:

$$j(t_p)=\int_{t_p}^{\infty}E_{rad}(t')\sigma_d(t'-t_p)dt'. \qquad (2.1.42)$$

For the detector used in the experiments, the conductivity can be assumed to have the form

$$\sigma_d(t'-t_p)=\begin{cases}0 & \text{if } \mathrm{t_p}>t' \\ \dfrac{\sigma_0}{\tau_d}\exp\left[\dfrac{-(t'-t_p)}{\tau_d}\right] & \text{if } \mathrm{t_p}\le t'\end{cases} \qquad (2.1.43)$$

where σ_0 is the peak conductivity of the detector. The rise in the conductivity can be assumed to be rapid because of the gating optical pulse has a short duration. Therefore, it is assumed that $\tau_d >> 0$, and Eq.(2.1.43) can be written as

$$\sigma_d(t'-t_p)=\begin{cases}0 & \text{if } \mathrm{t_p}>t' \\ \dfrac{\sigma_0}{\tau_d} & \text{if } \mathrm{t_p}\le t'\end{cases} \qquad (2.1.44)$$

Substitution of Eq. (2.1.44) into Eq. (2.1.42) gives

$$j_p(t_p)=\frac{\sigma_0}{\tau_d}\int_{t_p}^{\infty}E_{rad}(t')dt' \qquad (2.1.45)$$

If it is assumed that the radiated waveform of the THz pulse is symmetric, then the measured photocurrent becomes

$$j\approx\frac{\sigma_0}{2\tau_d}\int_{-\infty}^{\infty}E_{rad}(t')dt' \qquad (2.1.46)$$

Substitution of $E_{rad}(t')$ as given by Eq.(2.1.41) into Eq. (2.1.46) gives

$$j=-\frac{\sigma_0}{2\tau_d}\frac{BE_bF_{opt}}{\tau}\int_{-\infty}^{\infty}\exp(\frac{-t'^2}{\tau^2})\times\left[1+DF_{opt}\int_{-\infty}^{t'/\tau}\exp(-x^2)dx\right]^{-2}dt' \qquad (2.1.47)$$

However, because of the internal reflection the back side of the photoconductor, the amplitude of the radiated electric field is attenuated.

The Fresnel formulas for reflection at a plane interface and conservation of energy, which indicate that the amplitude of the transmitted pulse is decreased relative to its initial value by the amount

$$\frac{2\sqrt{n}}{n+1} \tag{2.1.48}$$

Evaluation of Eq. (2.1.47) and multiplication of the result by Eq. (2.1.48) lead to the following expression for the measured detector photocurrent:

$$j = -\sigma_0 C E_b \frac{F/F_s}{1+(F/F_s)} \tag{2.1.49}$$

where

$$F_s = \frac{(n+1)\hbar\omega}{\eta_0 e(1-R)m}, \tag{2.1.50}$$

$$C = \frac{A\sqrt{n}}{4\pi\varepsilon_0 c^2 \eta_0 z \tau_d}. \tag{2.1.51}$$

As shown above, n is the index of refraction of the emitter at submillimeter wavelengths, $\hbar\omega$ is the photon energy, η_0 is the impedance of free space, R is the optical reflectivity of the emitter, A is the illuminated area of the emitter, ε_0 is the permittivity of free space, c is the speed of light, z is the emitter-detector separation, and -τ_d is the lifetime.

Eq. (2.1.49) can be rewritten as

$$E_{rad}(peak) = \frac{j}{\sigma_0} = -CE_b \frac{F/F_s}{1+(F/F_s)} \tag{2.1.52}$$

where $E_{rad}(peak)$ is the experimentally measured value associated with the peak of the radiated electric field and the right side, $-CE_b\{(F/F_s)/[1+(F/F_s)]\}$, is the form of the incident excitation optical fluence and the bias field E_b applied to the emitter. The constant

C provides a measure of the fraction of the bias field extracted in the far field, whereas F_s is the optical fluence required for extracting half the maximum field.

2.1.3 Terahertz Time-Domain Spectroscopy (THz-TDS)

Figure. 2-2 shows a schematic diagram of a THz-TDS spectrometer [4]. It consists of a femtosecond laser source (1), a beam splitter that divides the laser into two branches, a THz emitter (2), focusing and collimating optics (3), the sample (4), THz detector (5), a variable delay line (6) that alters the optical delay between the THz emitter and detector, and a lock-in amplifier (7). A computer (8) controls the delay line and displays the detector photocurrent versus path length.

The sources and detectors of THz-TDS consist of the same building blocks. Both are based on the photoconductive antenna, which consists of a semiconductor bridging the gap in a transmission line structure deposited on the semiconductor substrate. The response of the voltage-biased photoconductive antenna to a short optical pulse focused into the gap between the two metal contacts is illustrated in Fig. 2-3.

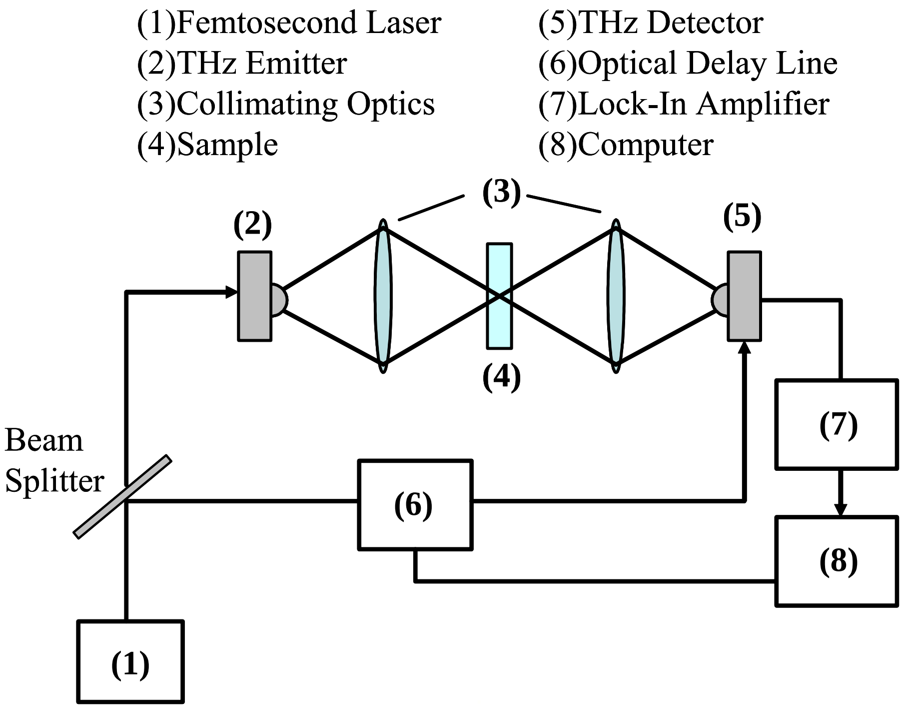

Fig. 2-2 Schematic diagram of a THz-TDS spectrometer using a femtosecond laser and photoconductive antennas to generate and detect THz waves.

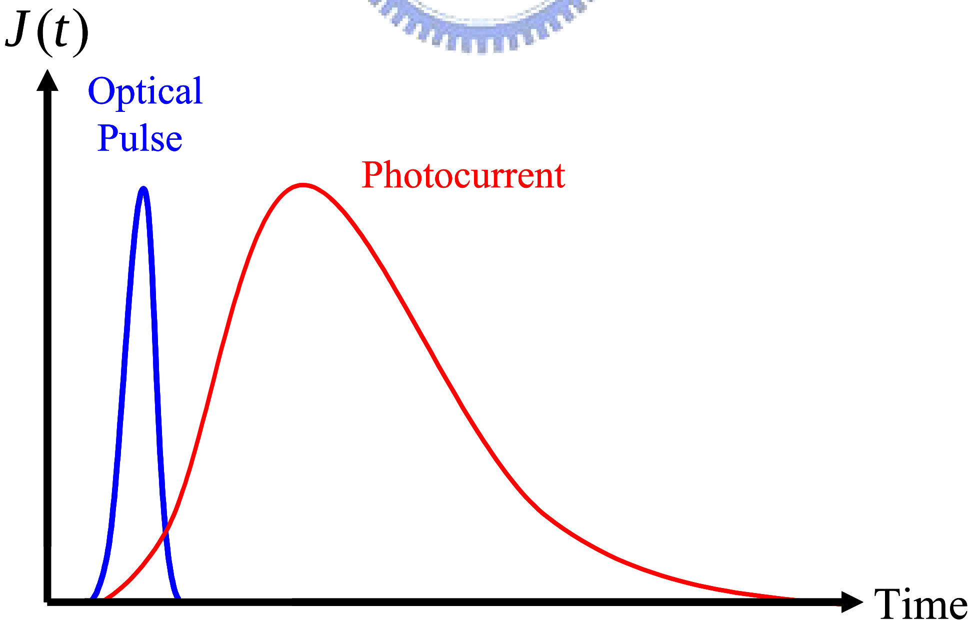

Fig. 2-3 Typical current response $J(t)$ of a photoconductive antenna to a short optical excitation pulse.

The current through the switch rises very rapidly when injecting photocarries by the optical pulse, and then decay with a time constant related to the carrier life time of the semiconductor. The transient photocurrent $J(t)$ radiates into free space according to Maxwell's equations,

$$E(t) \propto \partial J(t) \Big/ \partial t \tag{2.1.53}$$

Because of the time derivative, the radiated field is dominated by the rising edge of the photocurrent transient, which is much faster than the decay. Long tail of the photocurrent decay, which occur in most semiconductor without high defect density, are largely irrelevant to the radiated field.

To convert photoconductive antenna to a detector of short electrical pulses, a current-to-voltage amplifier is connected across the photoconductor, replacing the voltage bias. The electric field of the incident THz wave now provides the driving field for the photocarriers. Current flows through the switch only when both the THz wave and photocarriers are present. Because electronics are not fast enough to measure the THz transients directly, repetitive photoconductive sampling is used (Fig. 2-4). If the photocarrier lifetime, τ is much shorter than the THz pulse, the photoconductive switch acts as a sampling gate which samples the THz field within a time τ .

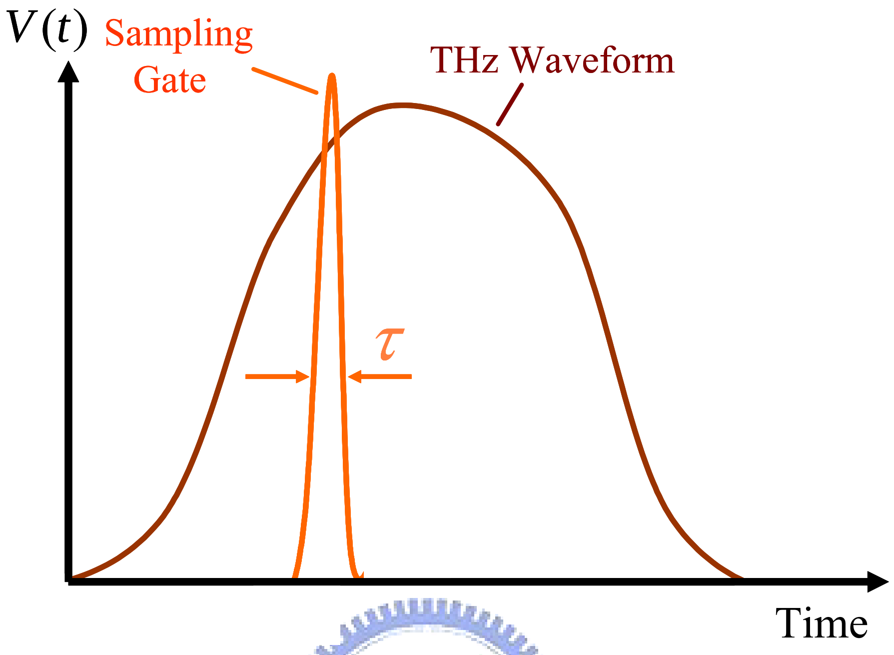

Fig. 2-4 Principle of photoconductive sampling. The photoconductive switch acts as a sampling gate that measures the waveform voltage V(t) within the sampling time τ .

Because the laser pulses which launch the emitter and gate the detector originate from the same source, the photoconductive gate can be moved across the THz waveform by changing the optical delay line shown in Fig. 2-2 (6). Fig. 2-5 shows using femtosecond pulse to analyze the THz waveform whose duration is about picoseconds. We can get entire THz transient waveform by employing this technique without the need for fast electronic components.

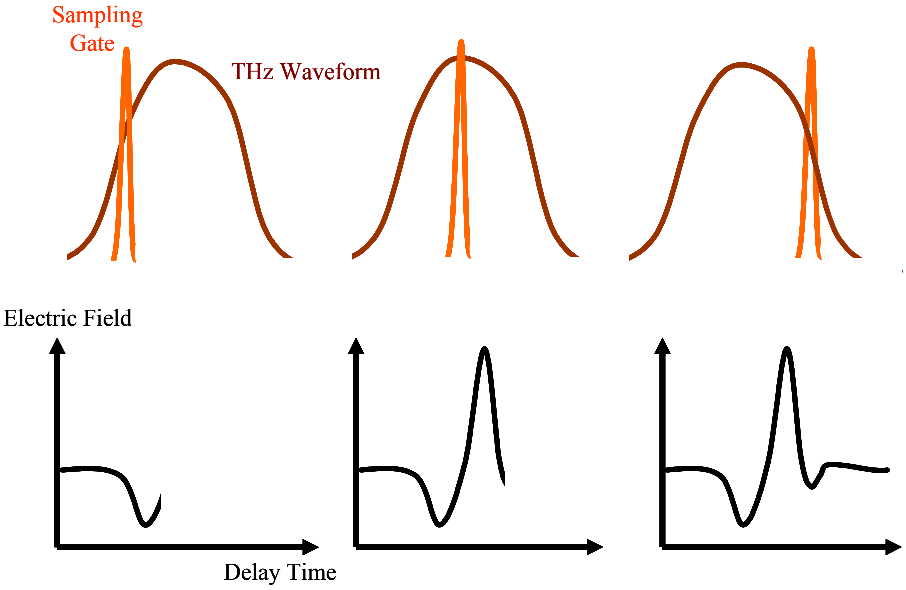

Fig. 2-5 Working principle of THz-TDS. By changing the optical delay between the optical pulse triggering the sampling gate and the waveform, the entire waveform can be mapped out sequentially in time.

2.1.4 Extraction of optical constant in THz-TDS

If the THz pulses before and after the sample insertion are denoted as $\mathrm{E}_{\mathrm{ref}}(t)$ and $E_{sam}(t)$, respectively, then the ratio of their Fourier transforms can be given by the complex refractive index of the sample $\tilde{n}(\omega)$ as [16]

$$\begin{aligned}\frac{\tilde{E}_{sam}(\omega)}{\tilde{E}_{ref}(\omega)} &= \tilde{t}_{as}(\omega)\tilde{t}_{sa}(\omega)\exp\left(i\frac{d(\tilde{n}(\omega)-1)\omega}{c}\right)\\ &\times\sum_{l=0}^{m}\left((\tilde{r}_{sa}(\omega))^{2}\exp\left(i\frac{2d\tilde{n}(\omega)\omega}{c}\right)\right)^{l}\\ &=\sqrt{T(\omega)}\exp(i\phi(\omega))\end{aligned}\tag{2.1.54}$$

Since the field $\mathrm{E}_{\mathrm{ref}}(t)$ is a real quantity, the Fourier transform will be a complex Hermitian spectrum with an angular frequency ω, $\tilde{E}(\omega)=E_{real}(\omega)-iE_{imag}(\omega)$, where $E(\omega)=E(-\omega)$. The $\tilde{t}_{as}(\omega)$, $\tilde{t}_{sa}(\omega)$, $\tilde{r}_{sa}(\omega)$ are the real Fresnel coefficients for amplitude transmission and reflection at the sample surfaces. The d means the thickness of the sample. The exponential factor represents the phase shift due to propagation in the material of the sample, and the last term is the contribution of the multiple reflection. The integer m represents the multiple reflection concluded in the observational time domain. $T(\omega)$ and $\phi(\omega)$ are experimentally obtained power transmittance and relative phase, respectively. Since it is difficult to obtain the complex refractive index $\tilde{n}(\omega)=n(\omega)-i\kappa(\omega)$ directly from (2.1.55), the expressions for the real and imaginary parts of the complex refractive index of the sample are denoted as

$$n(\omega)=\frac{c}{d\omega}(\phi(\omega)+\frac{d\omega}{c}+\arg(\tilde{t}_{as}(\omega)\tilde{t}_{sa}(\omega)\sum_{l=0}^{m+1}((\tilde{r}_{sa}(\omega))^2\exp(-i\frac{2\tilde{n}(\omega)d\omega}{c}))^l)) \qquad (2.1.56)$$

$$\kappa(\omega)=-\frac{c}{2d\omega}\ln(\frac{T(\omega)}{\left|\tilde{t}_{as}(\omega)\tilde{t}_{sa}(\omega)\sum_{l=0}^{m+1}((\tilde{r}_{sa}(\omega))^2\exp(-i\frac{2\tilde{n}(\omega)d\omega}{c}))^l\right|^2})$$

We use the value of the complex refractive index roughly estimated from the THz pulse in the time domain before and after the sample insertion as a starting point for an iterative loop wherein $n(\omega)$ and $\kappa(\omega)$ are calculated in a self-consistent manner. By performing this cyclic procedure for only a few times, the value would lead to a convergence.

2.2 Metallic Hole Arrays (MHAs)

Metal films with two-dimensional periodic arrays of subwavelength holes can exhibit extraordinary optical transmission characteristics [8]. This discovery attracts much attention because of its potential applications for subwavelength optics. The enhanced transmission is explained to be due to the resonant coupling of incident light with surface plasmon polaritons (SPPs) [10]. The enhanced peak was observed that it will be changed strongly with different geometry of the structure. There are three main parameters, such as hole diameter d, lattice constant s, and thickness of the metal plate t. The hole arrays can be cubic or triangular. Schematic diagram of two-dimensional metallic hole array (2D-MHA) with triangular lattice is shown below

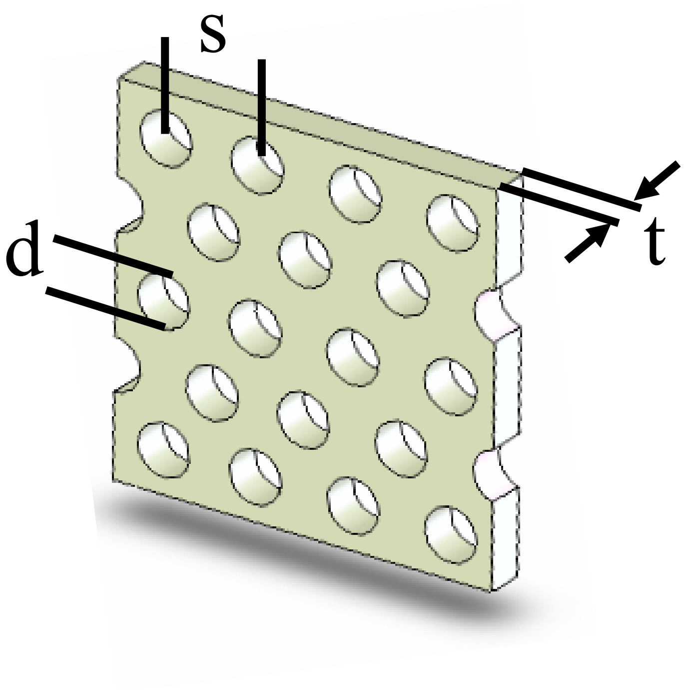

Fig. 2-6 Schematic diagram of the 2D-MHA. There are three main parameters, such as hole diameter d, lattice constant s, and thickness of the metal plate t

Since every hole can be thought as a waveguide, there must exist a cut-off frequency in this sample. Moreover, when the frequency of the incident wave is larger than diffraction limit, it will be diffracted into the first lobe due to the periodic structure [5]. It will be discussed explicitly below.

2.2.1 Cutoff Frequency and Diffraction Limit

Consider a circular waveguide with metallic surface and radius a. Equations of time-harmonic electric and magnetic field can be written as following [17]:

$$\begin{aligned} \nabla^2 E + k^2 E &= 0 \\ \nabla^2 H + k^2 H &= 0 \end{aligned} \qquad (2.2.1)$$

For a straight and uniform circular waveguide, it is convenient to decompose the 3-D Laplacian operator ∇^2 into two parts: $\nabla_{r\phi}^2$ and ∇_z^2 for transverse and longitudinal components, respectively. For TM waves, $H_z = 0$ and $E_z \neq 0$, all fields can be expressed in terms of $E_z = E_z^0 e^{-\gamma z}$, where E_z^0 satisfies the homogeneous Helmholtz's equation

$$\begin{aligned} &\nabla_{r\phi}^2 E_z^0 + (\gamma^2 + k^2) E_z^0 = 0 \\ &or \quad \nabla_{r\phi}^2 E_z^0 + h^2 E_z^0 = 0 \end{aligned} \;. \qquad (2.2.2)$$

For TE waves, $E_z = 0$ and $H_z \neq 0$, all fields can be expressed in terms of $H_z = H_z^0 e^{-\gamma z}$, where H_z^0 satisfies the same homogeneous Helmholtz's equation listed above.

For TM waves in circular waveguides,

$$E_z(r,\phi,z) = E_z^0(r,\phi)e^{-\gamma z} . \tag{2.2.3}$$

The solutions are

$$\begin{aligned}
E_z^0 &= C_n J_n(hr)\cos n\phi \\
E_r^0 &= -\frac{j\beta}{h} C_n J_n'(hr)\cos n\phi \\
E_\phi^0 &= -\frac{j\beta n}{h^2 r} C_n J_n(hr)\sin n\phi \\
H_r^0 &= -\frac{j\omega\varepsilon n}{h^2 r} C_n J_n(hr)\sin n\phi \\
H_\phi^0 &= -\frac{j\omega\varepsilon}{h} C_n J_n'(hr)\cos n\phi \\
H_z^0 &= 0
\end{aligned} \tag{2.2.4}$$

where $j\beta$ is equal to γ, J_n is a Bessel function, and C_n is a coefficient. The eigenvalues of TM modes are determined from the boundary condition that E_z^0 must vanish at r = a:

$$J_n(ha) = 0 \tag{2.2.5}$$

For the lowest TM mode, TM$_{01}$,

$$(h)_{TM_{01}} = \frac{2.405}{a}, \tag{2.2.6}$$

which yields the lowest cutoff frequency:

$$(f_c)_{TM_{01}} = \frac{(h)_{TM_{01}}}{2\pi\sqrt{\mu\varepsilon}} = \frac{0.383}{a\sqrt{\mu\varepsilon}} \quad \text{(Hz)} \tag{2.2.7}$$

For TE waves in circular waveguides,

$$H_z(r,\phi,z) = H_z^0(r,\phi)e^{-\gamma z} \tag{2.2.8}$$

The solutions are

$$
\begin{aligned}
&H_z^0 = C_n' J_n(hr)\cos n\phi \\
&H_r^0 = -\frac{j\beta}{h} C_n' J_n'(hr)\cos n\phi \\
&H_\phi^0 = \frac{j\beta n}{h^2 r} C_n' J_n(hr)\sin n\phi \\
&E_r^0 = \frac{j\omega\mu n}{h^2 r} C_n' J_n(hr)\sin n\phi \\
&E_\phi^0 = \frac{j\omega\mu}{h} C_n' J_n'(hr)\cos n\phi \\
&E_z^0 = 0
\end{aligned}
\tag{2.2.9}
$$

where C_n' is a coefficient. The eigenvalues of TE modes are determined from the boundary condition that the normal derivative of H_z^0 must vanish at r = a:

$$J_n'(ha) = 0 \tag{2.2.10}$$

For the lowest TE mode, TE$_{11}$,

$$(h)_{TE_{11}} = \frac{1.841}{a}, \tag{2.2.11}$$

which yields the lowest cutoff frequency:

$$(f_c)_{TE_{11}} = \frac{(h)_{TE_{01}}}{2\pi\sqrt{\mu\varepsilon}} = \frac{0.293}{a\sqrt{\mu\varepsilon}} \quad \text{(Hz)} \tag{2.2.12}$$

In conclusion, the cutoff frequency for an infinitely long cylindrical waveguide is defined by the hole diameter d

$$\nu_{cutoff} = 1.841\frac{c}{\pi d} \tag{2.2.12}$$

where c is speed of light in free space.

In addition to the cutoff frequency, owing to the triangular hole array represents a 2-D grating. When electromagnetic waves with frequency above

$$v_{diff} = \frac{2c}{s\sqrt{3}} \tag{2.2.13}$$

it will be diffracted into the first lobe. where s is the hole spacing.

2.2.2 Theories of Surface Plasmons (SPs)

In order to understand the characteristics of surface plasmons, we consider a p-wave propagates along the interface between dielectric material (ε_1) and metal (ε_2) in the x-direction. The metal locate in the area where $z < 0$, such as in Fig. 2-7:

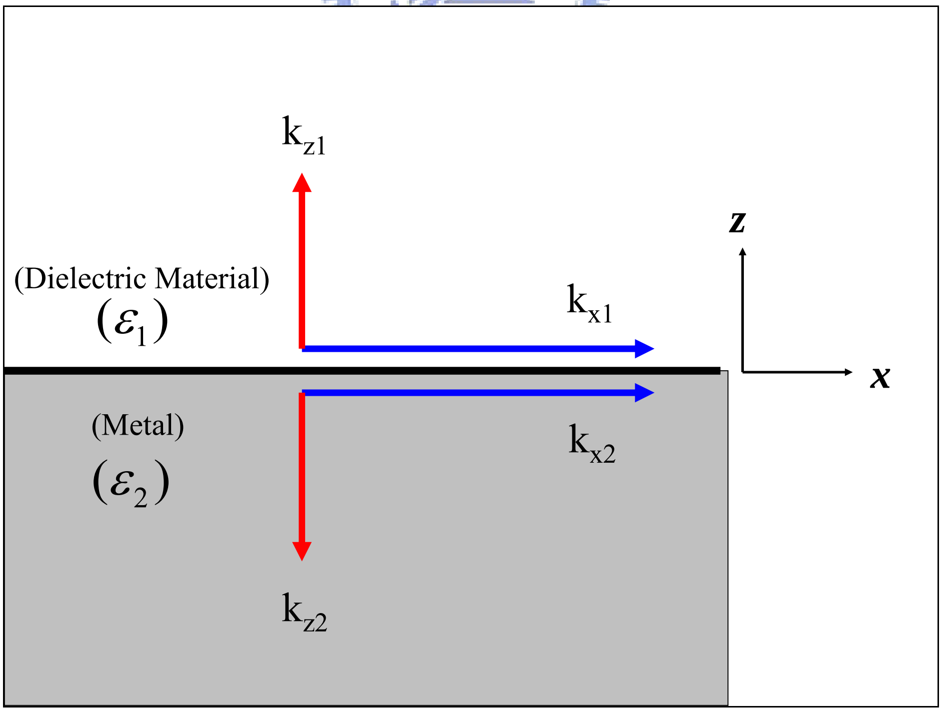

Fig. 2-7 A p-wave propagates along the interface between dielectric material (ε_1) and metal (ε_2) in the x-direction when $z > 0$.

$$\begin{aligned} H_1 &= (0, H_{y1}, 0)\exp i(k_{x1}x + k_{z1}z - \omega t) \\ E_1 &= (E_{x1}, 0, E_{z1})\exp i(k_{x1}x + k_{z1}z - \omega t) \end{aligned} \tag{2.2.14}$$

when $z < 0$

$$\begin{aligned} H_2 &= (0, H_{y2}, 0)\exp i(k_{x1}x - k_{z1}z - \omega t) \\ E_2 &= (E_{x2}, 0, E_{z2})\exp i(k_{x2}x - k_{z2}z - \omega t) \end{aligned} \tag{2.2.15}$$

The above equations must satisfy the Maxwell equations,

$$\vec{\nabla}\cdot\vec{E}_i = 0 \quad \vec{\nabla}\cdot\vec{H}_i = 0 \quad \vec{\nabla}\times\vec{E}_i = -\mu_i \frac{1}{c}\frac{\partial\vec{H}_i}{\partial t} \quad \vec{\nabla}\times\vec{H}_i = \varepsilon_i \frac{1}{c}\frac{\partial\vec{E}_i}{\partial t} \tag{2.2.16}$$

$and \quad i = 1, 2$

Then, using the boundary conditions,

$$E_{x1} = E_{x2} \qquad H_{y1} = H_{y2} \qquad \varepsilon_1 E_{z1} = \varepsilon_2 E_{z2} \tag{2.2.17}$$

We can obtain the following results:

$$\begin{aligned} k_{x1} &= k_{x2} \equiv k_x = \frac{\omega}{c}\left(\frac{\varepsilon_1\varepsilon_2}{\varepsilon_1 + \varepsilon_2}\right)^{1/2} \\ k_{zi} &= \left[\varepsilon_i\left(\frac{\omega}{c}\right)^2 - k_x^2\right]^{1/2} \quad , \quad i = 1, 2 \end{aligned} \tag{2.2.18}$$

This is the relative formula for the surface plasmons in metal. We can find that

$$k_x = \frac{\omega}{c}\left(\frac{\varepsilon_1\varepsilon_2}{\varepsilon_1 + \varepsilon_2}\right)^{1/2} > \frac{\omega}{c}\varepsilon_1^{1/2} \tag{2.2.19}$$

That is to say the wavevector of electric field in the surface plasmon is larger than the incident electromagnetic wave. Fig. 2-8 shows the dispersion relation of the incident electromagnetic wave and the surface plasmon.

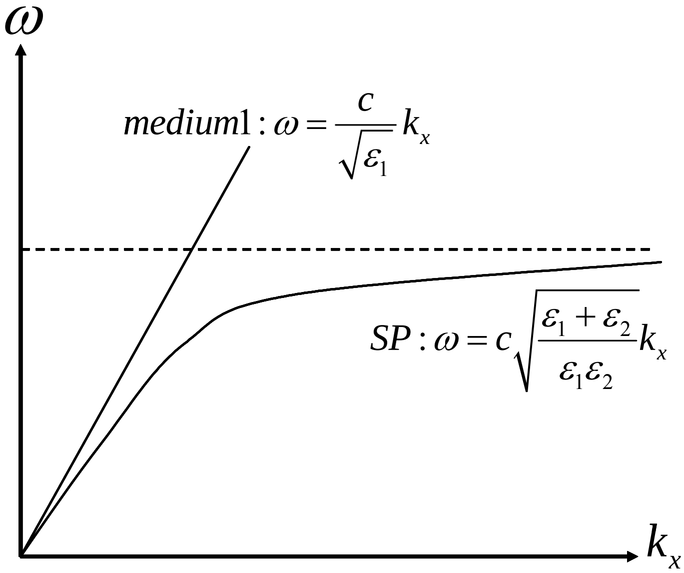

Fig. 2-8 The dispersion relation of the incident electromagnetic wave and the surface plasmon. Medium1: the dispersion curve of EM waves propagate in dielectric material; SP: the dispersion curve of surface plasmon.

Since the dispersion curve of surface plasmon always lies to the right of the incident electromagnetic wave so the usual incident photons can't excite surface plasmon polaritons (SPPs). However, periodical holes in the metallic film can lead to the in-plane momentum which aids the photon energy coupled to surface plasmon polariton modes [18]. The corresponding relation for conservation of momentum is

$$\vec{k}_{sp} = \vec{k}_x + i\vec{G}_x + j\vec{G}_y \tag{2.2.20}$$

where $\vec{k}_{sp}$ is the wave vector associated with the SPP, $\vec{k}_x$ is the transverse wave vector component of the incident radiation, $\vec{G}_x$ and $\vec{G}_y$ are the wave vector components associated with the two-dimensional array, and i and j are integers. $k_x = (2\pi / \lambda \sin\theta)$ is the component of the wave vector of the incident light that lies in the plane ($\theta = 0$ for normal incidence), From the above calculation,

$$k_{sp} = \frac{\omega}{c}\left(\frac{\varepsilon_d \varepsilon_m}{\varepsilon_d + \varepsilon_m}\right)^{\frac{1}{2}} \tag{2.2.21}$$

where ω is the frequency of the incident electromagnetic radiation, c is the speed of light in vacuum, ε_d is the dielectric constant of the dielectric interface medium and ε_m is the (complex) dielectric constant of the metal. This last quantity may be expressed as $\varepsilon_m = \varepsilon_{mr} + i\varepsilon_{mi}$, where ε_{mr} and ε_{mi} are the real and imaginary components of the dielectric constant of the metal, respectively. The complex propagation constant for the SPP wave can be expressed as $k_{sp} = k_{spr} + ik_{spi}$, where the two individual components can be written as [19]

$$\begin{aligned} k_{spr} &= \frac{\omega}{c}\left[\frac{\varepsilon_d}{(\varepsilon_{mr+}\varepsilon_d)^2 + \varepsilon_{mi}{}^2}\right]^{\frac{1}{2}}\left[\frac{\varepsilon_e{}^2 + (\varepsilon_e{}^4 + \varepsilon_d{}^2\varepsilon_{mi}{}^2)^{\frac{1}{2}}}{2}\right]^{\frac{1}{2}} = \frac{\omega}{c}n_{sp} \\ k_{spi} &= \frac{\omega}{c}\left[\frac{\varepsilon_d}{(\varepsilon_{mr+}\varepsilon_d)^2 + \varepsilon_{mi}{}^2}\right]^{\frac{1}{2}}\frac{\varepsilon_d\varepsilon_{mi}}{\{2[\varepsilon_e{}^2 + (\varepsilon_e{}^4 + \varepsilon_d{}^2\varepsilon_{mi}{}^2)^{\frac{1}{2}}]\}^{\frac{1}{2}}} \end{aligned} \tag{2.2.22}$$

with $\varepsilon_e{}^2 = \varepsilon_{mr}{}^2 + \varepsilon_{mi}{}^2 + \varepsilon_d\varepsilon_{mr}$. In the limit where $\varepsilon_{mi} > |\varepsilon_{mr}|$ and $|\varepsilon_{mr}|, \varepsilon_{mi} \gg \varepsilon_d$, which is true for most metals at THz frequencies, the real and imaginary components of the SPP wave vector can be greatly simplified. The real component of the SPP propagation constant may be approximated as

$$k_{spr} = \frac{\omega}{c} n_{sp} \simeq \frac{\omega}{c}\sqrt{\varepsilon_d} \tag{2.2.23}$$

and the imaginary component of the SPP propagation constant may be approximated as

$$k_{spi} = \frac{\omega}{c}\frac{\varepsilon_d^{\frac{3}{2}}}{2\varepsilon_{mi}} \tag{2.2.24}$$

At normal incidence, Eq. (2.2.23) gives the position of the maxima:

$$\lambda_{\max} = a_0 (i^2 + j^2)^{-\frac{1}{2}} \sqrt{\varepsilon_d} \tag{2.2.25}$$

for a square lattice. For a triangular lattice a similar derivation yields

$$\lambda_{\max} = a_0 [\frac{4}{3}(i^2 + ij + j^2)]^{-\frac{1}{2}} \sqrt{\varepsilon_d} \tag{2.2.26}$$

2.3 Finite-Difference Time-Domain(FDTD) Algorithm

Maxwell's partial differential equations of electrodynamics, formulated circa 1870, represent a fundamental unification of electric and magnetic fields predicting electromagnetic wave phenomena which Nobel Laureate Richard Feynman has called the most outstanding achievement of 19th-centry science. Now engineers and scientists worldwide use computers ranging from simple desktop machines to massively parallel arrays of processors to obtain solutions of these equations for the purpose of investigating electromagnetic wave guiding, radiation, and scattering phenomena and technologies. In this chapter, we discuss prospects for using numerical solutions of Maxwell's equations, in particular the finite-difference time-domain (FDTD) method.

There are seven primary reasons for the expansion of interest in FDTD and related computational solution approaches for Maxwell's equations [20]:

1. *FDTD use no linear algebra.* Being a fully explicit computation, FDTD avoids the difficulties with linear algebra that limit the size of frequency-domain integral-equation and finite-element electromagnetics models to generally fewer than 106 electromagnetic field unknowns. FDTD models with as many as 109 field unknowns have been run; there is no intrinsic upper bound to this number.

2. *FDTD is accurate and robust.* The sources of error in FDTD calculations are well understood, and can be bounded to permit accurate models for a very large variety of electromagnetic wave interaction problems.

3. *FDTD treats impulsive behavior naturally.* Being a time-domain technique, FDTD directly calculates the impulse response of an electromagnetic system. Therefore, a single FDTD simulation can provide either ultra wideband temporal waveforms or the sinusoidal steady-state response at any frequency with the excitation spectrum.

4. *FDTD treats nonlinear behavior naturally.* Being a time-domain technique, FDTD directly calculates the nonlinear response of an electromagnetic system.

5. *FDTD is a systematic approach.* With FDTD, specifying a new structure to be modeled is reduced to a problem of mesh generation rather than the potentially complex reformulation of an integral equation. For example, FDTD requires no calculation of structure-dependent Green's functions.

6. *Computer memory capacities are increasing rapidly.* While this trend positively influences all numerical techniques, it is of particular advantage to FDTD methods which are founded on discretizing space over a volume, and therefore inherently require a large random access memory.

7. *Computer visualization capabilities are increasing rapidly.* While this trend positively influences all numerical techniques, it is of particular advantage to FDTD methods which generate time-marched arrays of field quantities suitable for use in color videos to illustrate the field dynamics.

In fact, the large-scale solution of Maxwell's equations for electromagnetic wave phenomena using FDTD and similar grid-based time-domain approaches may be fundamental to the advancement of the ultra complex and the ultra fast. Maxwell’s equations provide the physics of electromagnetic wave phenomena from do to light, and their accurate modeling is essential to understand high-speed signal effects having wave-transport behavior. A key goal is the computational unification of electromagnetic waves; charge transport in transistors, Josephson junctions, and electro-optic devices; surface and volumetric wave dispersions; and nonlinearities due to quantum effects. Then these can attack a broad spectrum of important problems to advance electrical and computer engineering and directly benefit our society.

2.3.1 Finite-Difference Expressions for Maxwell’s Equations

Imagine a region of space where which contains no flowing currents or isolated charges. Maxwell's curl equations in can be written in Cartesian coordinates as six simple scalar equations. Two examples are:

$$\begin{aligned} \frac{\partial H_x}{\partial t} &= \frac{1}{\mu}\left(\frac{\partial E_y}{\partial z} - \frac{\partial E_z}{\partial y}\right) \\ \frac{\partial E_x}{\partial t} &= \frac{1}{\varepsilon}\left(\frac{\partial H_z}{\partial y} - \frac{\partial H_y}{\partial z}\right) \end{aligned} \tag{2.3.1}$$

The other four are symmetric equivalents of the above and are obtained by cyclically exchanging the x, y, and z subscripts and derivatives.

Maxwell’s equations describe a situation in which the temporal change in the **E** field is dependent upon the spatial variation of the **H** field, and vice versa. The FDTD method solves Maxwell's equations by first discretizing the equations via central differences in time and space and then numerically solving these equations in software.

The most common method to solve these equations is based on Yee's mesh [21] and computes the **E** and **H** field components at points on a grid with grid points spaced Δx, Δy, and Δz apart. The **E** and the **H** field components are then interlaced in all three spatial dimensions as shown in Fig. 2-9. Furthermore, time is broken up into discrete steps of Δt. The **E** field components are then computed at times $t = n\ \Delta t$ and the **H** fields at times $t = (n+1/2)\ \Delta t$, where n is an integer representing the compute step. For example, the **E** field at a time t = n Δ*t* is equal to the **E** field at t = (n-1) Δ*t* plus an additional term computed from the spatial variation, or curl, of the **H** field at time t.

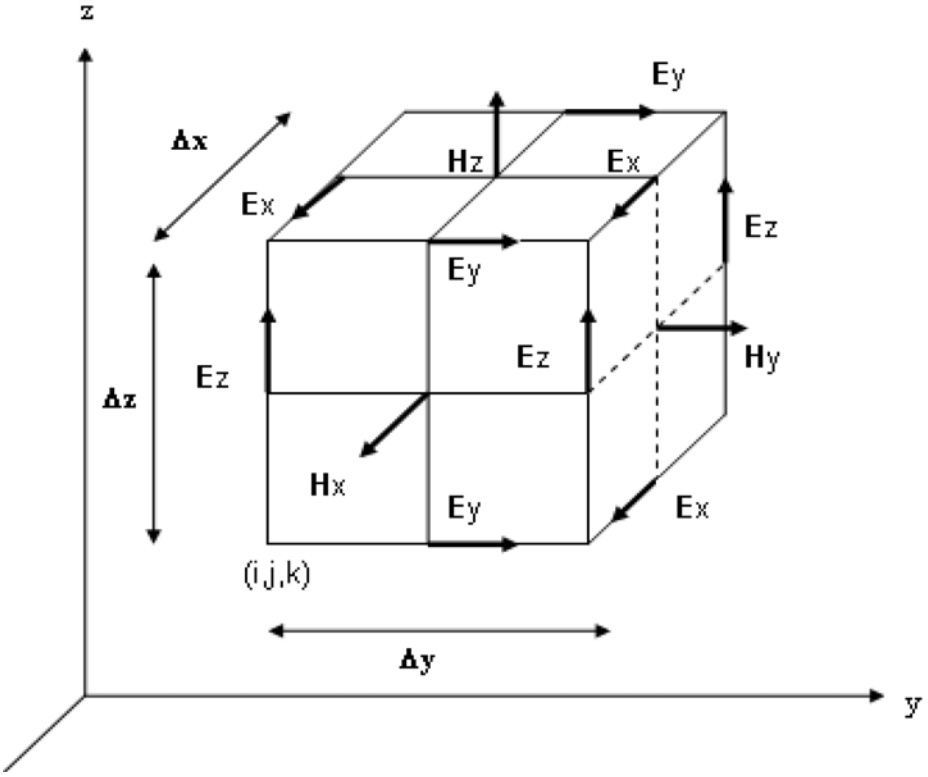

Fig. 2-9 Yee’s mesh

This method results in six equations that can be used to compute the field at a given mesh point, denoted by integers *i*, *j*, *k*. For example, two of the six are:

$$
\begin{aligned}
&H^{n+1/2}_{x(i,j+1/2,k+1/2)} = H^{n-1/2}_{x(i,j+1/2,k+1/2)} \\
&+\frac{\Delta t}{\mu\Delta z}\left(E^{n}_{y(i,j+1/2,k+1)} - E^{n}_{y(i,j+1/2,k)}\right) \\
&-\frac{\Delta t}{\mu\Delta y}\left(E^{n}_{z(i,j+1,k+1/2)} - E^{n}_{z(i,j,k+1/2)}\right) \\
&E^{n+1}_{x(i+1/2,j+1,k+1)} = E^{n}_{x(i+1/2,j+1,k+1)} \\
&+\frac{\Delta t}{\varepsilon\Delta y}\left(H^{n+1/2}_{z(i+1/2,j+1/2,k+1)} - H^{n+1/2}_{z(i+1/2,j-1/2,k+1)}\right) \\
&-\frac{\Delta t}{\varepsilon\Delta z}\left(H^{n+1/2}_{y(i+1/2,j,k+1/2)} - H^{n+1/2}_{y(i+1/2,j,k+3/2)}\right)
\end{aligned}
\tag{2.3.2}
$$

These equations are iteratively solved in a leapfrog manner, alternating between computing the **E** and **H** fields at subsequent Δ*t*/2 intervals.

2.3.2 Stability in FDTD algorithm

Now we discuss that how we determine the time step Δ*t*. An EM wave propagating in free space cannot go faster than the speed of light. To propagate of one cell requires a minimum time of $\Delta t = \Delta x / c_0$. When we get to two-dimensional simulation, we have to allow for the propagation in the diagonal direction, which brings the time requirement to $\Delta t = \Delta x/(\sqrt{2}c_0)$. Furthermore, $\Delta t = \Delta x/(\sqrt{3}c_0)$ is required in three-dimensional simulation. This is summarized by the well-known "Courant Condition" [22]

$$\Delta t \le \frac{\Delta x}{\sqrt{n} \cdot c_0} \tag{2.3.3}$$

where n is the dimension of the simulation.

It is convenient to specify the time step for any simulation in (2.3.4).

$$\Delta t = \frac{\Delta x}{2 \cdot c_0} \tag{2.3.4}$$

2.4 The Drude Dispersion Model for Metal

In keeping with IR spectroscopic notation, all frequencies will be expressed in cm^{-1}. The complex dielectric function ε_c and the complex index of refraction n_c , are defined as

$$\varepsilon_c \equiv \varepsilon_1 + i\varepsilon_2 \equiv {n_c}^2 = (n - i\kappa)^2 \tag{2.4.1}$$

The Drude model dielectric function is [23]

$$\varepsilon_c = \varepsilon_\infty - \frac{{\omega_p}^2}{\omega^2 + i\omega\omega_\tau} \tag{2.4.2}$$

where ω , ω_p and ω_τ, have units of cm^{-1}. Separating the real and imaginary parts yields

$$\begin{aligned} \varepsilon_1 &= \varepsilon_\infty - \frac{{\omega_p}^2}{\omega^2 + {\omega_\tau}^2} \\ \varepsilon_2 &= \frac{{\omega_p}^2 \omega_\tau}{\omega^3 + \omega{\omega_\tau}^2} \end{aligned} \tag{2.4.3}$$

In these equations, the plasma frequency is

$$\omega_p(cm^{-1}) = \frac{1}{2\pi c}\left(\frac{4\pi N e^2}{m^* \varepsilon_\infty}\right)^{\frac{1}{2}} \tag{2.4.4}$$

where N is the free electron density, e is the electron charge, m^* is the effective mass of the electrons, and ε_∞ is the high frequency dielectric constant. The damping frequency ω_τ expressed in cm^{-1}, is

$$\omega_\tau(cm^{-1}) = \frac{1}{2\pi c\tau} \tag{2.4.5}$$

where τ is the electron lifetime in seconds and c is the velocity of light.

If we have a group of $(\varepsilon_1, \varepsilon_2)$ at any frequency, from (2.4.3) we can calculate the value of ω_p and ω_τ by solving the simultaneous equation.

$$\begin{aligned} \omega_\tau &= \frac{\omega\varepsilon_2}{(1-\varepsilon_1)} \\ {\omega_p}^2 &= (1-\varepsilon_1)(\omega^2 + {\omega_\tau}^2) \end{aligned} \tag{2.4.6}$$

This was done for several values of co to obtain several pairs of co, and cop, which produce the curve with the best eyeball fit to the data.

3 Experiments and Simulated Methods

3.1 THz-TDS using LT-GaAs photoconductive antanna

The THz-TDS system we used was shown in the Fig. 3-1, and transient current was generated by femtosecond laser pulses impinging on a photoconducting material, dipole antenna on a LT-GaAs substrate. Emission of electromagnetic pulses, THz radiation, of about picosecond duration were produced by this current. The THz pulse was collected and guided by gold-coated parabolic mirrors. Femtosecond laser pulse as a probe beam with time delayed by motor stage .Also using the LT-GaAs antenna to detect the THz wave. Finally, connect the detected voltage signal to the lock-in amplifier. Signal from the lock-in amplifier can be obtained using PC easily. The photo of our THz-TDS system is shown in Fig. 3-2.

Because of its unique properties (high carrier mobility, high dark resistivity and subpicosecond carrier lifetimes) low temperature-(LT) grown GaAs is widely used to be the material for the THz emitters or detectors [24]. Post-growth annealing of LT-GaAs at temperature above 600°C leads to the nucleation of excess arsenic in As precipitates. The influence of As precipitates on the high resistivity of annealed LT-GaAs is related to As clusters, which is also responsible for the fast recombination of the photoinjected carriers. Recently, the trapping time reduction was observed for heavily doped LT-GaAs.

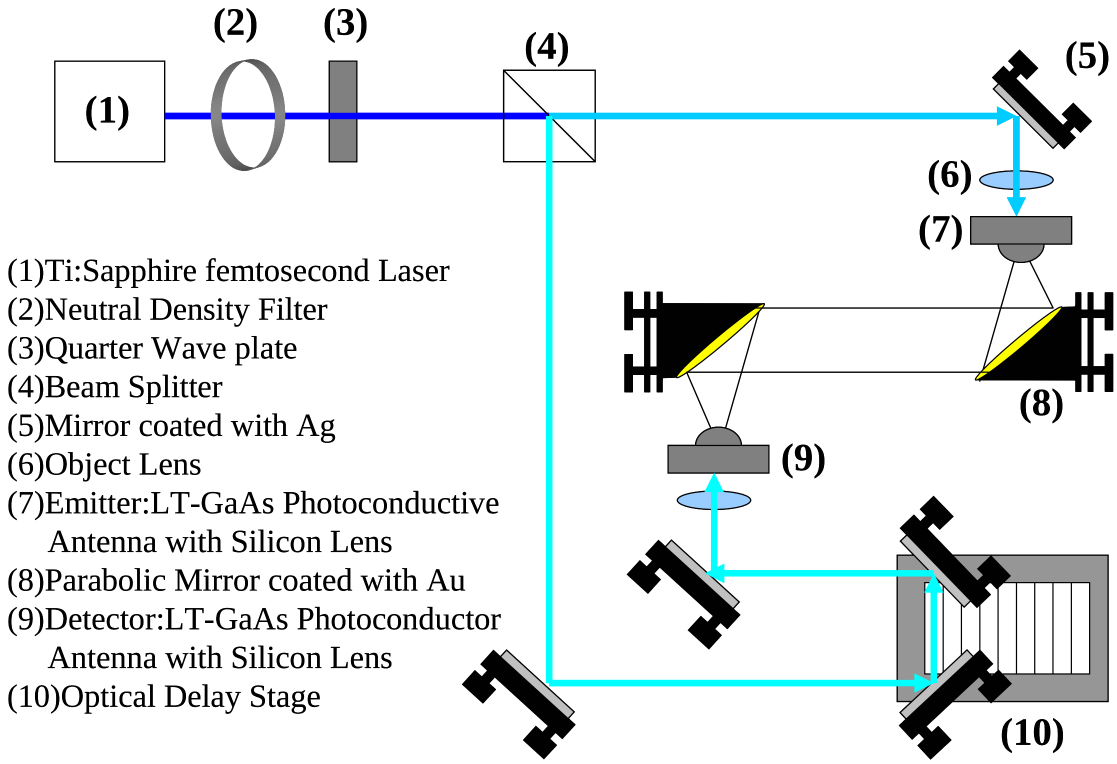

Fig. 3-1 Terahertz Time-Domain Spectroscopy in our lab.

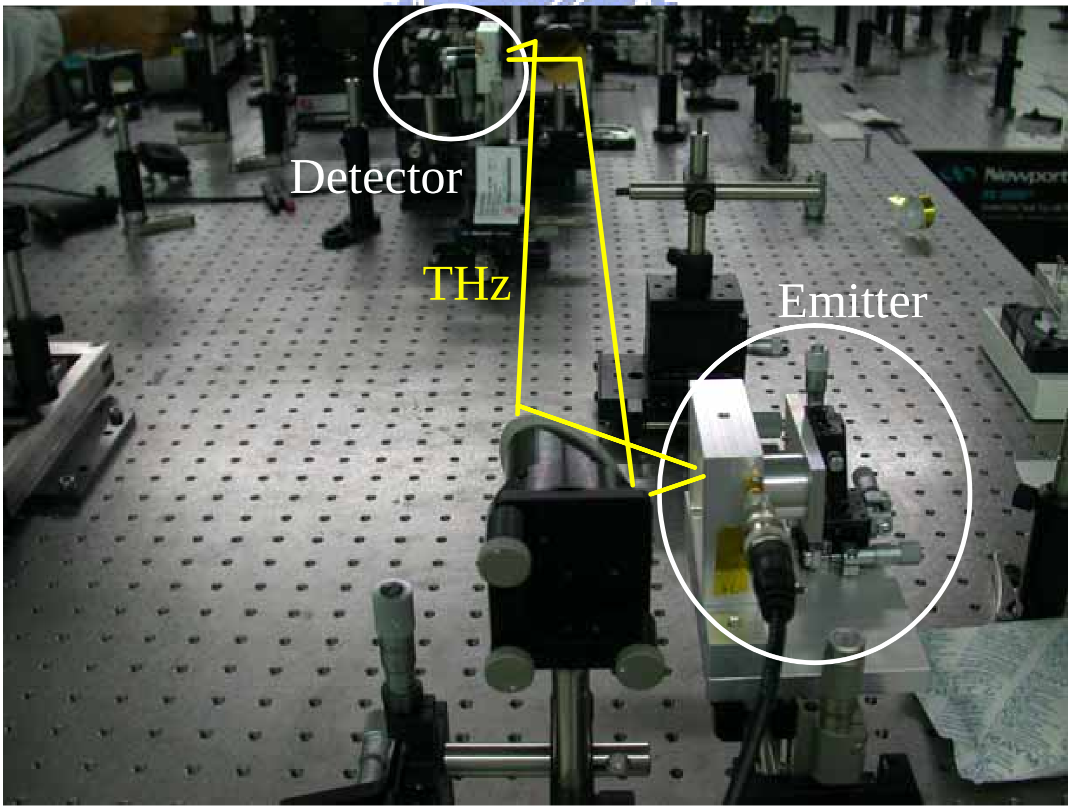

Fig. 3-2 The photo of our THz-TDS system. The photoconductive emitter and detector forms a symmetry type can be seen.

We also use the silicon lens to make the second reflective signal from the substrate far away from the expected time domain waveform. There are three possible silicon lens designs are depicted in Fig. 3-3 [4]. In the hemispherical design (Fig. 3-3 (a)), the emitted source is located at the center of the silicon lens all rays exit the lens/air interface at normal incidence. The radiation pattern inside the substrate is preserved in the transition to free-space because no refraction occurs. The design in Fig. 3-3 (b) is the aplanatic hyper-hemispherical substrate lens. Like the hemispherical design, it has no spherical aberration or coma, and when using silicon as a lens material, no chromatic dispersion. The design specification for the aplanatic design is

$$\rho = r/n \tag{3.1.1}$$

where ρ is the distance from the center of the lens to the focal point, r is the radius of the lens, and n is the refractive index. This design provides a slight collimation of the beam. The design in Fig. 3-3 (c) locates the dipole source at the focal point of the lens so that geometrical optics predicts a fully collimated output beam. However, diffraction is important because of the long wavelength of the THz wave compared to the lateral dimension of the beam exiting the lens, and, unless substrate lenses with a diameter much larger than the wavelength are used, the beam propagates with a larger divergence compared to the other designs.

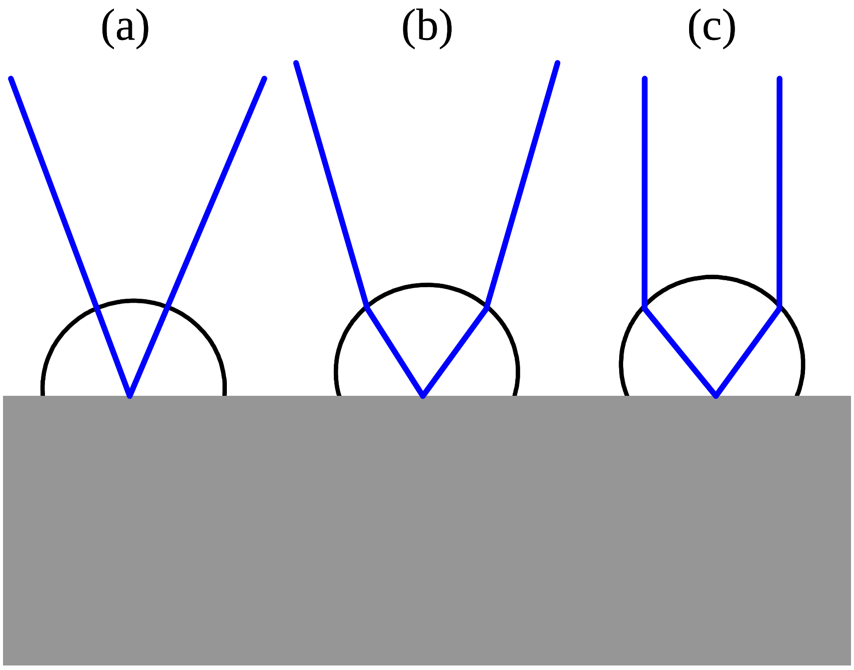

Fig. 3-3 Three different silicon design. (a) the non-focusing hemispherical design. (b) the hyper-hemispherical lens, and (c) , the collimating substrate lens.

The type of our silicon lens is hyper-hemispherical lens, the radius is 6.75mm and the total thickness is 8.35mm. When using the hyper-hemispherical silicon lens, the focal length of the first collective Au-coated parabolic mirror is changed due to the silicon lens, and we can use the equation in geometric optics. For example, in Fig. 3-4, this is the case of our setup, the thickness of the GaAs substrate is 0.355mm. If we want to know where is the imaging point of the dipole antenna through the hyper-hemispherical silicon lens, we can use the well-known equation in geometric optics.

$$\frac{1}{l'} = \frac{(n-1)}{r} - \frac{n}{l} \tag{3.1.2}$$

where l is the object distance, l' is the image distance and r is the radius of the silicon lens. n is the refractive index of silicon in THz region, the value is about 3.5. Filling the values into the equation, we can get

$$\frac{1}{l'}=\frac{2.5}{6.75}-\frac{3.5}{8.705}\Rightarrow l'=-31.548mm$$

Therefore, the imaging point is located in the left side of GaAs substrate and the distance L is 31.548-8.705 = 22.843mm. If the focal length of the first parabolic mirror is 7.5cm, we have to make it short to 7.5-2.284 = 5.216mm.

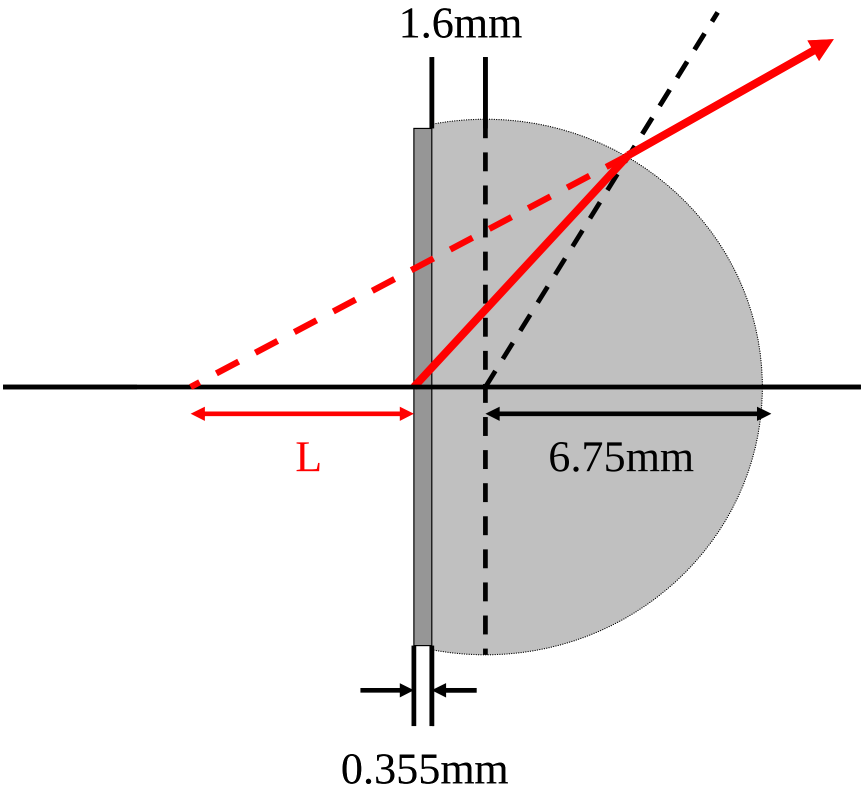

Fig. 3-4 The schematic diagram of silicon lens and GaAs substrate. The radius of silicon lens is 6.75mm and the total thickness is 8.35mm. The thickness of the wafer is 0.355mm. The imaging point of the dipole antenna through the silicon lens is located in the left side with L distance.

The effective focal length of the first parabolic mirror is very critical, so we strongly recommend that combining the emitter with the object lens in one stage shown in Fig. 3-5. That will be convenient for avoiding missing the focus of femtosecond laser on the photoconductive antenna when aligning the effective focal length of the first parabolic mirror.

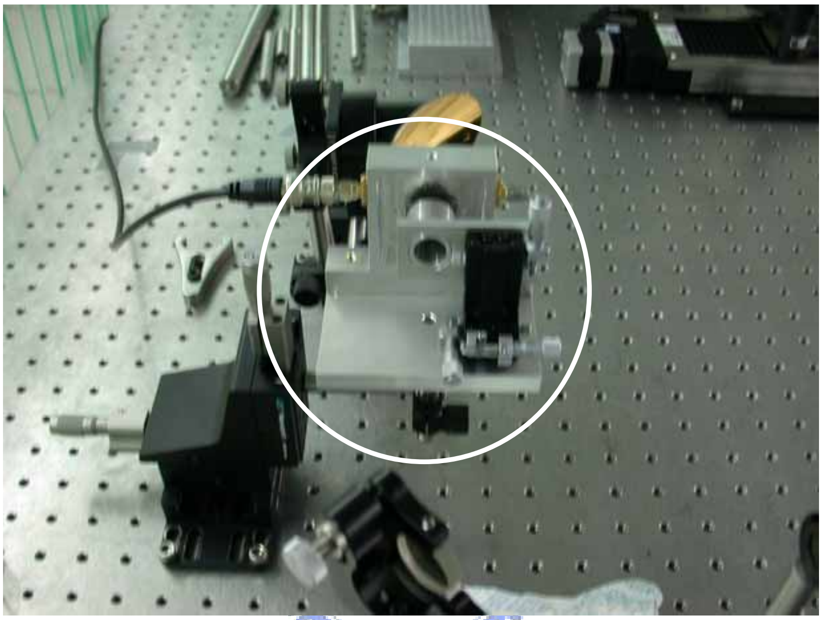

Fig. 3-5 Photo of the setup of the THz emitter and the object lens. The emitter is combined with the object lens in one stage.

In our system, THz wave is parallel between two parabolic mirrors, the MHA is place on the middle of the optical path. We put a pinhole beyond the sample in order to control the THz beam size passing through the MHA. Assuming that the THz beam was spatial Gaussian distribution, the THz radiation can be considered as a plane wave, i.e. normal incident to the sample, as shown in Fig. 3-6. For convenience, we define the transmission direction is z-axis and the periodical structures is distributed in x-y plane.

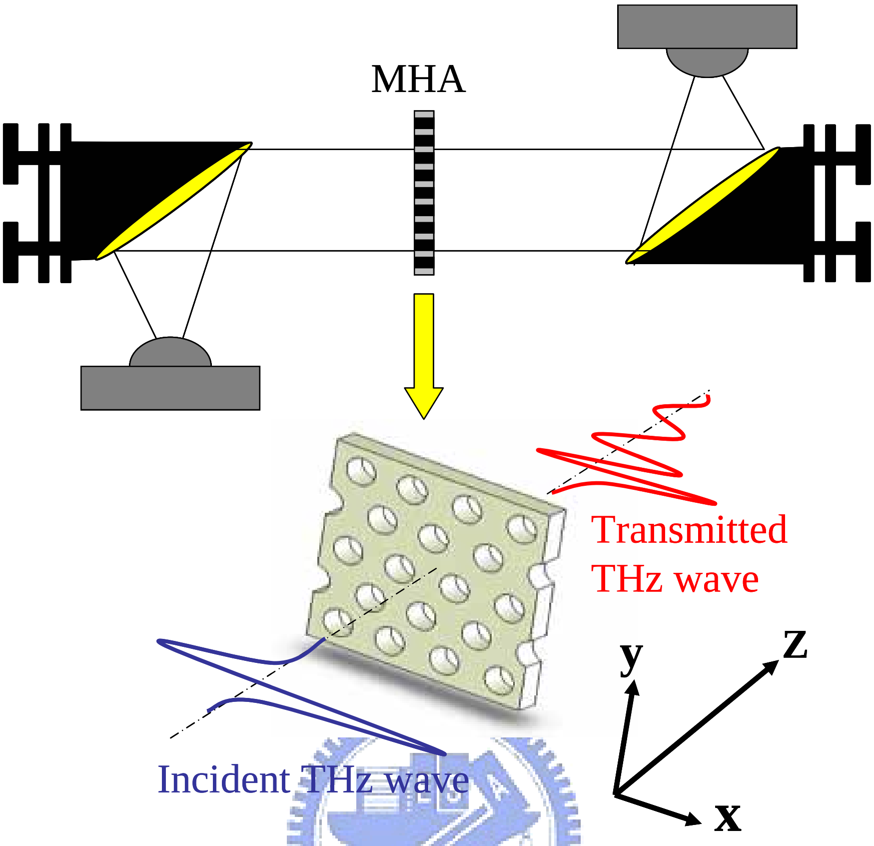

Fig. 3-6 Schematic diagram of the transmission properties of THz wave through MHA. THz wave is parallel between two parabolic mirrors and normal incident to the sample.

We measure THz radiation propagating through MHA or not as a signal or a reference, respectively. Two time-domain waveforms can be used to obtain frequency-domain spectra using numerical fast Fourier transform, and then the MHA signal divided by the reference in frequency domain should be the transmittance of this sample. The transmission properties of certain sample with a board band frequency spectrum can be observed. From the above steps, we can obtain the basic transmission properties of MHAs.

3.2 The Structure of MHAs and the sample fabrication

Our sample is a aluminum film perforated periodically with hexagonal lattice of circular holes shown in Fig. 3-7, and the photo of the real sample is shown in Fig. 3-8. The spacing between holes ,s is 995 μm and the diameter of holes ,d is 565 μm. The thickness of MHA ,t is about 500 μm. These parameters can be controlled to change the transmission properties of MHA.

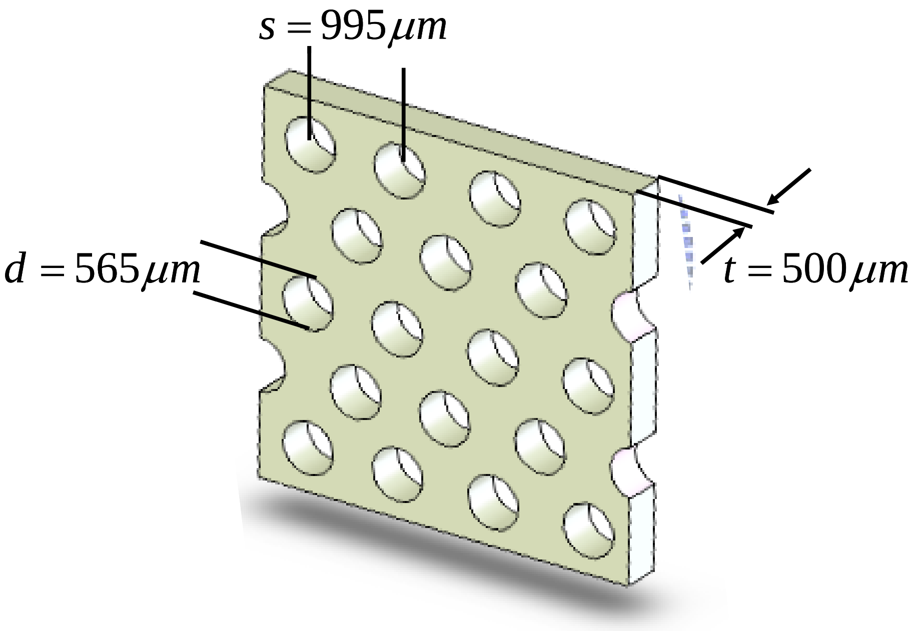

Fig. 3-7 The structure of MHA. hole diameter d=0.56 mm, lattice constant s=0.99 mm, and thickness of the metal plate t=0.5 mm

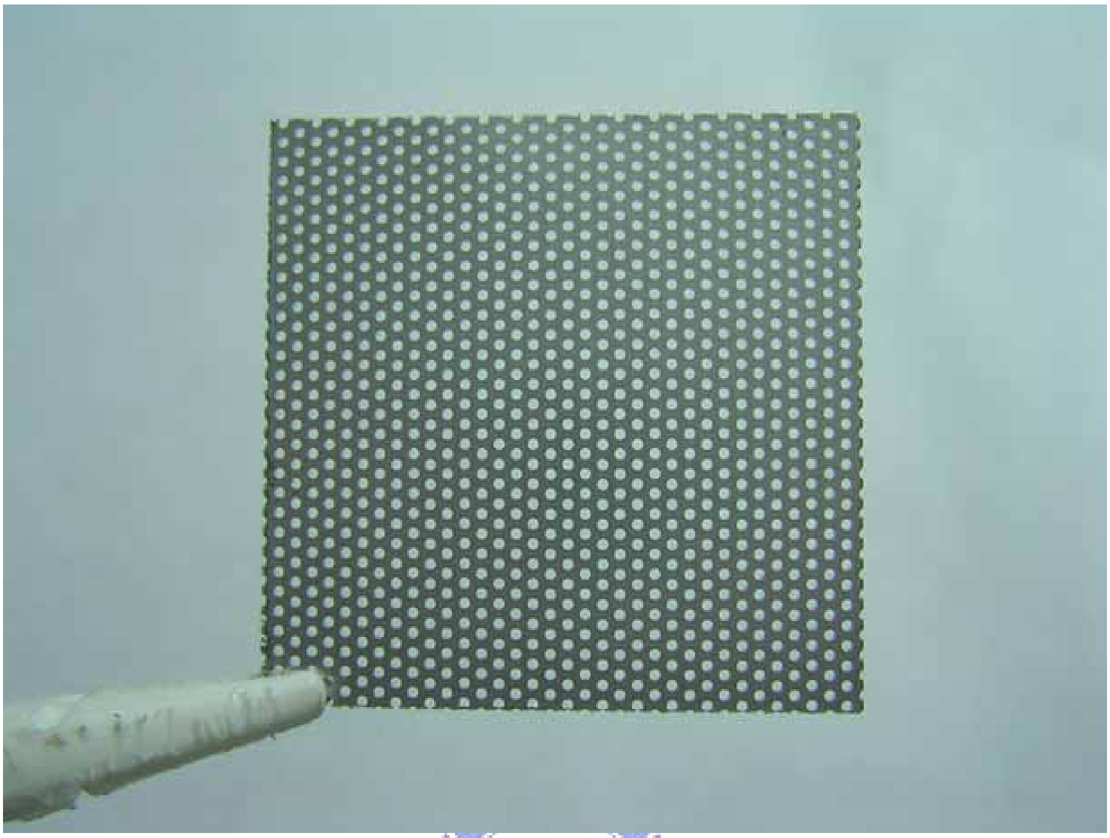

Fig. 3-8 The photo of the real MHA sample.

In order to investigate the effect of hole material on MHA, we filled UV-gel into the holes. The UV-gel we used is produced by Norland company and the number of this product is 68. The reason we chose UV-gel is due to the negligible absorption and the flat curve of dielectric function. The procedure of filling UV-gel into the holes of the MHA is shown below and drawn in Fig. 3-9.

1. We let the MHA lay on the UV-gel from top to bottom in order to avoid producing the bubble within the UV-gel.

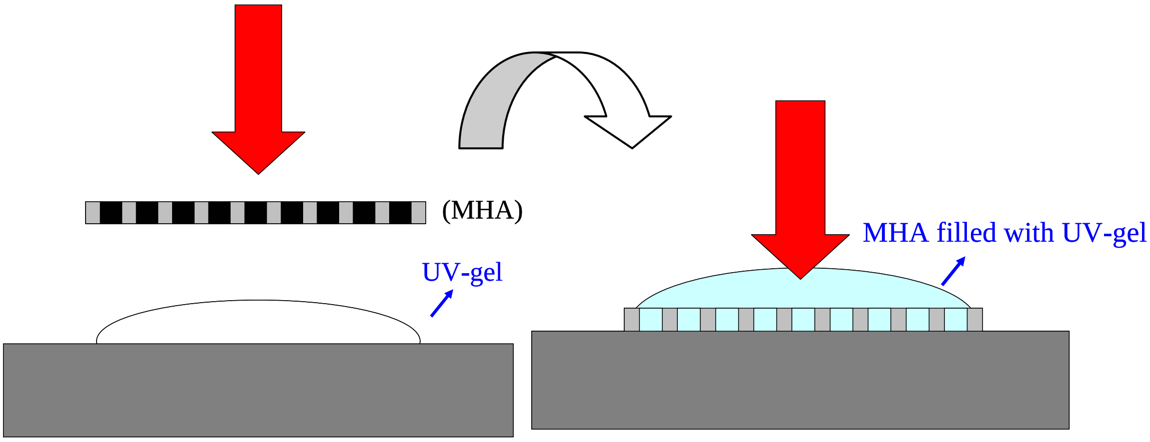

Fig. 3-9 (a) Procedure 1 of fabricating the MHA which holes filled with UV-gel. Let the MHA lay on the UV-gel from top to bottom, and then a MHA filled with UV-gel can be obtained.

2. Devising a mold for fixing the MHA to benefit thinning the thickness of the MHA.

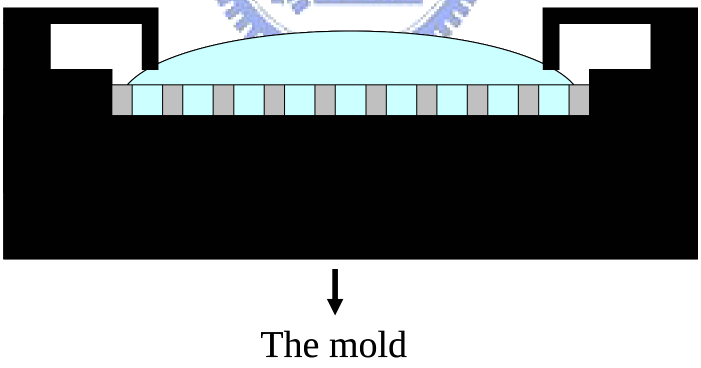

Fig. 3-9 (b) Procedure 2 of fabricating the MHA which holes filled with UV-gel. Devising a mold for fixing the MHA.

3. Using the miller to drill the MHA, and to obtain a thickness t of the MHA which holes filled UV-gel we want by controlling the miller.

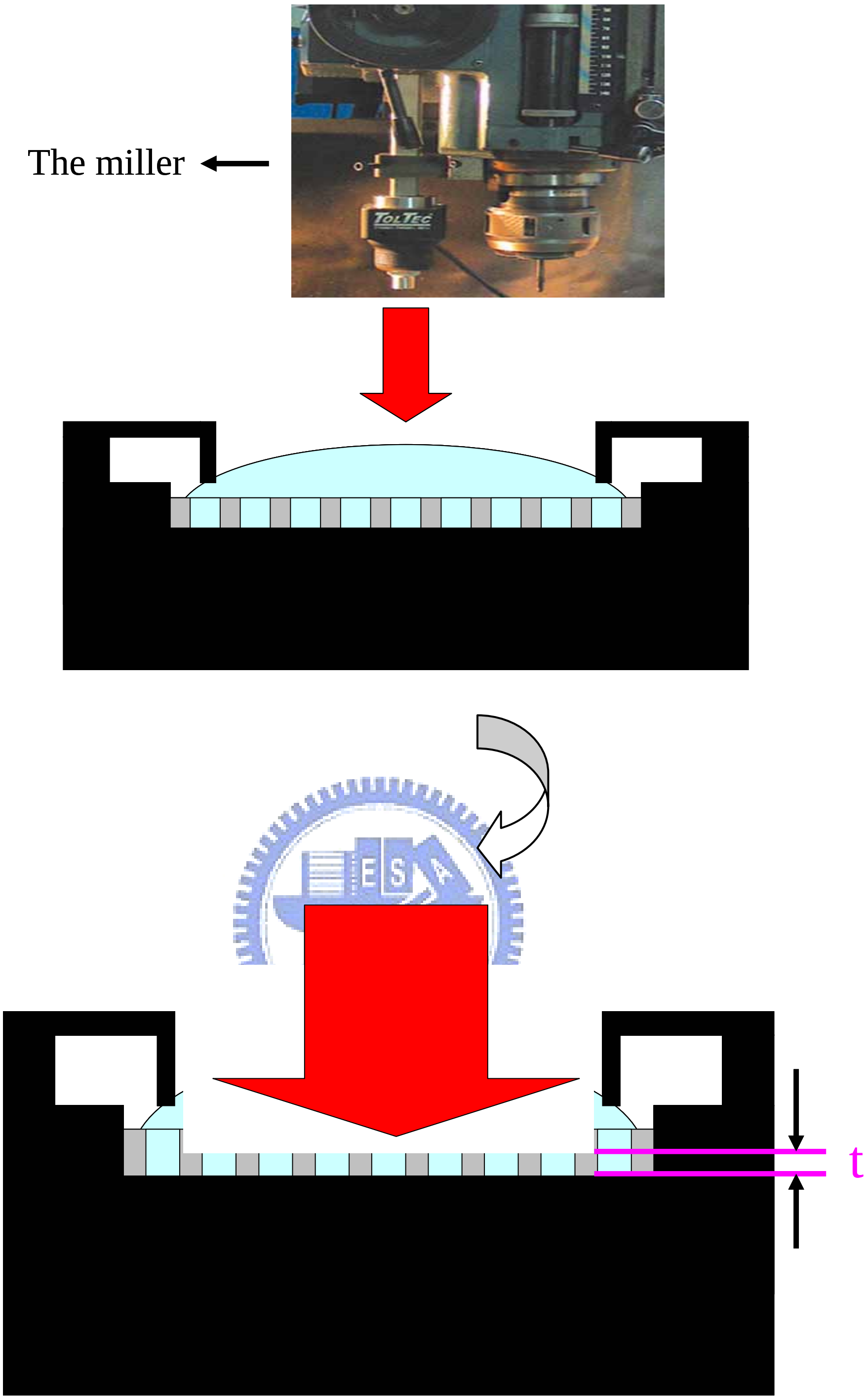

Fig. 3-9 (c) Procedure 2 of fabricating the MHA which holes filled with UV-gel. Using the miller to drill the MHA, and to obtain a thickness t we want.

The photo of the real sample is shown below.

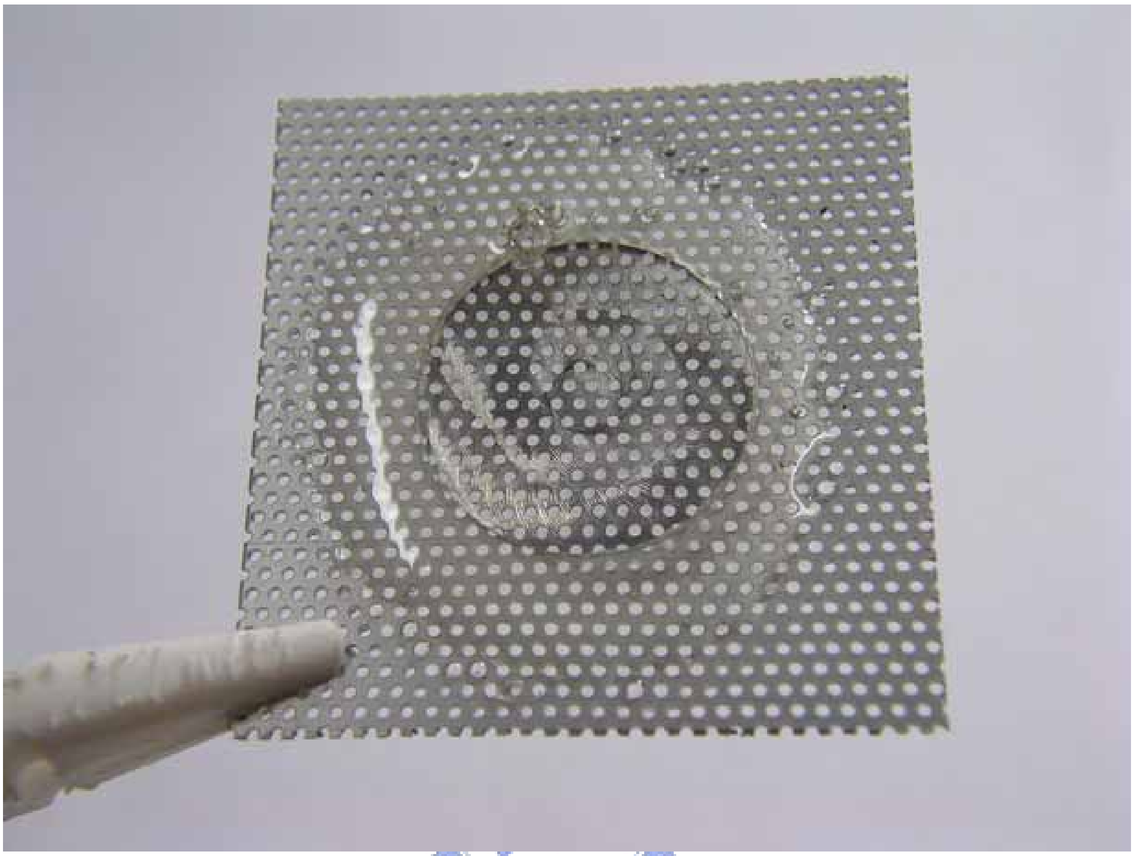

Fig. 3-10 The photo of the MHA with expected thickness which holes filled with UV-gel.

3.3 Parameters of FDTD Algorithm

The equipment of our computer is P4 2.4GHz with 2G RAM. For convenience, we use the commercial software “FULLWAVE” invented by the RSOFT company to proceed the FDTD simulation. The parameters of the simulation are listed below.

The FDTD method is used to numerically simulate the THz propagation problem. In this approach, the 2D-MHA occupies the space from $z = 0$ to t. Terahertz wave is normally incident in the z-direction from $z<0$ and polarized in the x-direction. The grid spacing for FDTD calculation are 30μm in x and y dimensions and 8μm in the z-direction. For the periodic triangular arrays with period of 990μm, the total computational grid is about 7.5mm × 8.3mm × 0.9mm. The beam size is 6mm which is large enough to avoid the finite size effect. The system is defined by specifying the relative dielectric constant, $\varepsilon_R(x, y, z, \omega)$. At first, the hole material and the adjacent medium are air, so we set $\varepsilon R = \varepsilon_{Air} = 1$, and for Aluminum we set $\varepsilon_R = \varepsilon_{Al}(\omega)$ using the Drude model shown in Fig. 3-11 (a). For example, it gives $\varepsilon_{Al} = -3.3820\times104 +2.1882\times106i$ at 0.3THz. Complex refractive index is also shown below in Fig. 3-11 (b). The grids are truncated with uniaxial perfect matching layers to simulate absorption of field components approaching grid edges where appropriate [20].

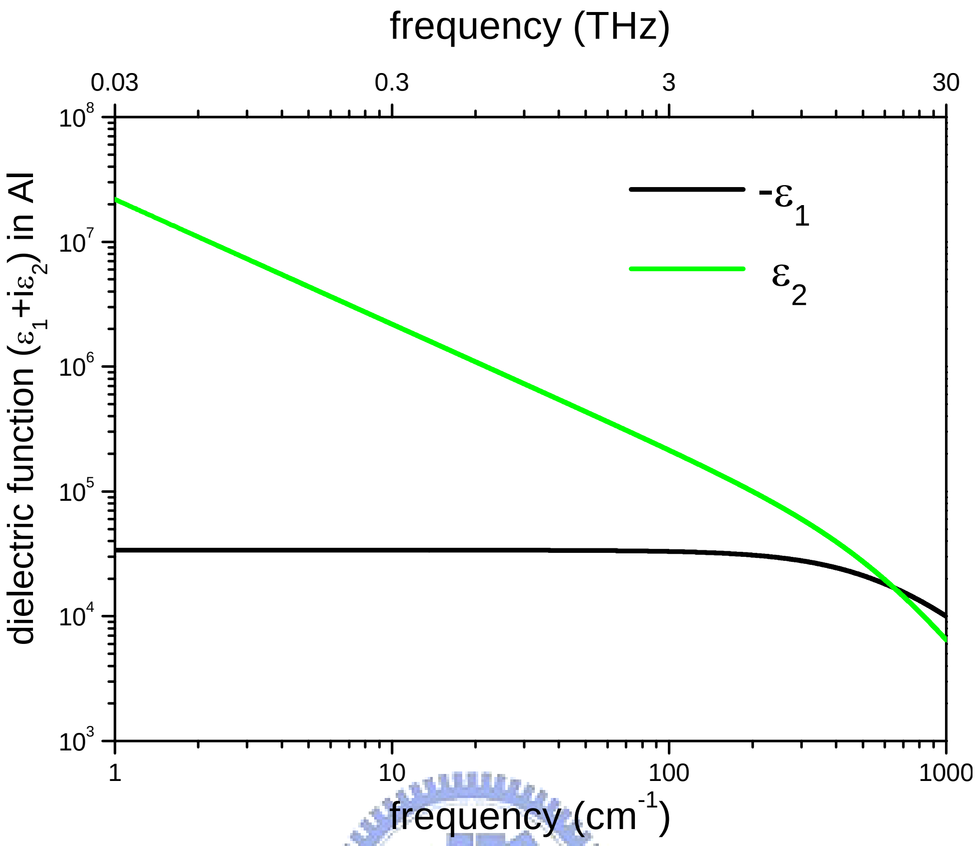

Fig. 3-11 (a) Dielectric function of Aluminum versus frequency.

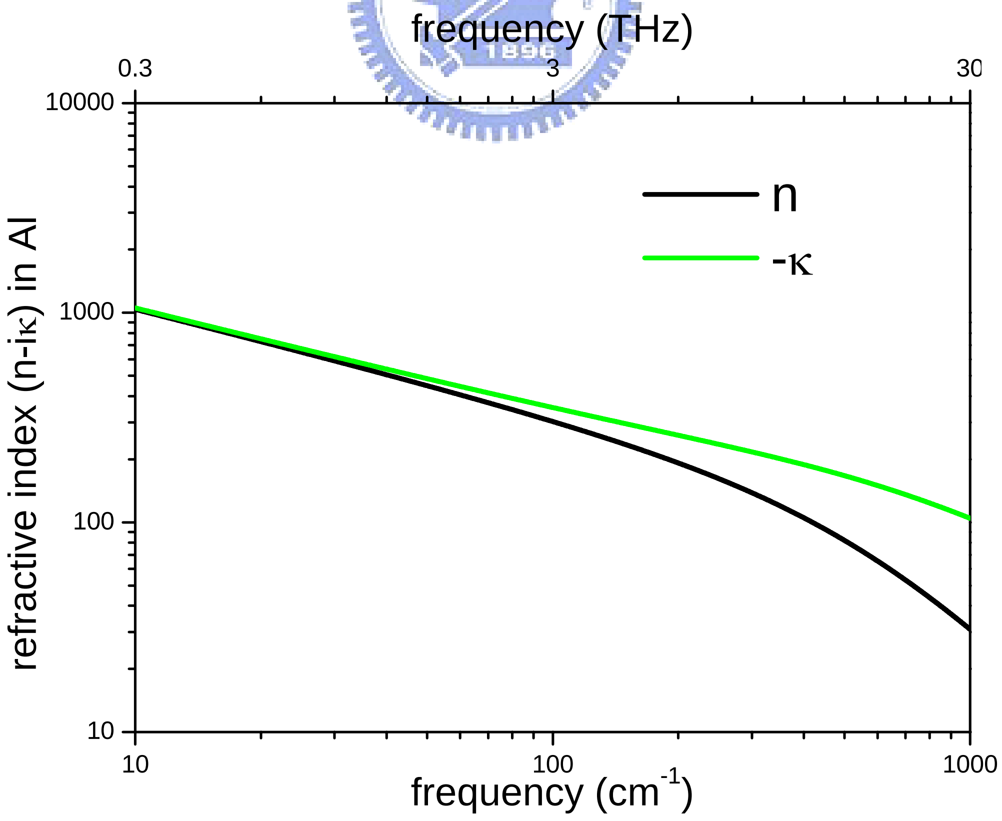

Fig. 3-11 (b) Refractive index of Aluminum versus frequency.

4 Results and Discussion

4.1 Free Space THz-TDS Waveform and Spectrum

THz time domain waveform is shown in Fig. 4-1. The amplitude of oscillations after main peaks are due to the humidity can be seen in the tail of the waveform. It can speculate that the oscillation is caused by water vapor absorption.

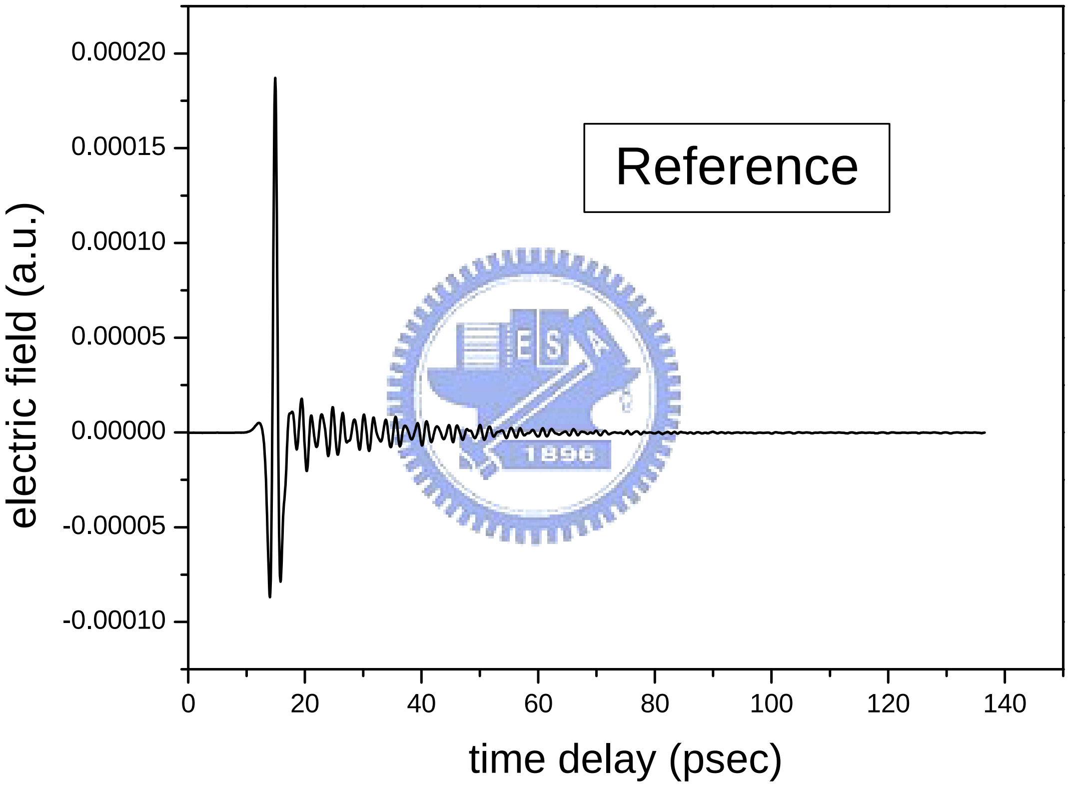

Fig. 4-1 Free space THz time domain waveform

Because of the silicon lens contacted with the substrate of antenna, we can eliminate the reflective signal from the waveform. Then, using numerical fast Fourier transform can obtain the frequency spectrum shown in Fig. 4-2. Some deep dips at 0.556, 0.754, 0.988, 1.113, 1.164, 1.208, 1.230, 1.413 THz are cause by water absorption [25].

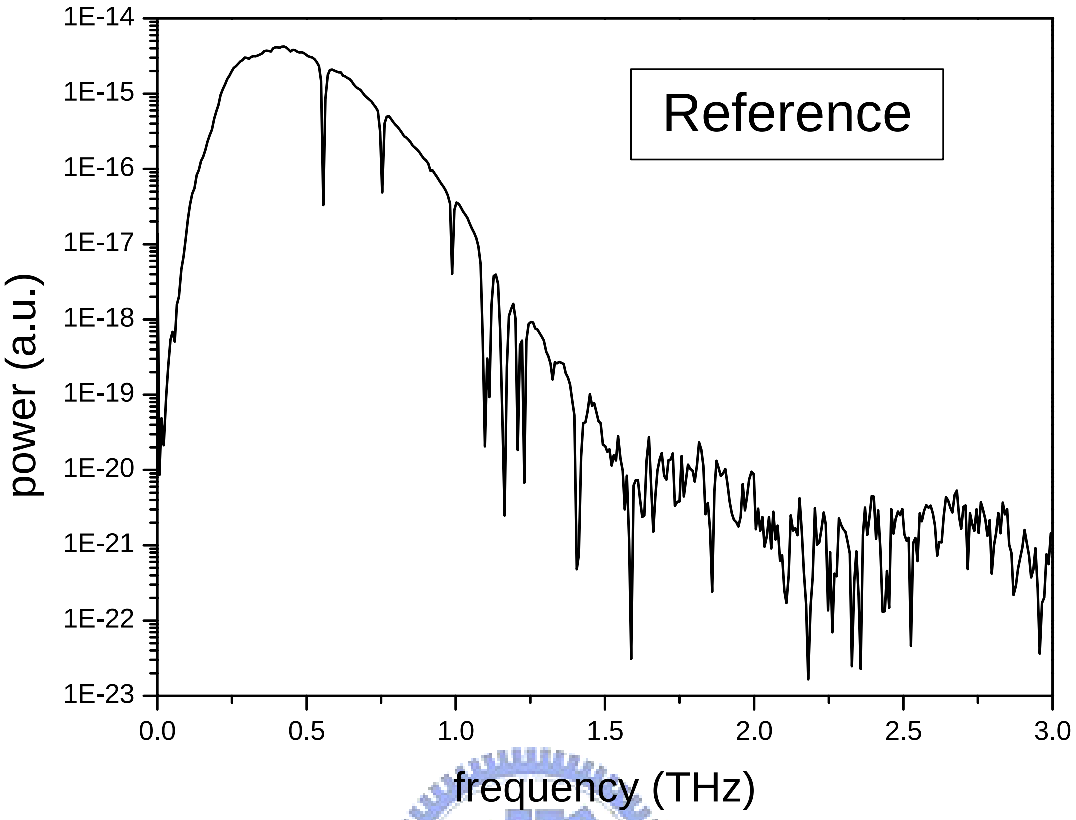

Fig. 4-2 THz frequency domain spectrum

From the frequency spectrum, we can estimate the signal-to-noise ratio in our system is larger than 10^6 and the bandwidth approaches 2THz. Because this spectrum was measured in free space without passing any sample, we call this signal is reference signal.

4.2 Characteristics of MHAs

MHA in THz region is like a band-pass filter, and the normalized transmittance at peak frequency is about 260% to the porosity of the sample. The porosity means the area of holes divided by the total area of illuminating, the value is about 0.29 in our sample. Theory of this extraordinary phenomenon is still unclear; the widespread explanation is the coupling between the incident electromagnetic wave and surface plasmon polariton. Recall the equation (2.2.26) about the resonant peaks in triangular structure,

$$\lambda_{\max} = a_0[\frac{4}{3}(i^2 + ij + j^2)]^{-\frac{1}{2}}\sqrt{\varepsilon_d} \qquad (2.2.26)$$

the maximum transmittance only concern with the spacing and the adjacent material. This phenomenon has been verified by experiments, for instance, the peak can be tuned when the adjacent dielectric material is changed from air to tape. However, in this formula, the max. transmittance peak seems to be independent of the thickness of the MHA and the material stuffed with the holes. We want to check this point ,and then some brand-new phenomena happened in our experiments that the formal experiences can’t to expound.

4.2.1 Basic Transmission properties of MHAs

First, we measure the THz waveform in free space as the reference, and then we measure THz propagating through MHA as the siganl. Two time-domain waveforms can be used to obtain frequency-domain spectra using numerical fast Fourier transform, and dividing MHA signal by the reference in frequency domain will be the transmittance of this sample. The transmission properties of certain sample with a board band frequency spectrum can be observed. From the above steps, we can obtain the basic transmission properties of MHAs.

From the above steps, we can obtain the basic transmittance properties of MHAs shown in Fig. 4-3 (a) is the time domain signal compared with the reference. (b) is the frequency domain signals via the

FFT from (a). (c) is the power transmittance, we can observe a obvious characteristic of band-pass filter, and the magnitude of the peak almost get up to 100%. The little peaks at 0.55 and 0.75THz are the inaccuracies owing to the water absorption.

The finite time extent of the terahertz pulse scans, 136 ps (in 1024 steps), limits the frequency resolution of the numerical Fourier transforms in THz-TDS. To perform a numerical interpolation between the measured frequency points, the measured pulses in the time domain were extended with zeros (zero padding) [11] to a total time duration of 1500 ps.

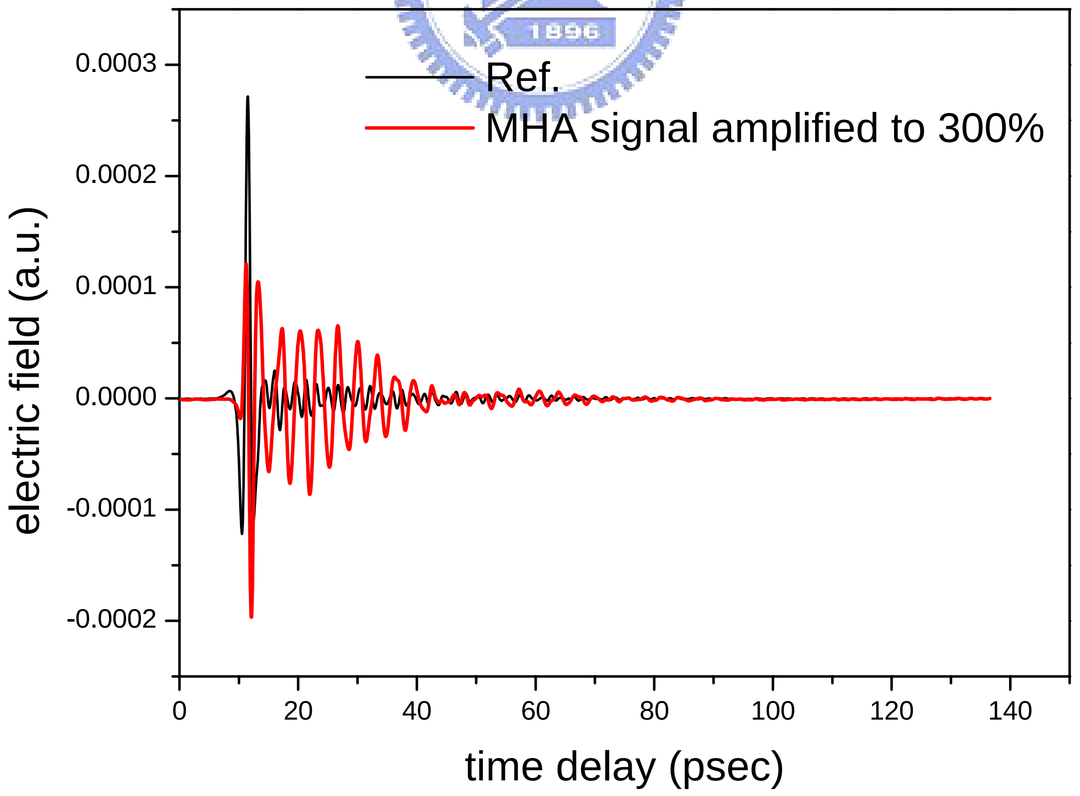

Fig. 4-3 (a) The time domain signal compared with the reference

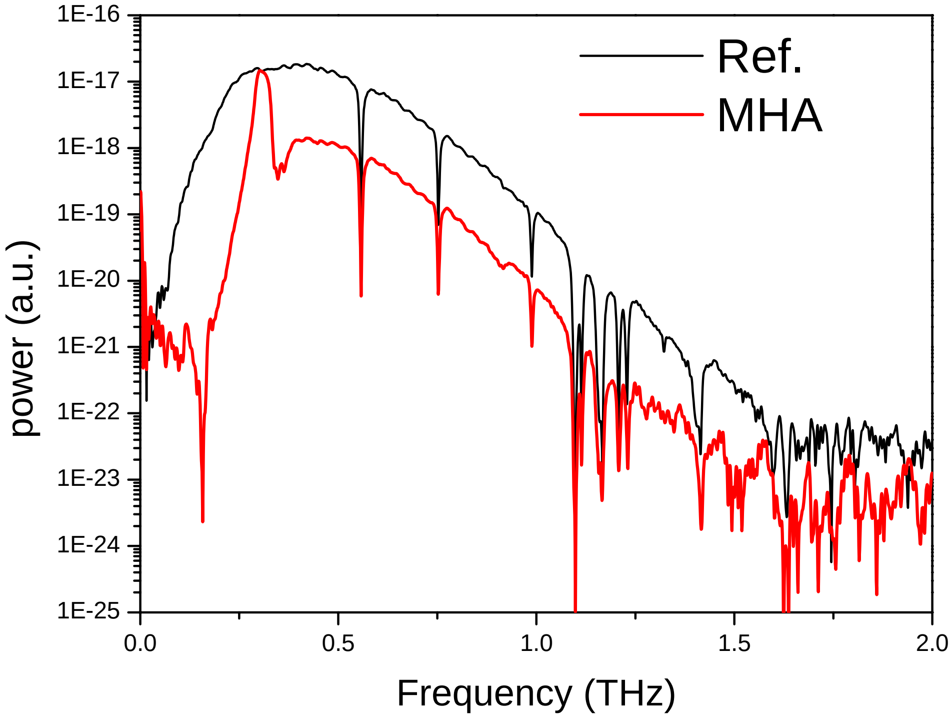

Fig 4-3. (b) The frequency domain signals via the FFT from (a)

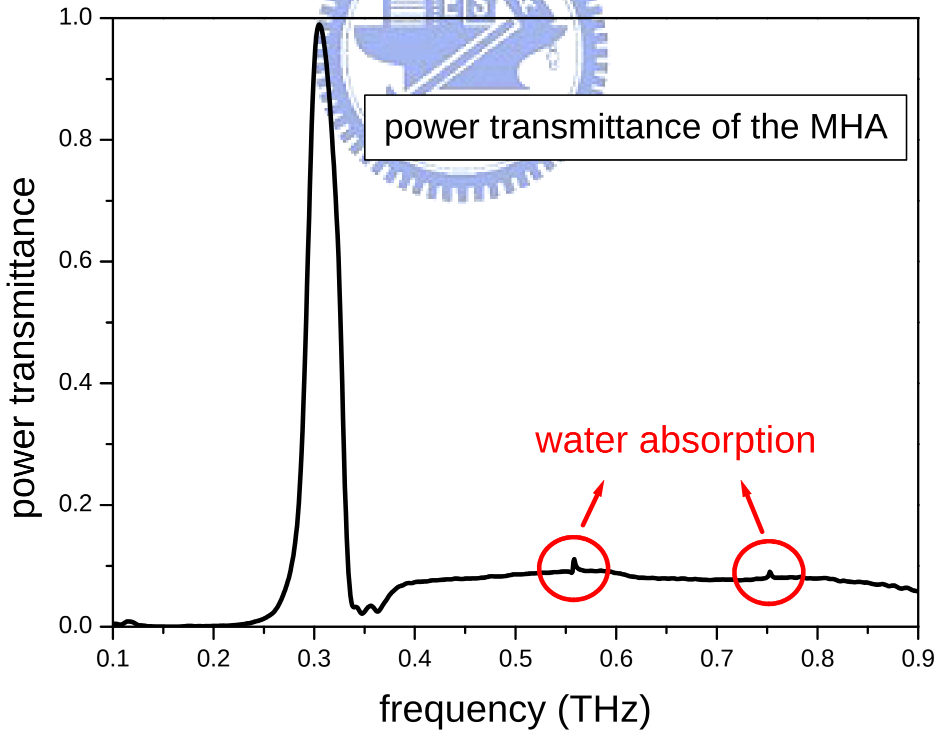

Fig. 4-3 (c) The power transmittance of the MHA. A obvious characteristic of band-pass filter, and the magnitude of the peak almost get up to 100%.

In order to grasp this phenomena more, we use the FDTD algorithm to simulate this structure. It is successful that we got almost the same result compared with the experiments. Owing to the lack of our RAM, the spectral linewidth of the peak is wider slightly than the experiment, but the peak frequency is also located at 0.3THz nearby. So we can affirm that this simulated tool is accurate enough to express the real situation. The simulated results shown Fig. 4-4 (a) is the time domain signal compared with the reference. (b) is the frequency domain signals via the FFT from (a). (c) is the power transmittance.

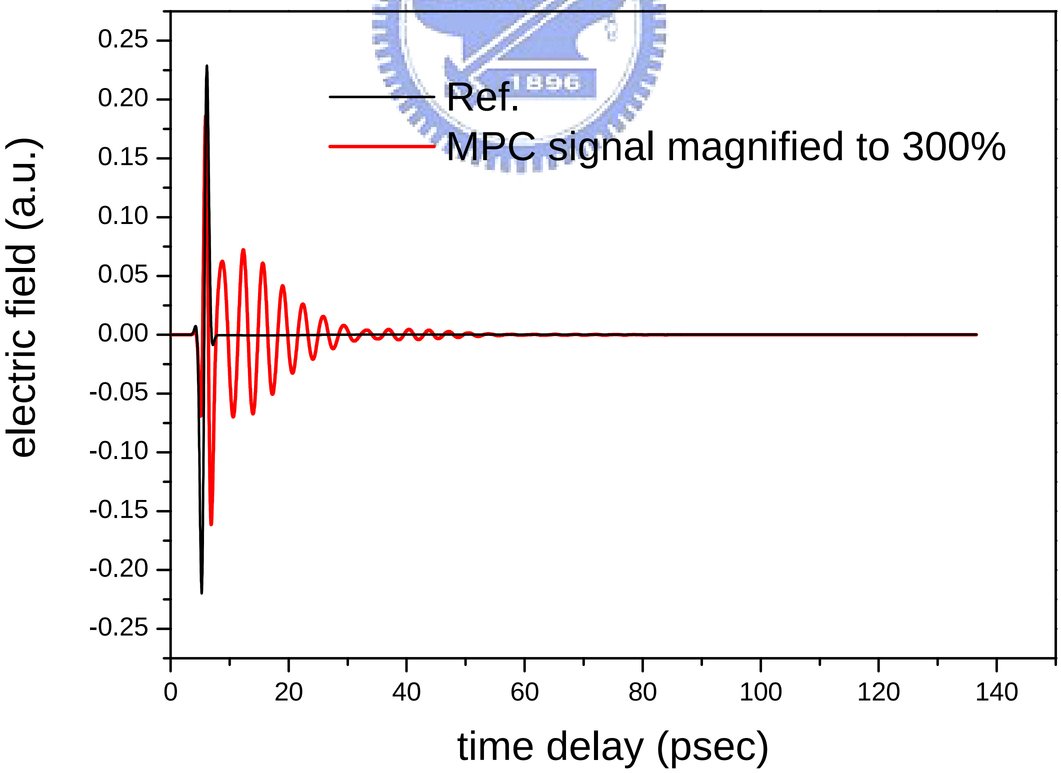

Fig. 4-4 (a) Simulated result: The time domain signal compared with the reference

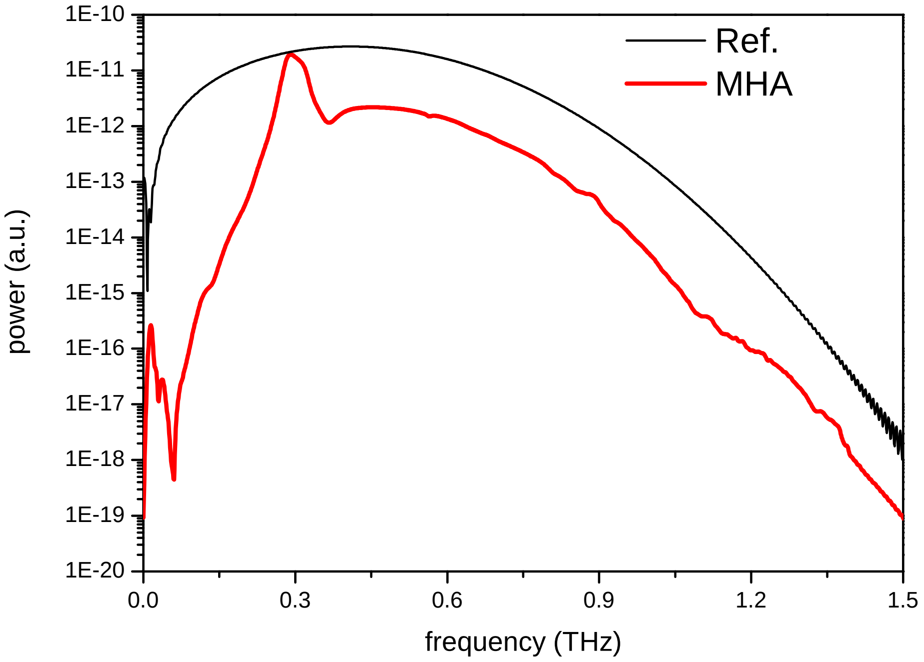

Fig. 4-4 (b) Simulated result: The frequency domain signals via the FFT from (a)

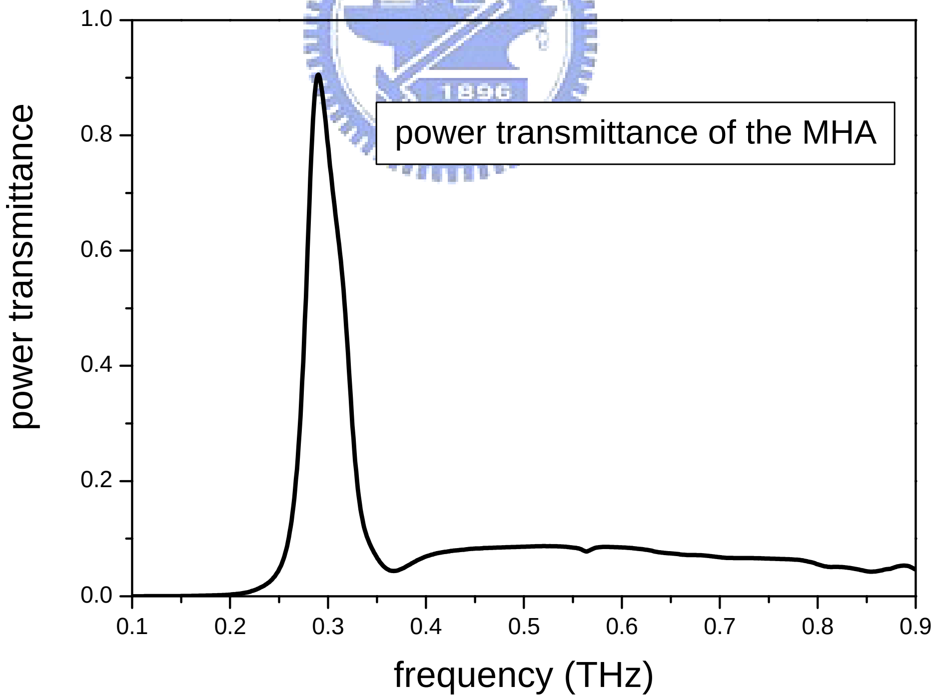

Fig. 4-4 (c) Simulated result: The power transmittance of the MHA. The spectral linewidth of the peak is wider slightly than the experiment, but the peak frequency is also located at 0.3THz nearby.

From both experimental and simulated results above, we can observe a almost monochromatic waveform in time domain that can response to the peak at 0.3 THz in the power transmittance.

4.2.2 Using SPP Model to explain the extraordinary transmission peak

The MHA we used is an Aluminum plate perforated with an array of triangular holes (hole diameter d=0.56 mm, lattice constant s=0.99 mm, and thickness of the metal plate t=0.5 mm). For this sample, the cut-off frequency is ν_{cutoff}=0.311 THz. In Fig. 4-3 (c), we can observe a obvious peak at 0.301THz which is left to the cutoff frequency. The enhanced transmission is commonly believed to be due to the resonant coupling of incident light with SPPs.

Nevertheless, the peak frequency calculated from eq.(2.2.26) is 0.348THz which is not accurate enough to the observed peak at 0.301THz shown in Fig. 4-5 (a). Furthermore, we checked the MHA with cubic arrays with the same parameters (d=0.56 mm, s=0.99 mm, and t=0.5 mm) to the triangular one using FDTD algorithm, the theoretical peaks also laid on the right side to the simulated peaks, as shown in Fig 4-5 (b).

Although the peak positions are not the same with SPP model, they are still very close to each other. And the spacing between the two peaks in Fig. 4-5 (b) show almost identical range. For this reason, we can presume SPPs play an important role in the extraordinary transmissions.

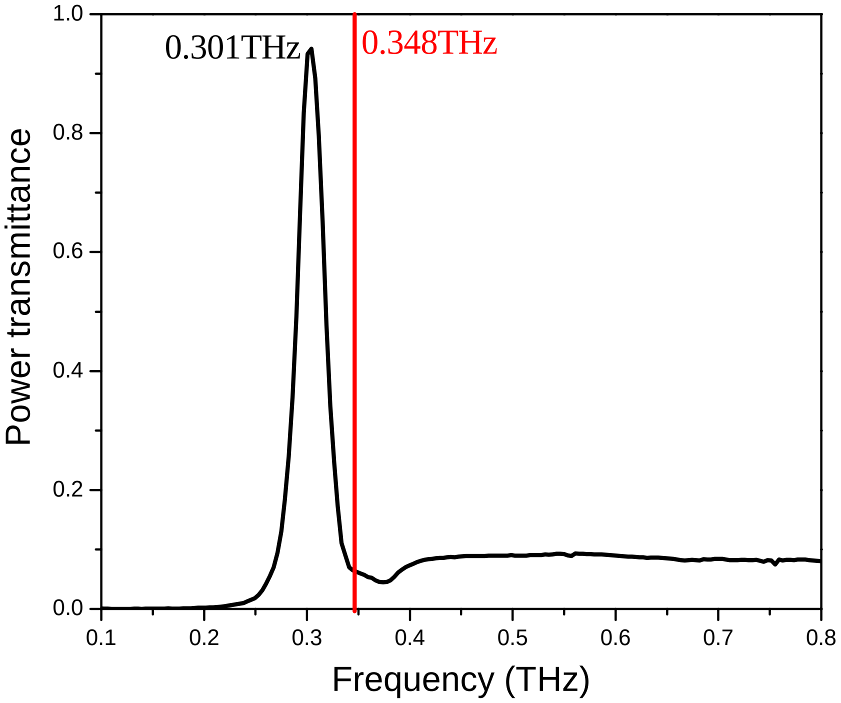

Fig. 4-5 (a) Using SPP model to estimate the transmission peak in the triangular MHA. The peak frequency calculated from eq.(2.2.26) is 0.348THz right to the observed peak at 0.301THz

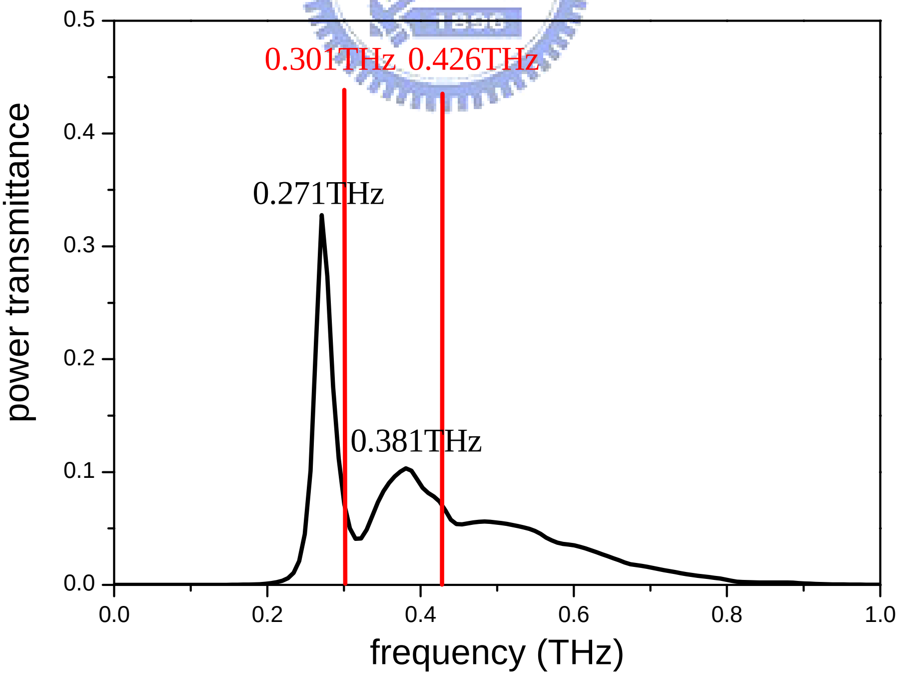

Fig. 4-5 (b) Using SPP model to estimate the transmission peak in the cubic MHA. The peak frequencies calculated both are right to the the observed peaks.

4.2.3 Altering the thickness of MHAs

In order to make sure that the maximum transmittance peak frequency won’t change with the thickness of MPC. We use two different samples to do experiments. The structure of the first sample is s (spacing) =1.13mm, d (diameter) =0.68mm and the second sample is s =0.99mm, d =0.56mm. From the experimental results shown in Fig. 4-6, we find only the cutoff frequency shifts to left, but the peak frequency is almost invariable. This agrees with the prediction from the equation (2.2.26).

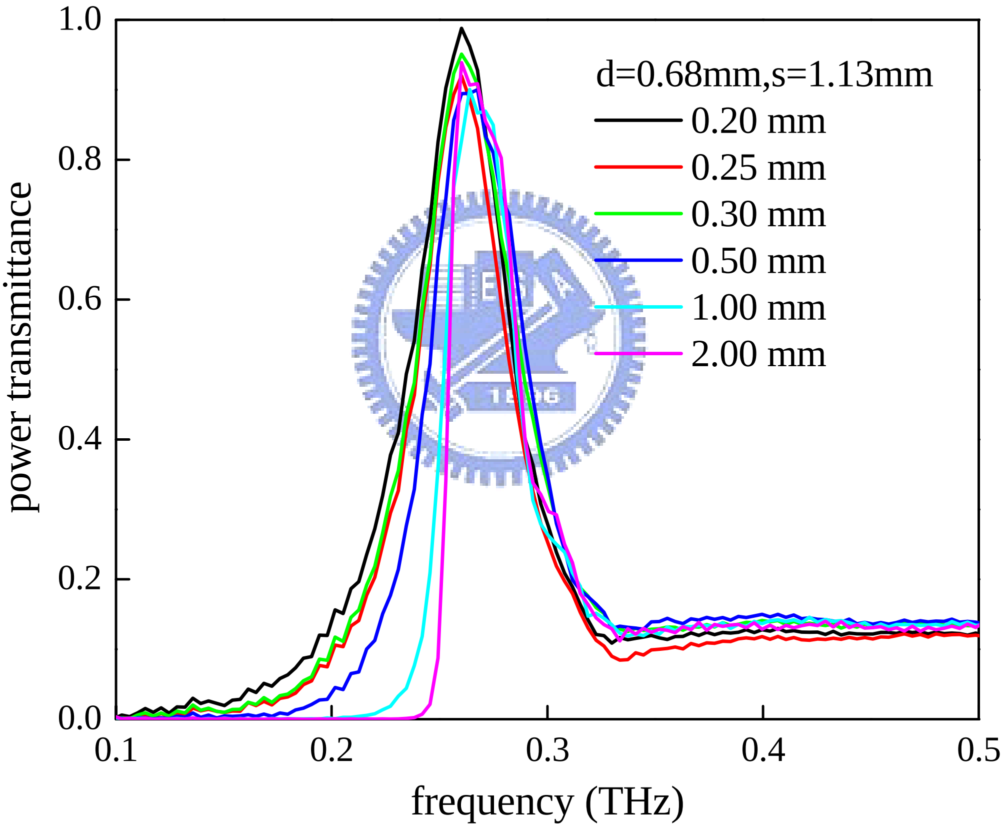

Fig. 4-6 (a) Altering the thickness of the first sample. The structure of the first sample is s =1.13mm, d =0.68mm.

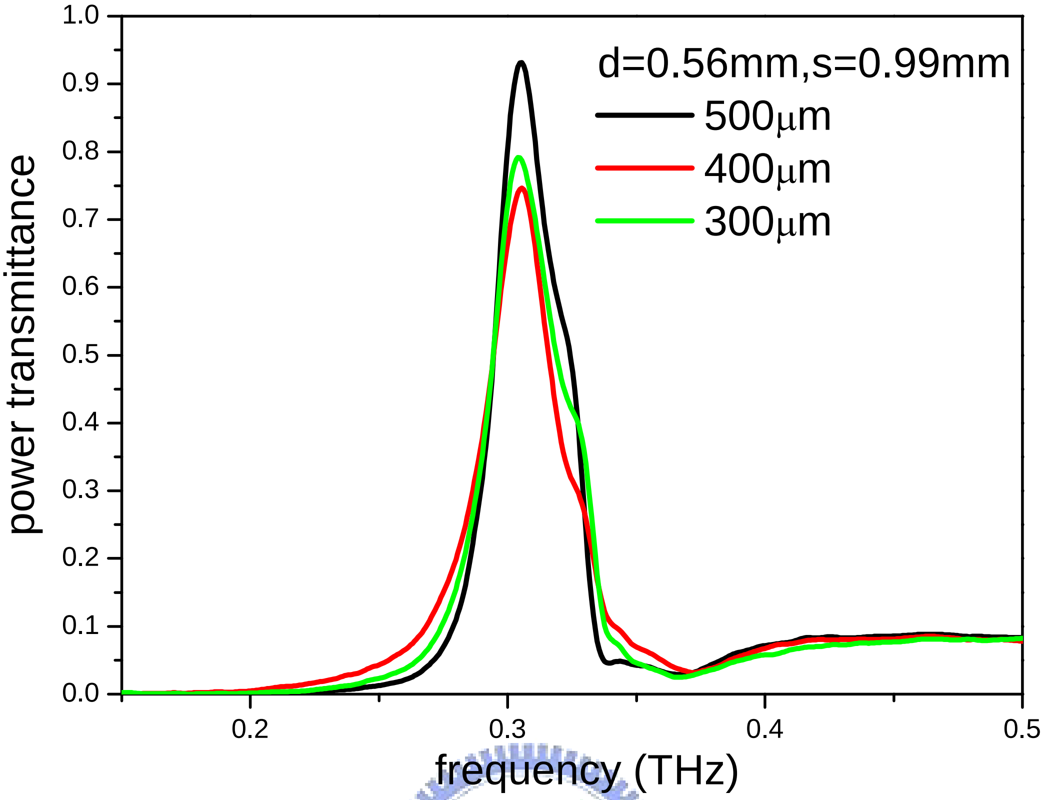

Fig. 4-6 (b) Altering the thickness of the second sample. The structure of the second sample is s =0.99mm, d =0.56mm.

4.3 Features of MHAs when their holes filled up with UV-gel

We recently demonstrated a THz tunable filter by controlling the index of refraction of nematic liquid crystal filling the holes and adjacent to the MHA on one side. New phenomena appeared when holes of the MHA are filled with dielectric material. The effect of filling dielectric material into the holes cannot simply be explained by increased effective hole diameter of the 2D-MHA and equation (2.2.26) also cannot predict the peak frequencies. Therefore, we want to fill some dielectric material into holes of the MHA for studying the effect on hole material.

The optical constants of the UV-gel are very suitable for us to fill it into the holes in MHA. The real part of refractive index is about 1.68, and the attenuation is negligible in our case. The dispersion curve is shown in Fig. 4-7, it seems to be almost non-dispersive in THz region.

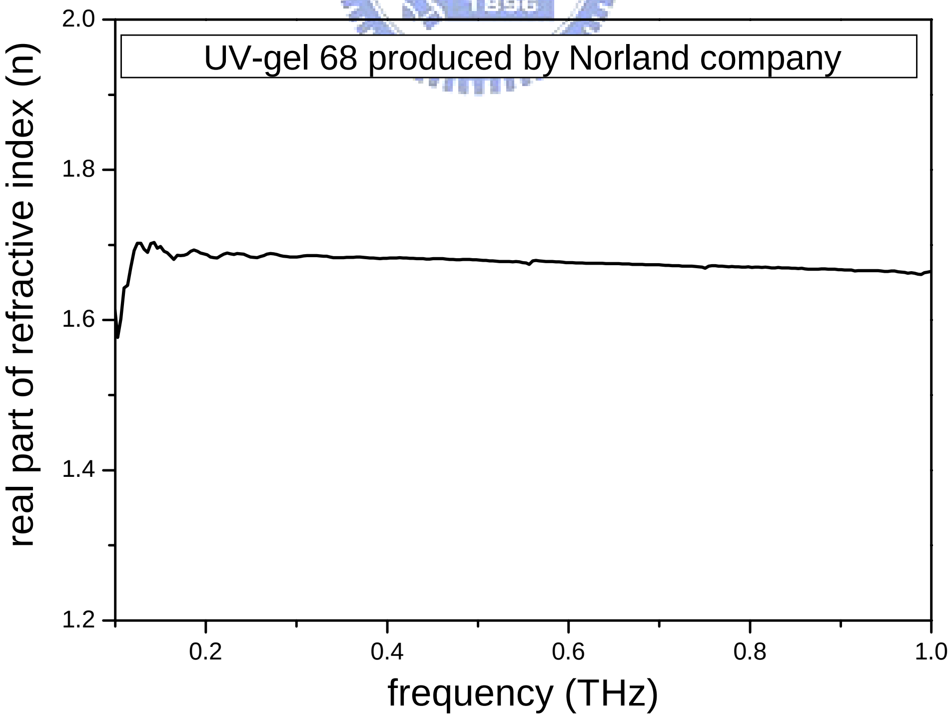

Fig. 4-7 (a) The dispersion relation of the UV-gel in THz region. The real part of refractive index is about 1.68 with almost non-dispersion.

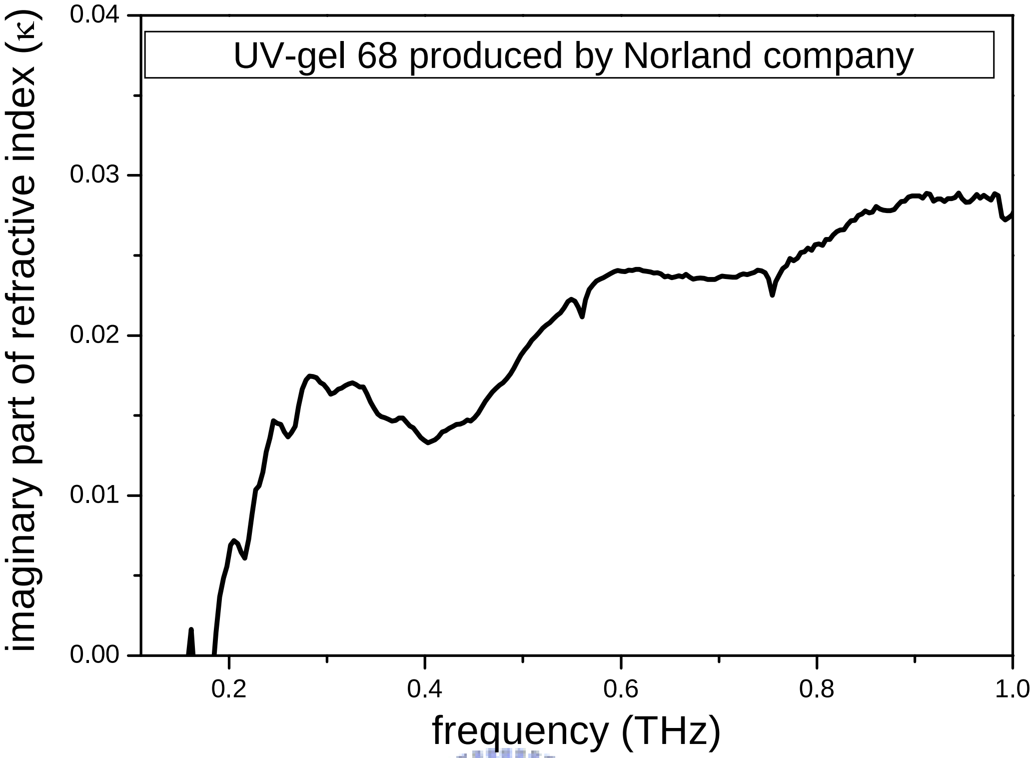

Fig. 4-7 (b) The imaginary part of refractive index of the UV-gel in THz region. The attenuation seems to be negligible in our case.

The imaginary part of refractive index is related to attenuation, and it can be expressed below [26]. Fig. 4-8 shows the attenuation coefficient versus frequency.

$$\alpha = \frac{2\omega\kappa}{c} \tag{4.3.1}$$

where α is attenuation coefficient. And the inverse of attenuation coefficient means the depth of penetration.

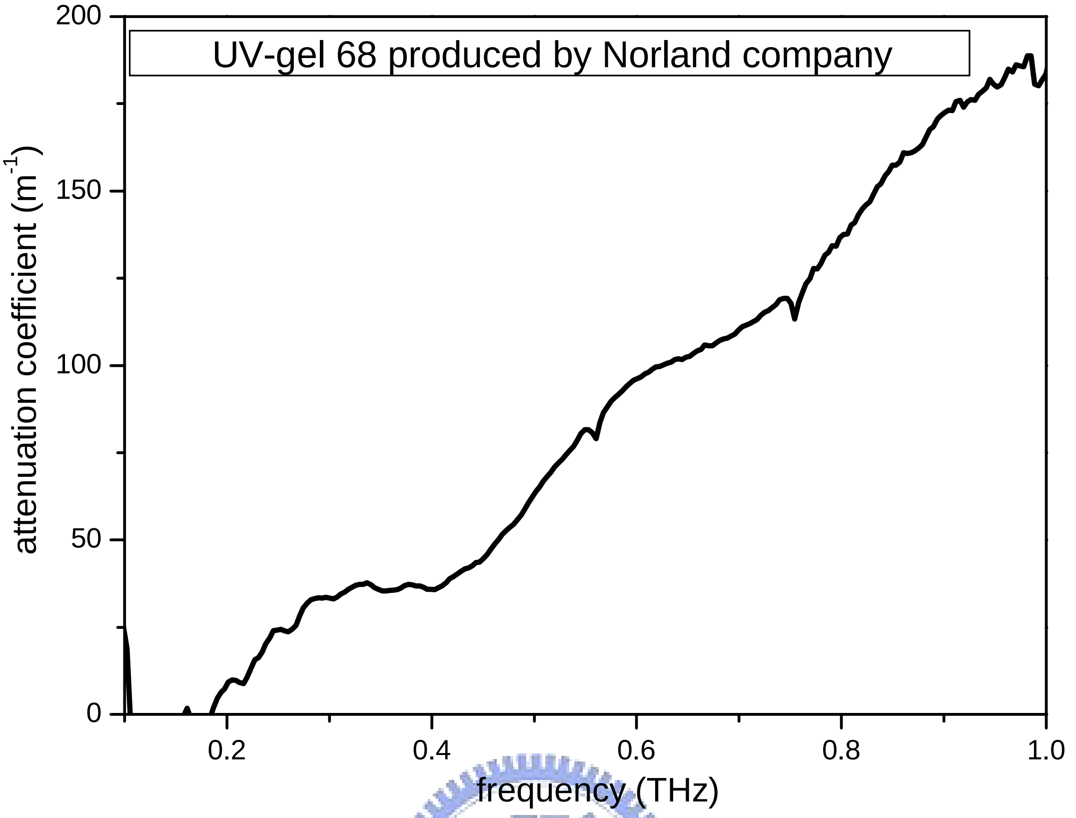

Fig. 4-8 The attenuation coefficient of the UV-gel in THz region.

4.3.1 Transmission Properties When Holes of the MHA Filled with UV-gel

When the holes filled with UV-gel, the effective hole diameter becomes larger, so the cutoff frequency shifts to left. Except for this predictable result, frequency range between the cutoff frequency and the diffraction limit occurs some unusual phenomena. The transmission peak broadened and multi-peak features are observed. The original single transmittance peak changes into three peaks shown in Fig. 4-9. The transmittance of the peaks are reduced, but they are still larger than those according to the porosity (0.29).

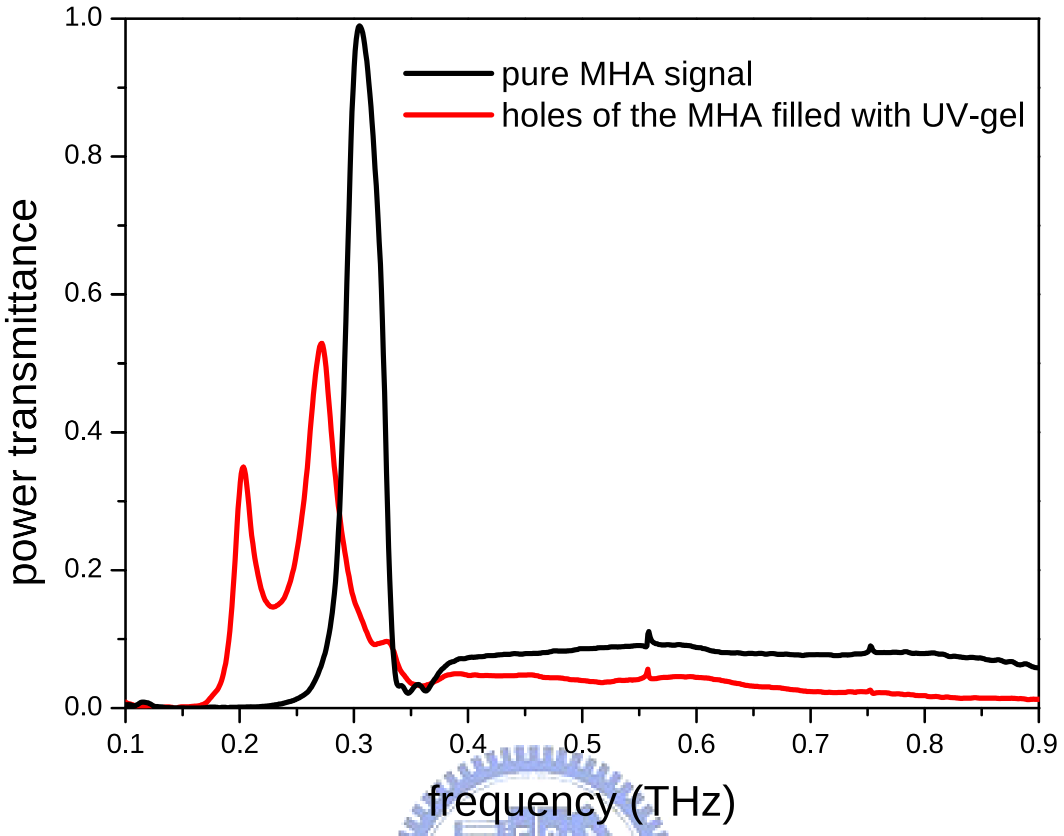

Fig. 4-9 Power transmittance of the MHA which holes filled with UV-gel. The transmission peak broadened and multi-peak features are observed.

For the pure sample, the cut-off frequency is ν_{cutoff}=0.311 THz, but when holes of the MHA filled with UV-gel, the effective hole diameter becomes larger so the cutoff frequency is reduced to 0.311/1.68 =0.185THz. Diffraction limit frequency remains the same due to the changeless lattice constant.

4.3.2 Dependence on Thickness When Holes of the MHA Filled with UV-gel

Further, altering the thickness of MHA will let the peaks shift strongly. With the thickness becomes thinner, all peaks shift to high frequencies and disappear when they approach the diffraction limit. The range of shift seems to be random. Finally, multi-peaks return to one when the thickness reaches around $100\mu m$, as shown in Fig. 4-10.

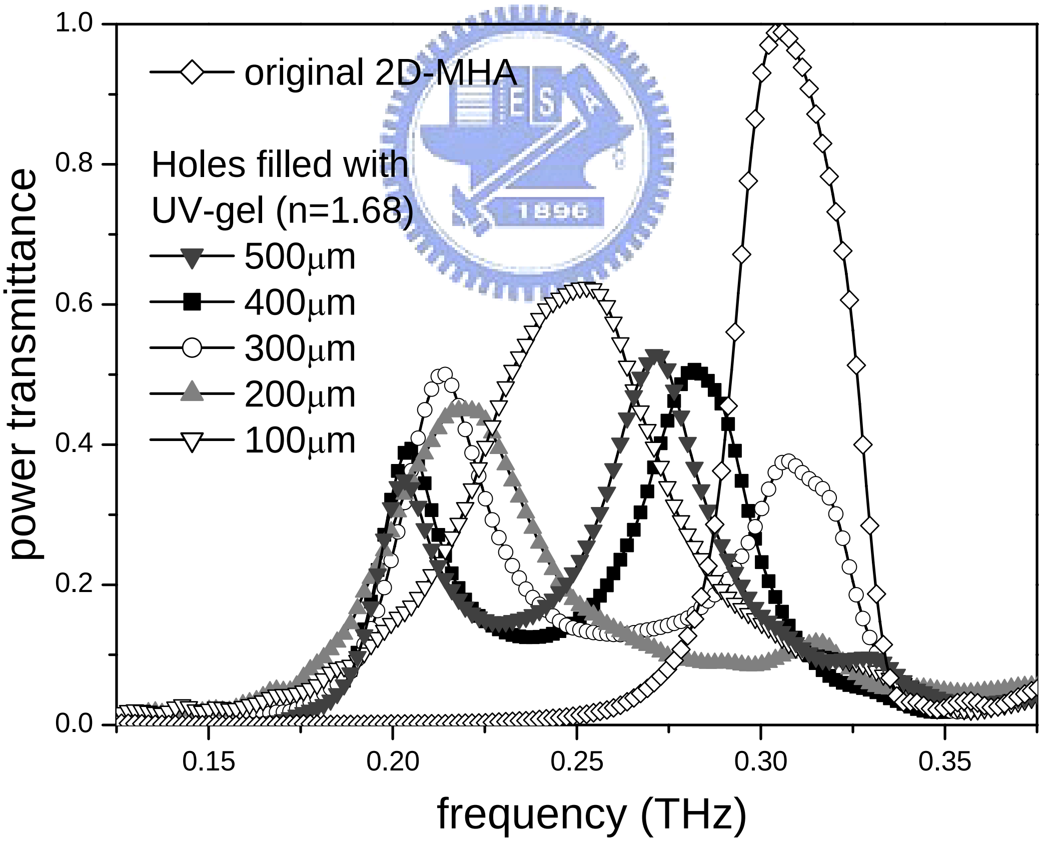

Fig. 4-10 Altering the thickness of MHA when the holes filled with UV-gel. All peaks shift to high frequencies and disappear when they approach the diffraction limit.

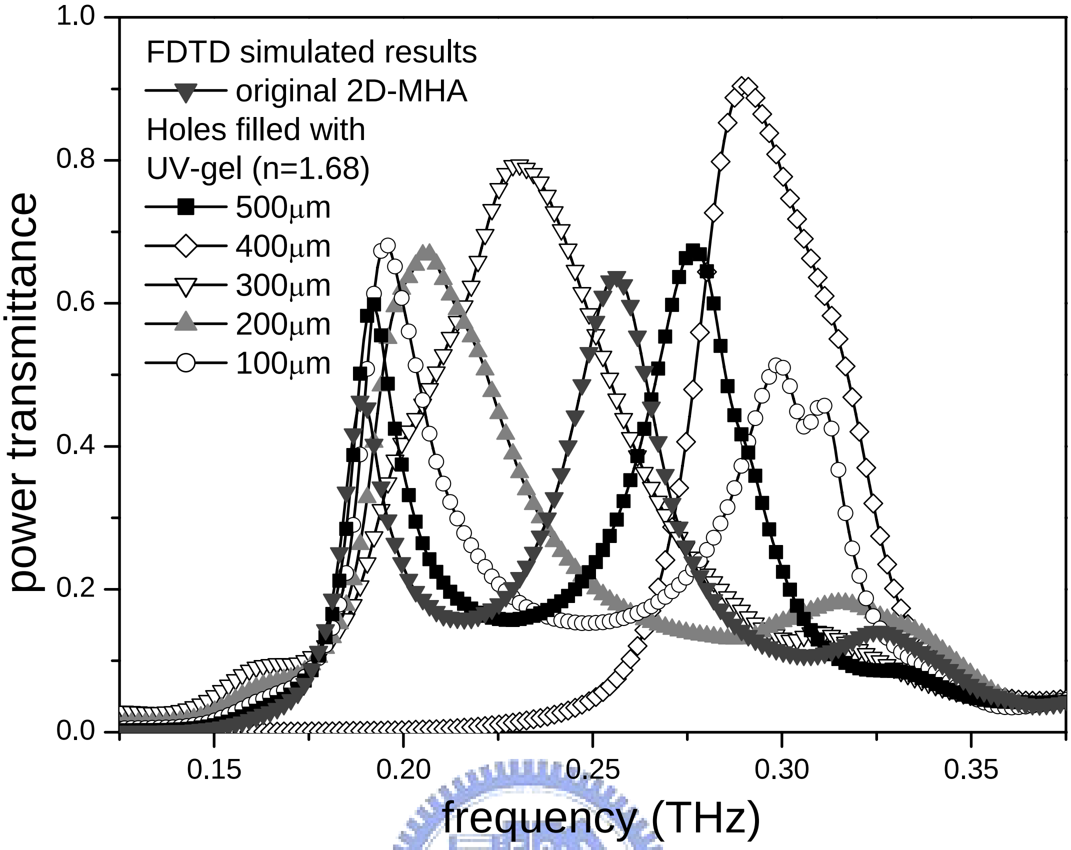

Fig. 4-11 FDTD simulated results: Altering the thickness of MHA when the holes filled with UV-gel. It shows the same trend with experimental results in Fig. 4-9

The simulated results using FDTD algorithm as shown in Fig. 4-11 qualitatively agree with the experimental results. They have the same trend that all peaks shift to high frequencies and disappear when they approach the diffraction limit. However, owing to the rough grids (30μm) in x and y dimensions, the inaccuracy of cutoff frequency will be more obvious in the simulated results. The peak values are lower in experimental results owing to the inaccuracy of sample fabrication.

In order to look for the trend of these phenomena, we aim at the first and the second peaks from left, the first valley, and the spacing between the first and the second peaks, as shown in Fig. 4-12 below.

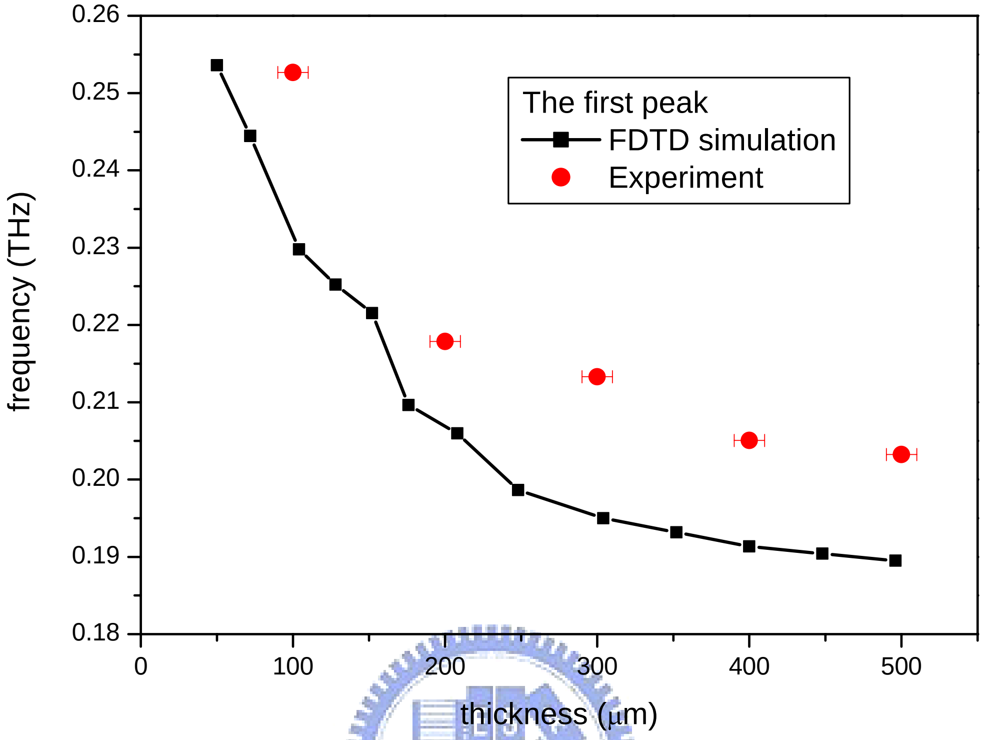

Fig. 4-12 (a) The first peak frequency as the function of the thickness

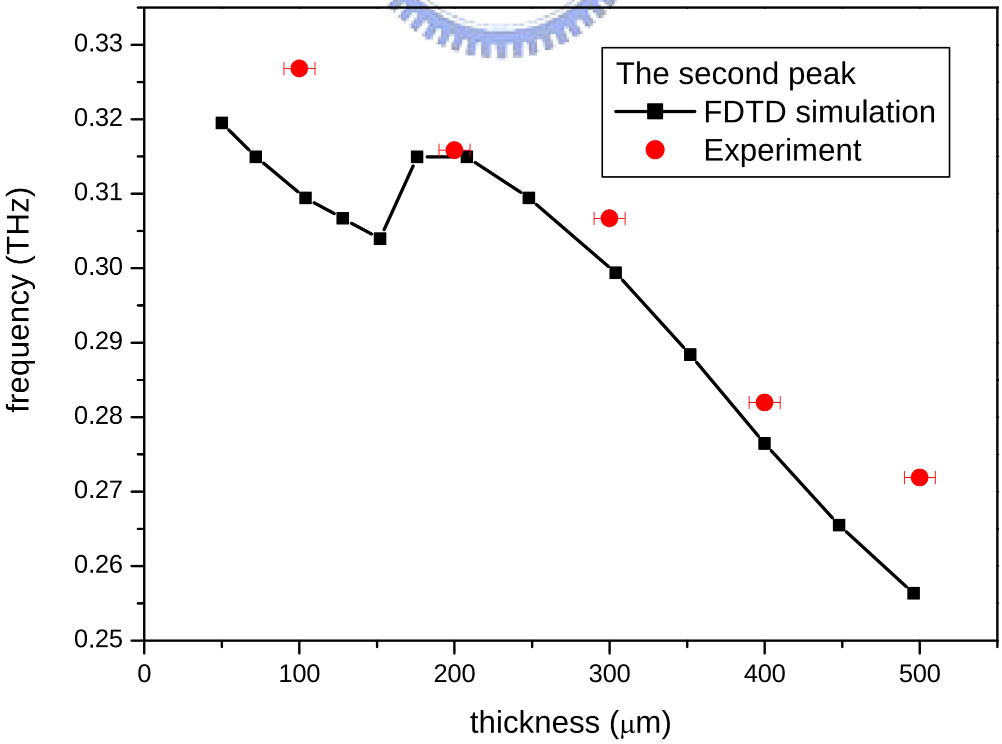

Fig. 4-12 (b) The second peak frequency as the function of the thickness

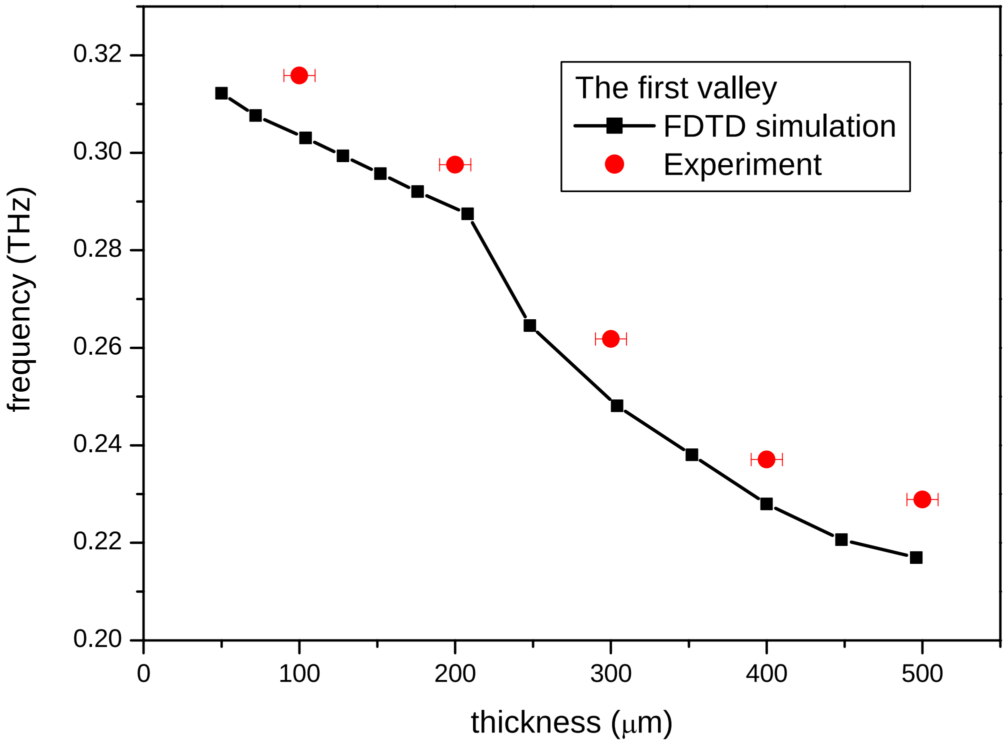

Fig. 4-12 (c) The first valley frequency as the function of the thickness

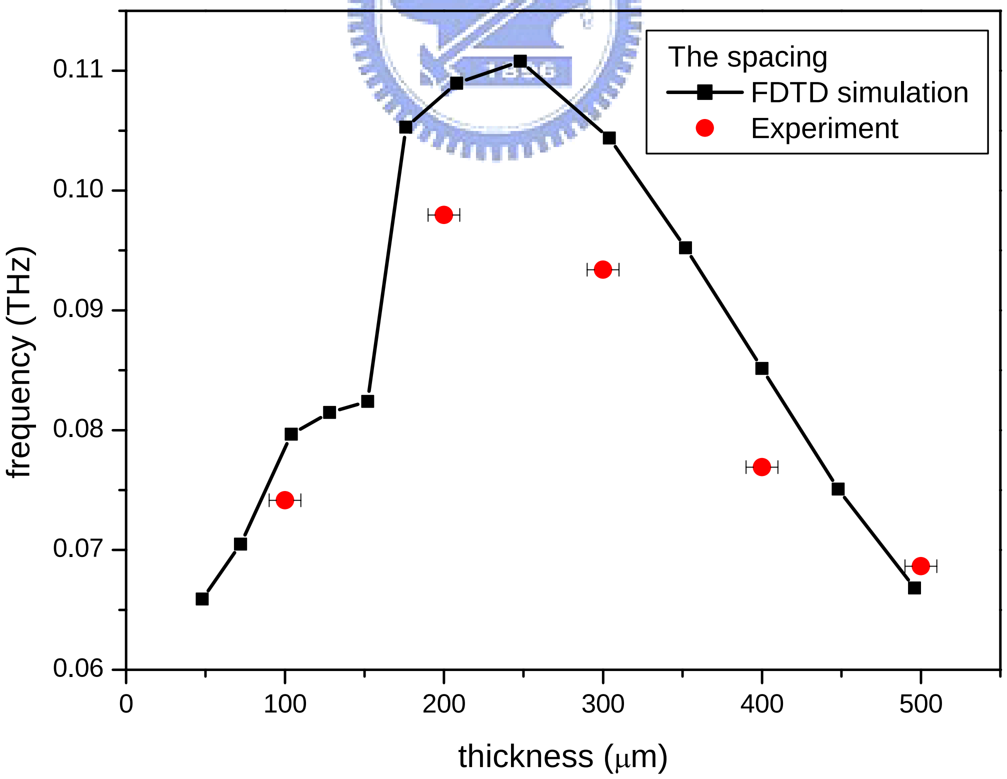

Fig. 4-12 (d) The spacing between the first and the second peaks as the function of the thickness

From the above figures, we can see that there exists a gap, around 200μm, between two distinct regimes. There appears to be a line of demarcation: only one transmission peak is observed when the thickness of the MHA is below 200μm. The first peak from left seems to be depressed by the cutoff frequency. So when the thickness becomes thicker, the shift of the first peak will tend to saturation. And if the thickness is thicker than 200μm, the second peak wavelength seems to be linear with the thickness of MHA.

4.3.3 Changing the adjacent medium When Holes of the MHA Filled with UV-gel

The transmission spectra when we attach translucent Scotch^{TM} tapes on the incident side of 100μm-thick 2D-MHA filled with UV-gel is studied. Peaks shift to the left and decrease as the SPP resonances approach the cutoff frequencies, as shown in Fig. 4-13 (a). Refractive index of the tape is about 1.7 in THz region. These phenomena are analogous with previous reports elucidated in terms of the SPP. However, upon increasing the number of the tape, a side peak on the high frequency side grew gradually and red-shifted shown in Fig. 4-13 (b). For the number of tapes up to fifteen layers, the trend of shift still persists, as shown in Fig. 4-13 (c).

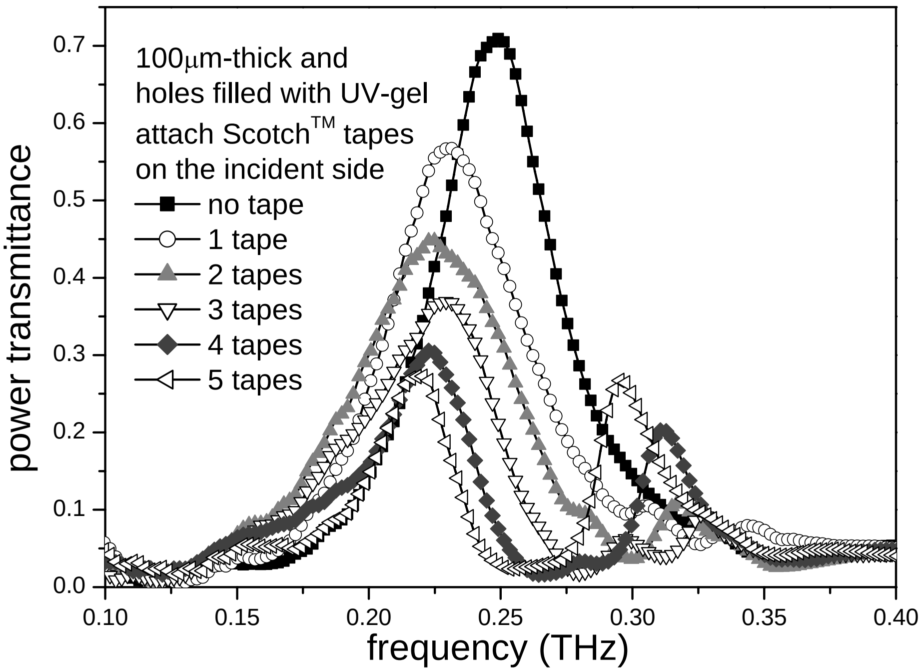

Fig. 4-13 (a) 100μm-thick MHA which holes filled with UV-gel attach different layers of Scotch™ tapes on the incident side. The number of tapes is from zero to five.

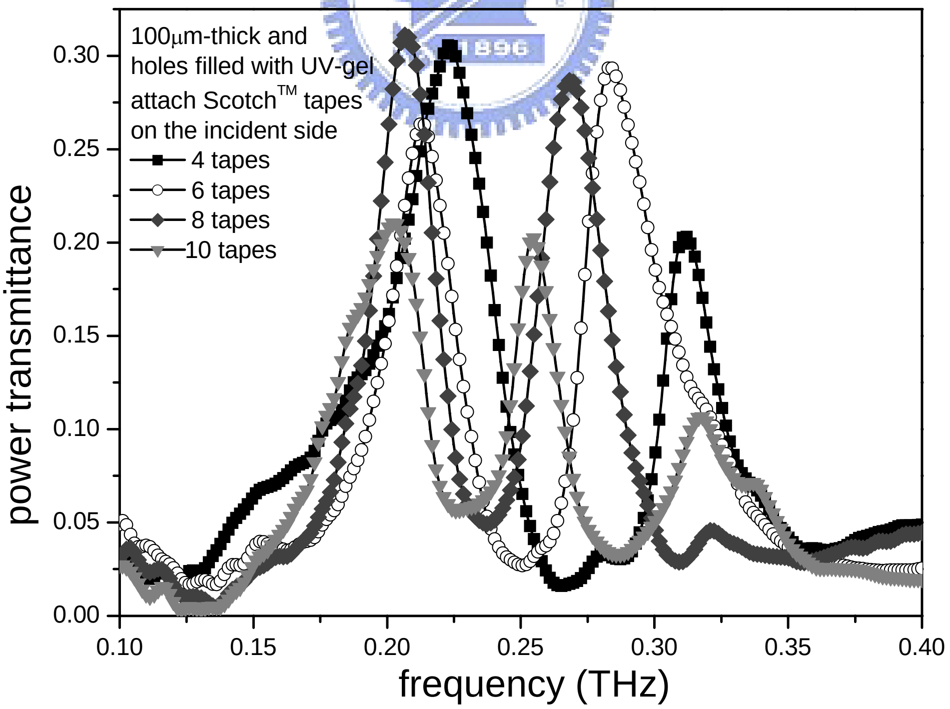

Fig. 4-13 (b) 100μm-thick MHA which holes filled with UV-gel attach different layers of Scotch™ tapes on the incident side. The number of tapes is four, six, eight and ten.

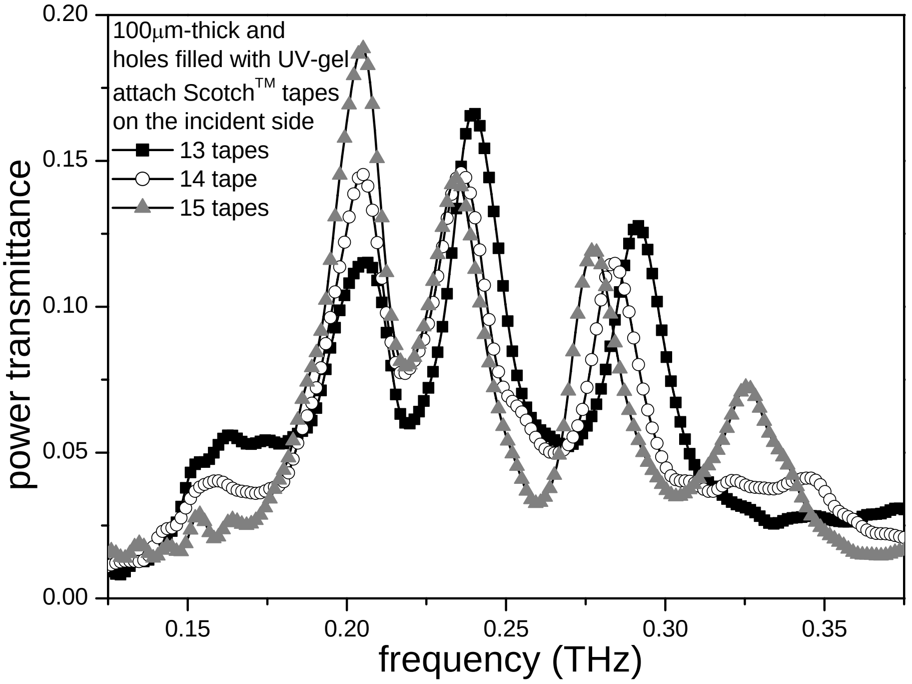

Fig. 4-13 (b) 100μm-thick MHA which holes filled with UV-gel attach different layers of Scotch™ tapes on the incident side. The number of tapes is from thirteen to fifteen.

The same trend is also found in the case of 400μm-thick 2D-MHA filled with UV-gel, as shown in Fig. 4-14. Owing to the original double peaks in 400μm-thick sample, the situation of attaching tapes exhibited more complication.

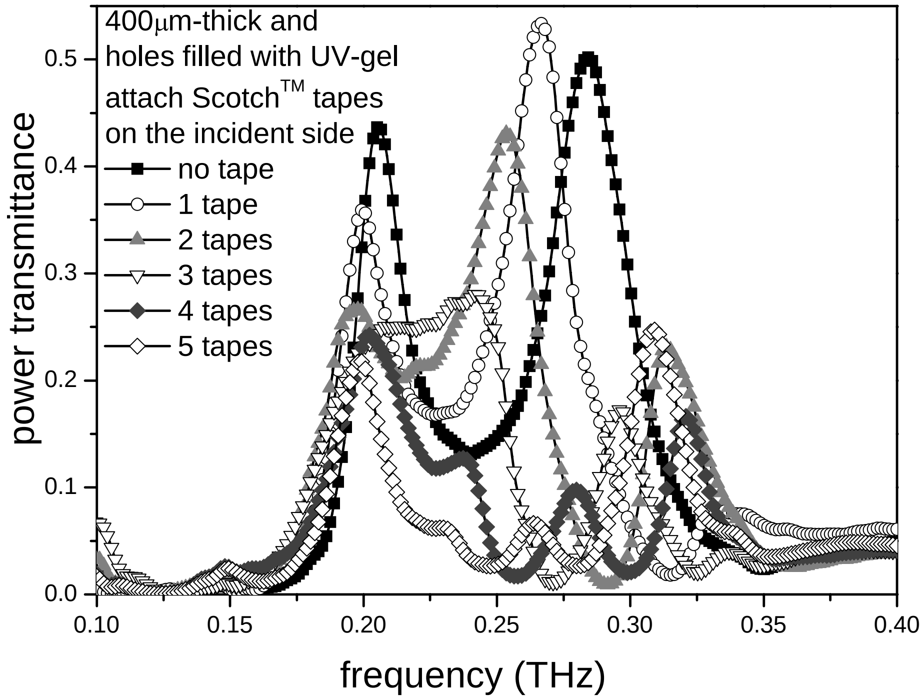

Fig. 4-14 (a) 400μm-thick MHA which holes filled with UV-gel attach different layers of Scotch^{TM} tapes on the incident side. The number of tapes is from zero to five.

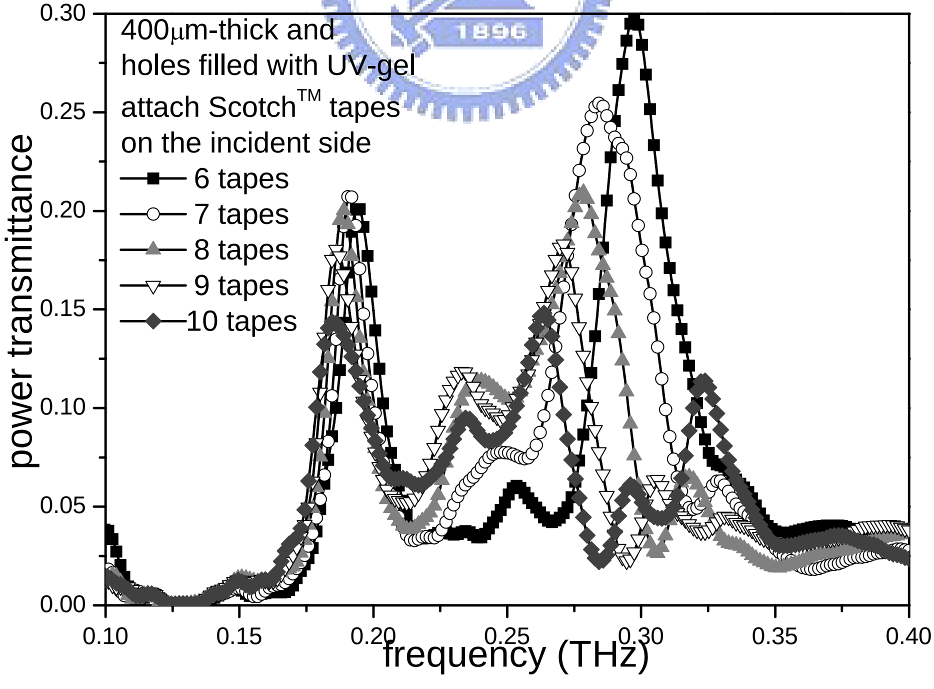

Fig. 4-14 (b) 400μm-thick MHA which holes filled with UV-gel attach different layers of Scotch^{TM} tapes on the incident side. The number of tapes is from six to ten.

4.2.4 Verify the Existence of Surface Plasmons Resonance by Observing the Electric Field in Near-Field Range

It is well-known that an in-plane momentum is needed to modify the incident wave to achieve the enhanced transmission. Either the SPP model, or the model of evanescent wave diffracted by the hole edges [27, 28] can provide such a mechanism. In order to identify these contentions, we have calculated distributions of Ez of the electric field amplitude for 400μm-thick 2D-MHA filled with UV-gel, as shown in Fig. 4-15. The frequencies of the incident THz wave are 0.191THz in Fig. 4-15 (a) and 0.276 THz in Fig. 4-15 (b), respectively. At 0.191 THz, the charge distribution on the side wall of each individual hole shows an anti-symmetric pattern between the top and bottom portion of the hole. At 0.276 THz, the charge distribution is symmetric, and surface waves on the top and bottom are coupled together. We also observe that the CW wave at 0.191THz impinges on the MHA, it will induce the maximum SPPs when a wave crest or trough passes through the medium of the MHA shown in Fig. 4-16 (a). Contrary to the first peak at 0.191THz, the CW wave at 0.276THz impinges on the MHA, it will induce the maximum SPPs when a wave crest arrives at the front surface of the MHA and a wave trough arrives at the back surface shown in Fig. 4-16 (b), and vice versa.

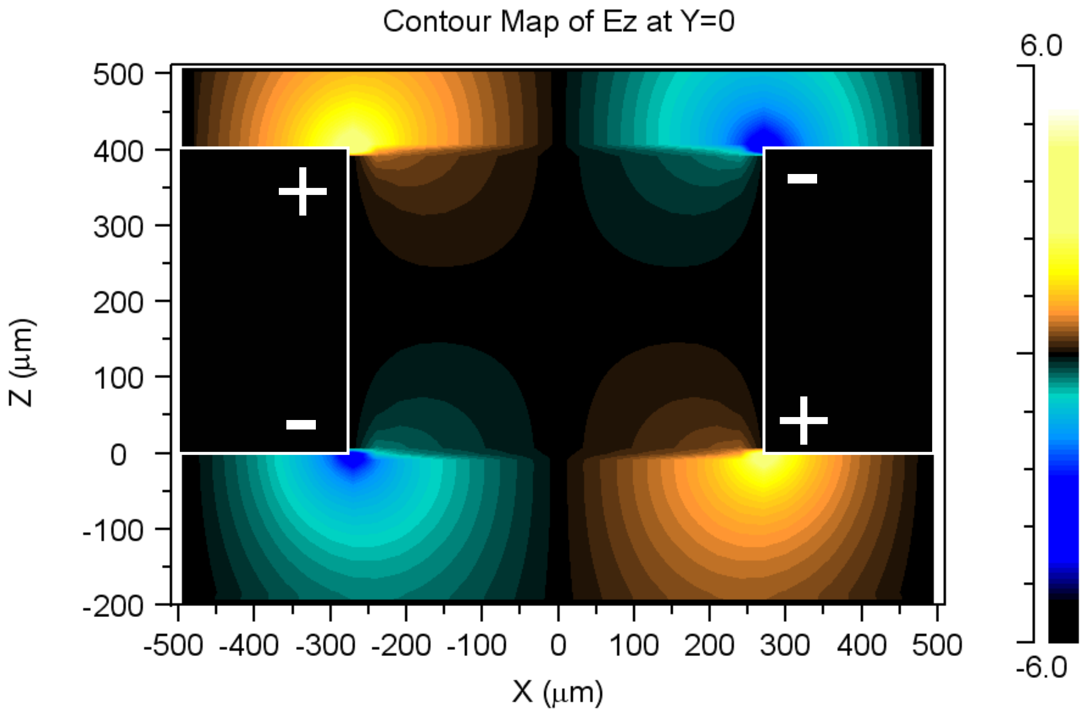

Fig. 4-15 (a) Simulated z component E_z of the electric field amplitude for 100μm-thick MHA filling with UV-gel. The incident CW wave at 0.191THz.

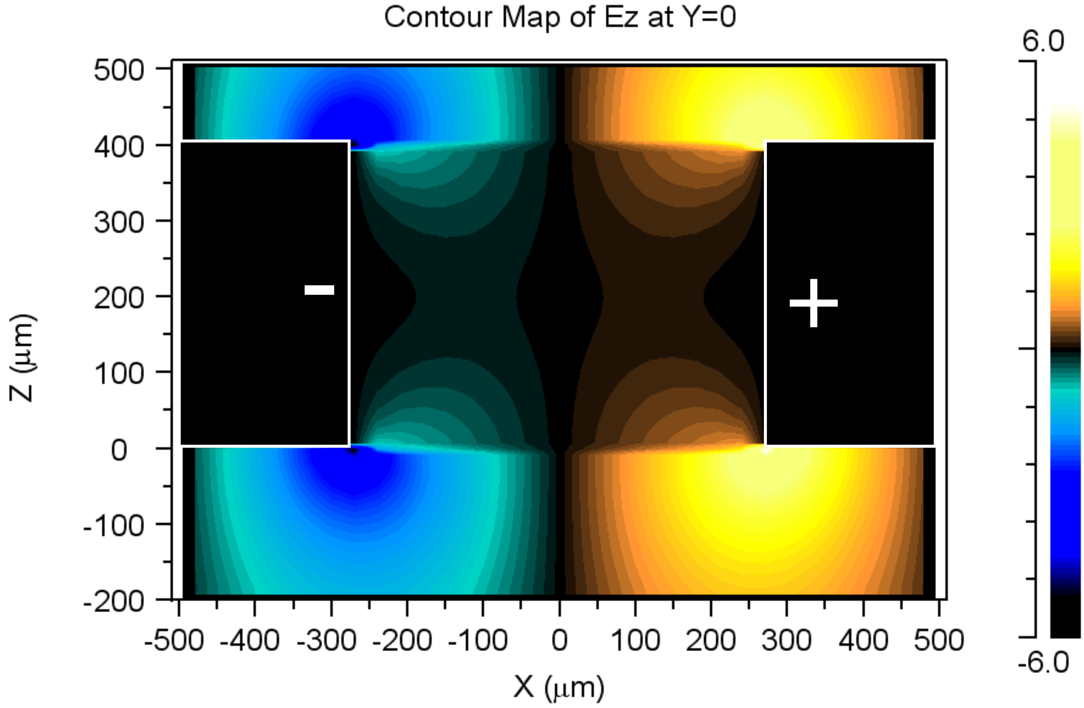

Fig. 4-15 (b) Simulated z component E_z of the electric field amplitude for 100μm-thick MHA filling with UV-gel. The incident CW wave at 0.276THz.

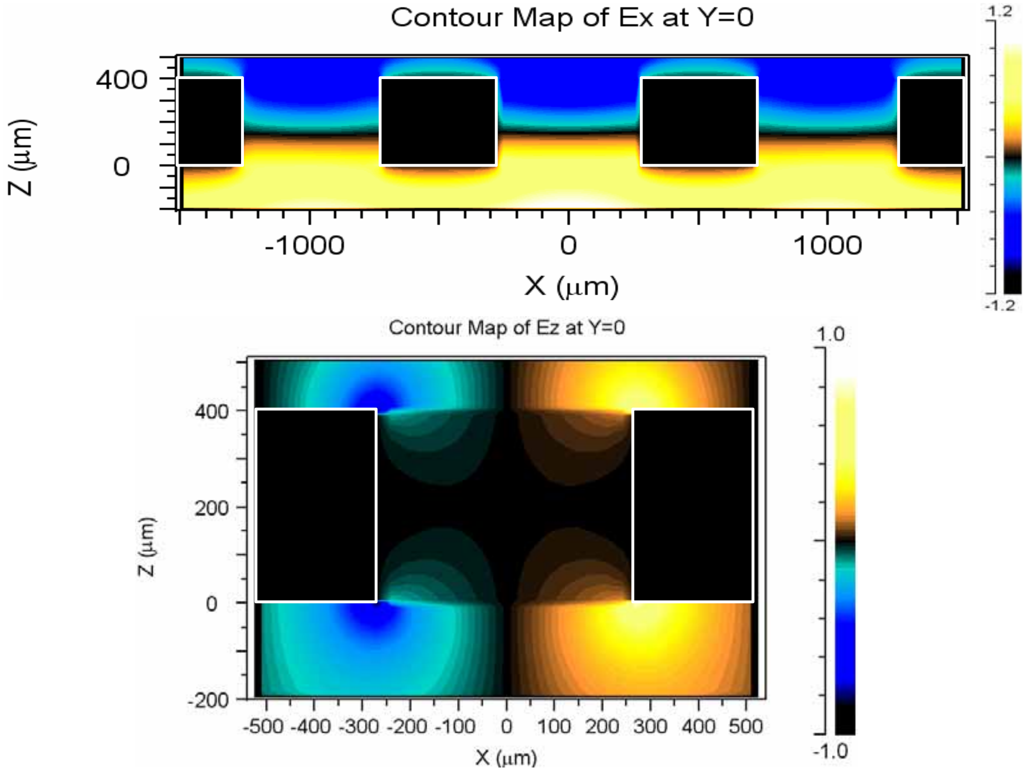

(1)

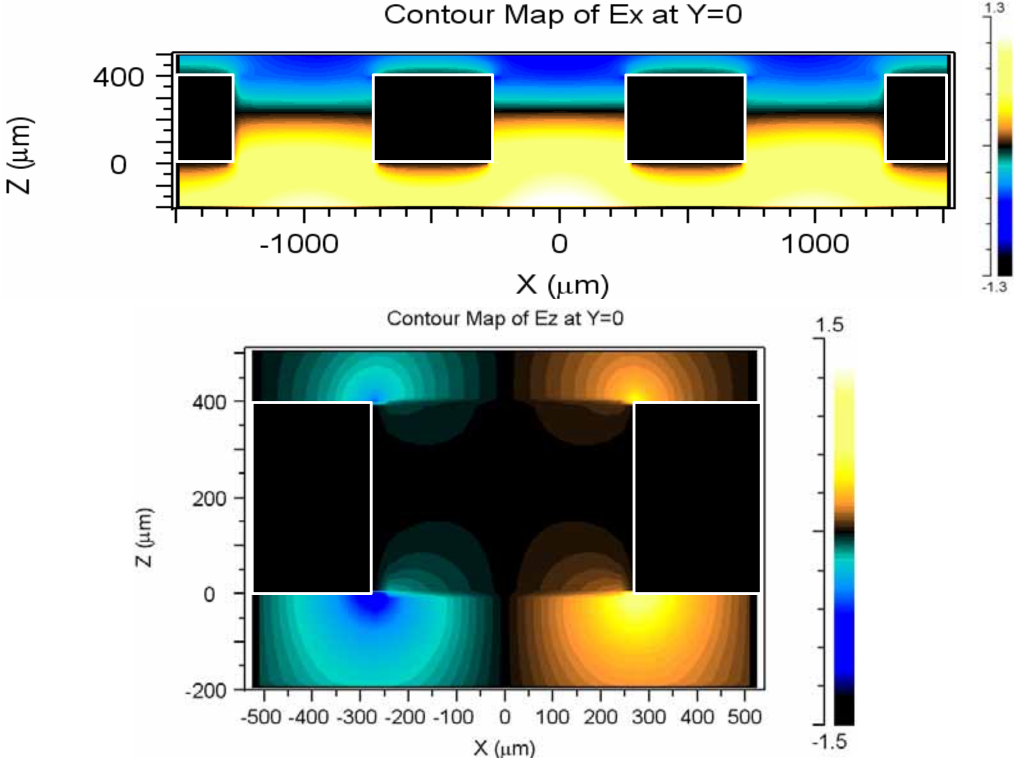

(2)

Fig. 4-16 (a) Simulated E_x and E_z for the 400μm-thick 2D-MHA at 0.191THz. (1)-(6) shows a cycle of propagation.

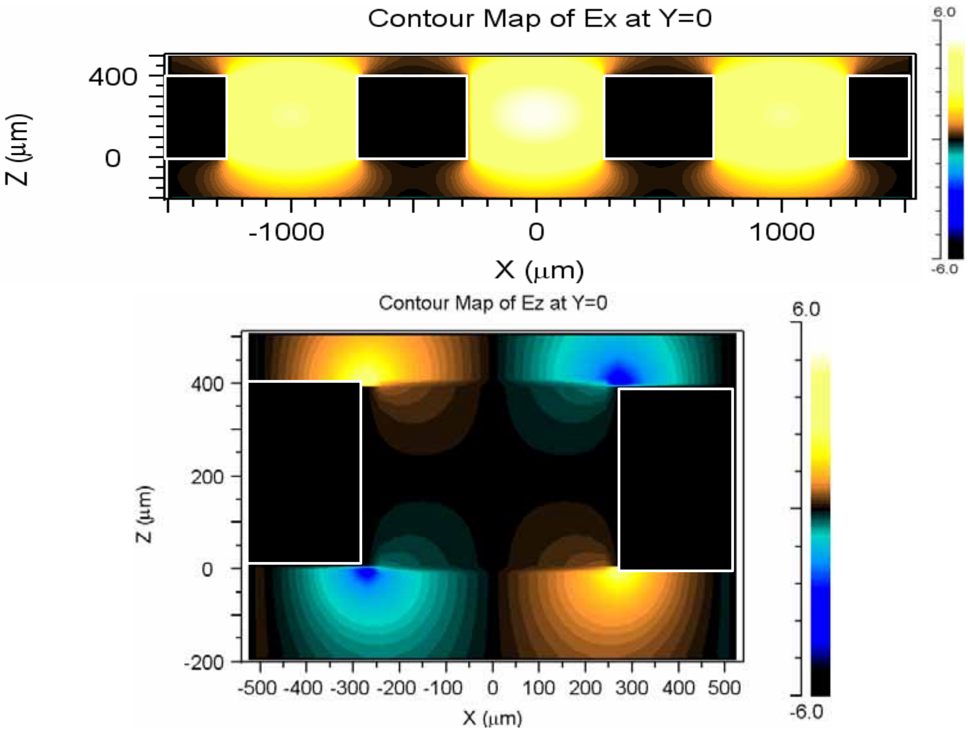

(3)

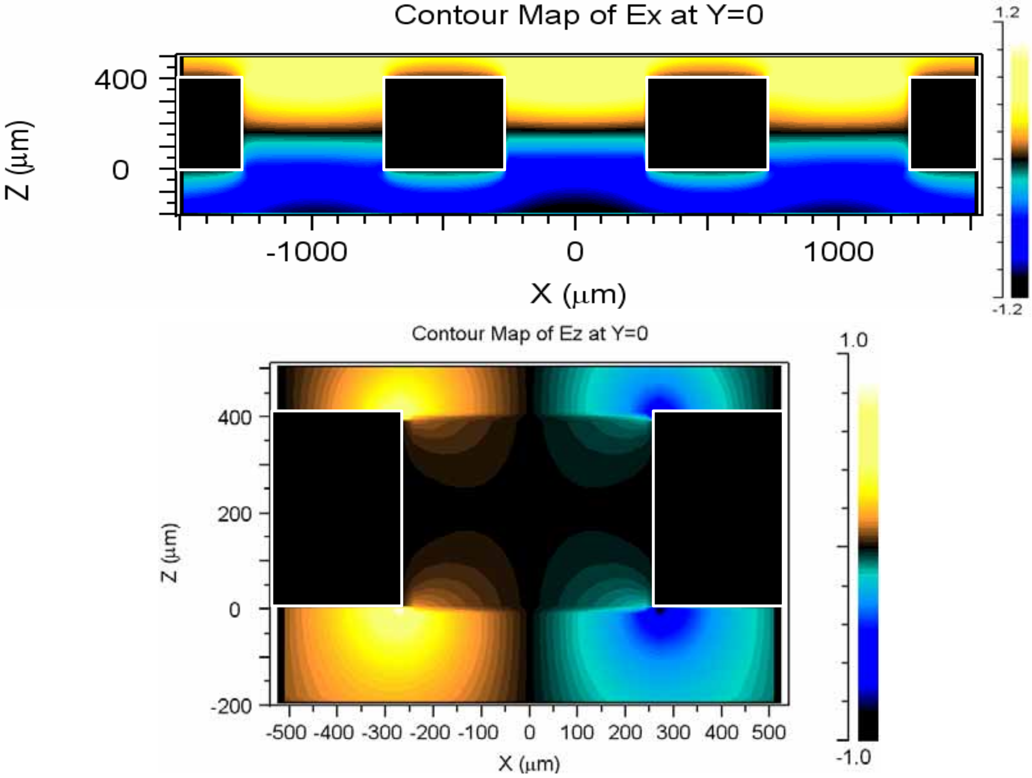

(4)

Fig. 4-16 (a) Simulated E_x and E_z for the 400μm-thick 2D-MHA at 0.191THz. (1)-(6) shows a cycle of propagation.

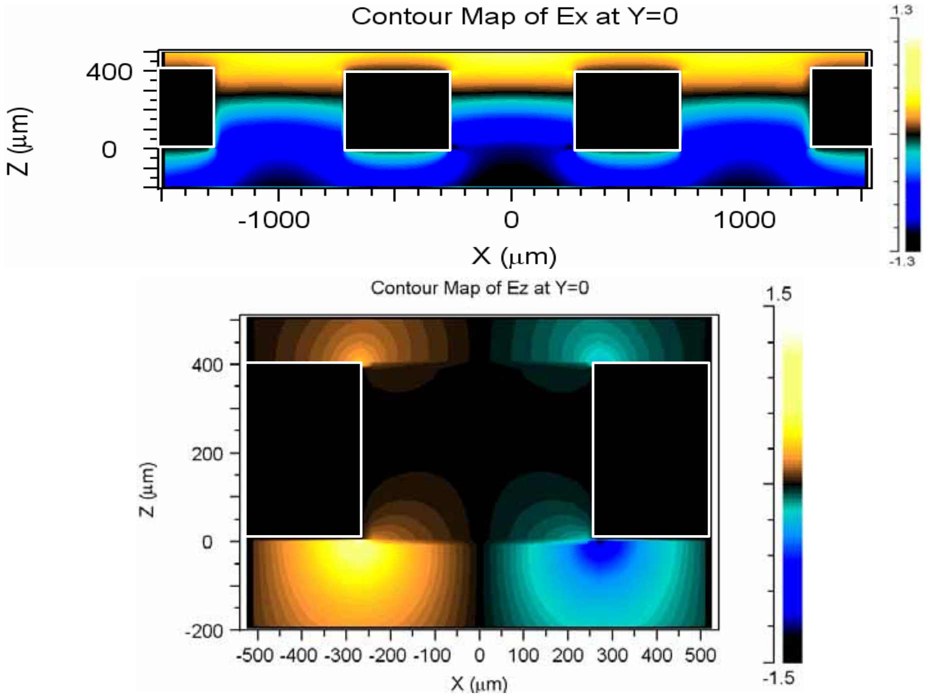

(5)

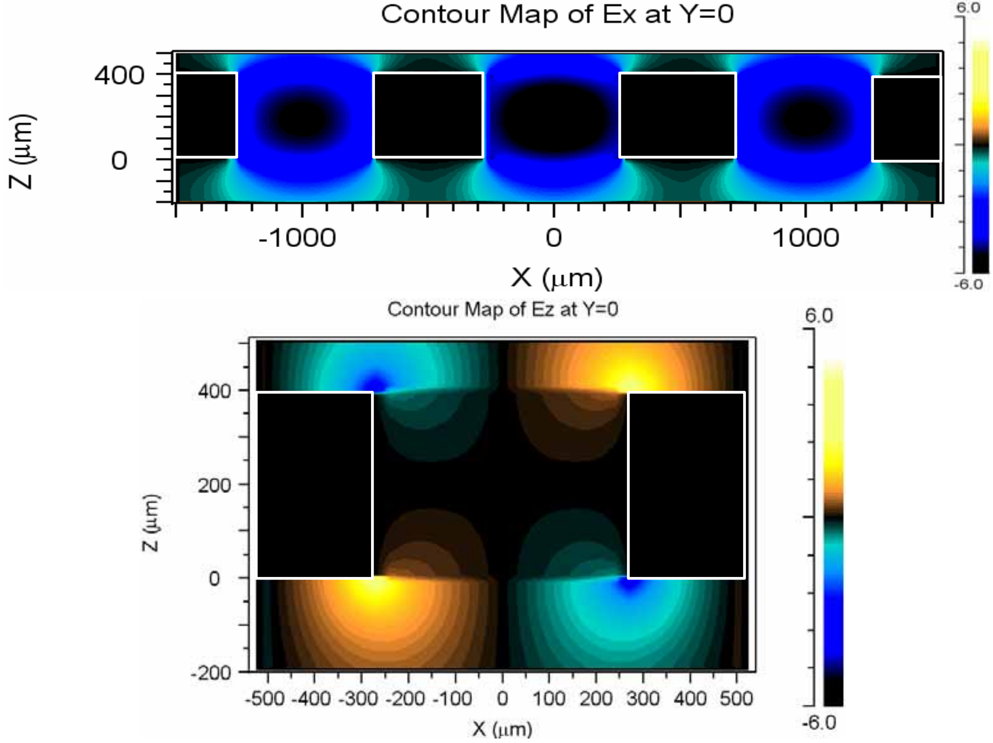

(6)

Fig. 4-16 (a) Simulated E_x and E_z for the 400μm-thick 2D-MHA at 0.191THz. (1)-(6) shows a cycle of propagation.

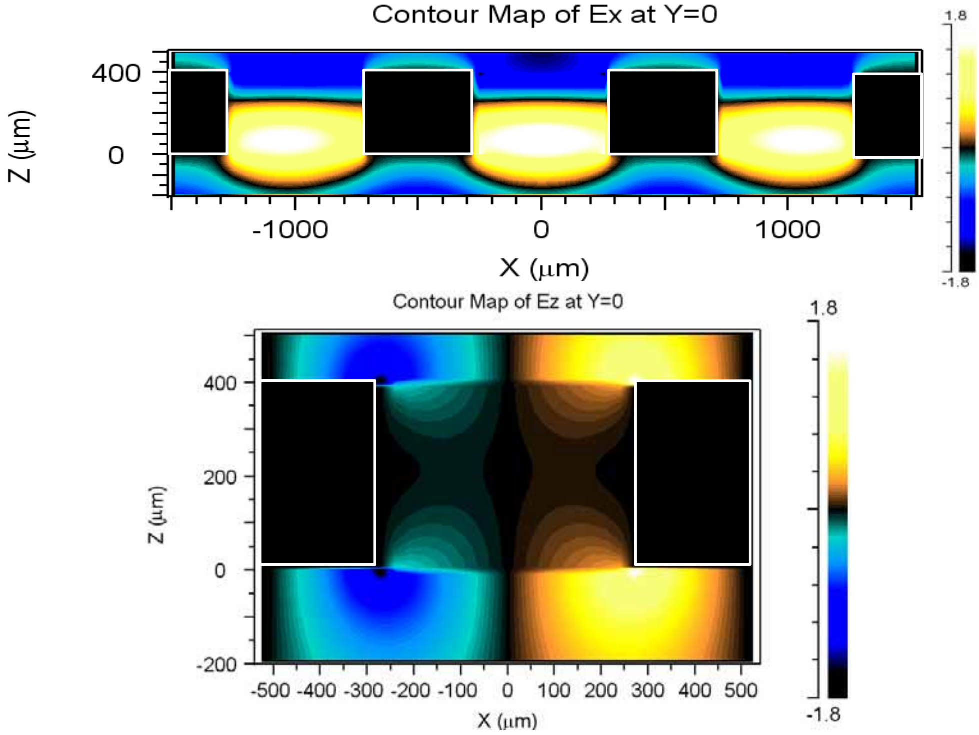

(1)

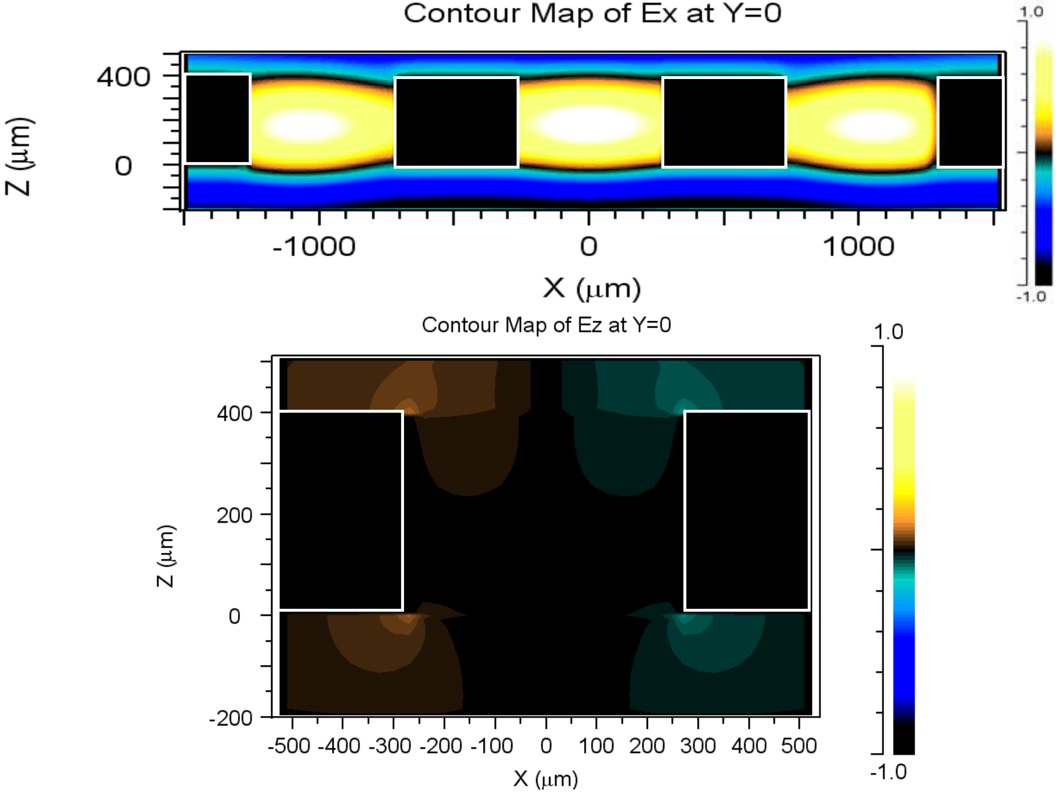

(2)

Fig. 4-16 (b) Simulated E_x and E_z for the 400μm-thick 2D-MHA at 0.276THz. (1)-(6) shows a cycle of propagation.

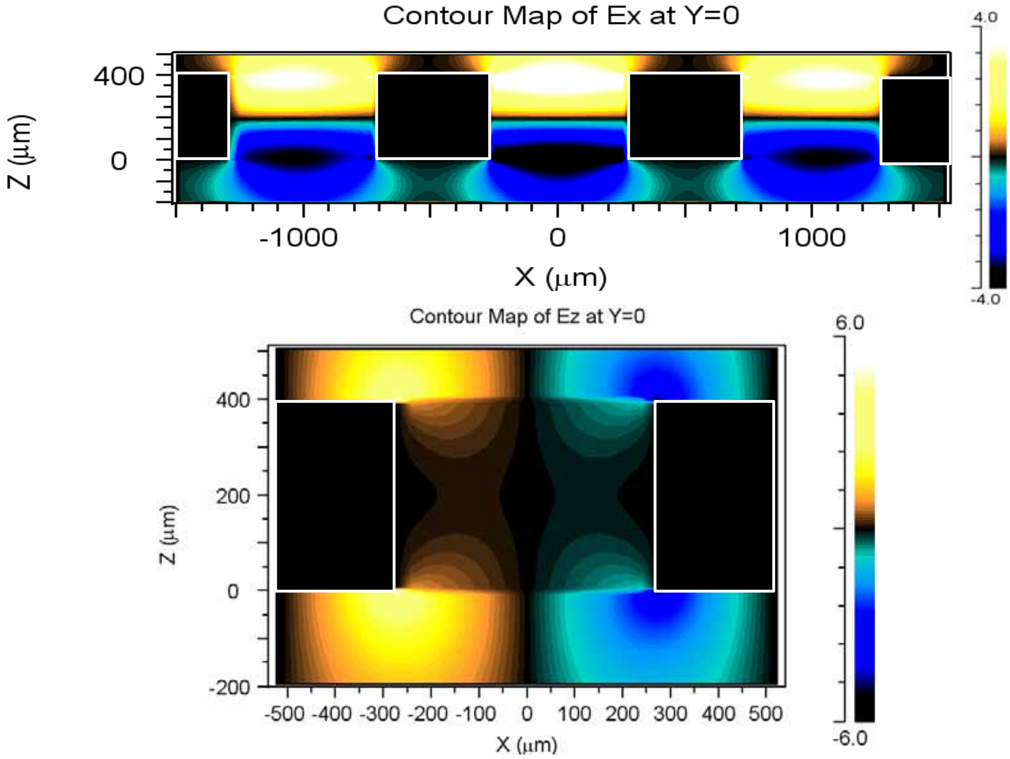

(3)

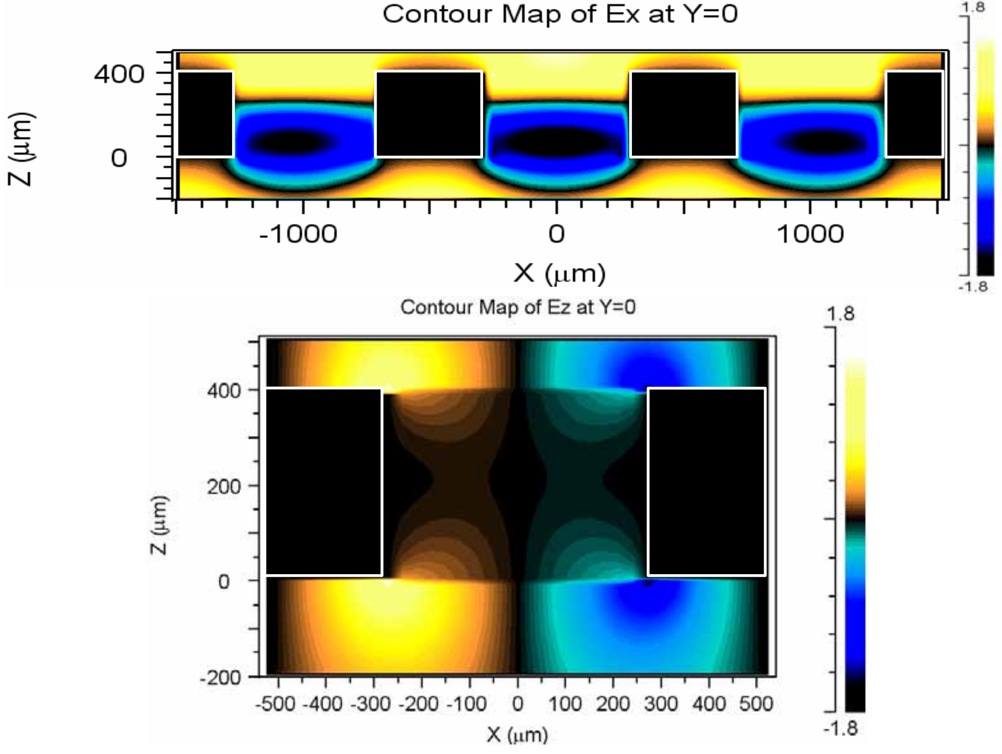

(4)

Fig. 4-16 (b) Simulated E_x and E_z for the 400μm-thick 2D-MHA at 0.276THz. (1)-(6) shows a cycle of propagation.

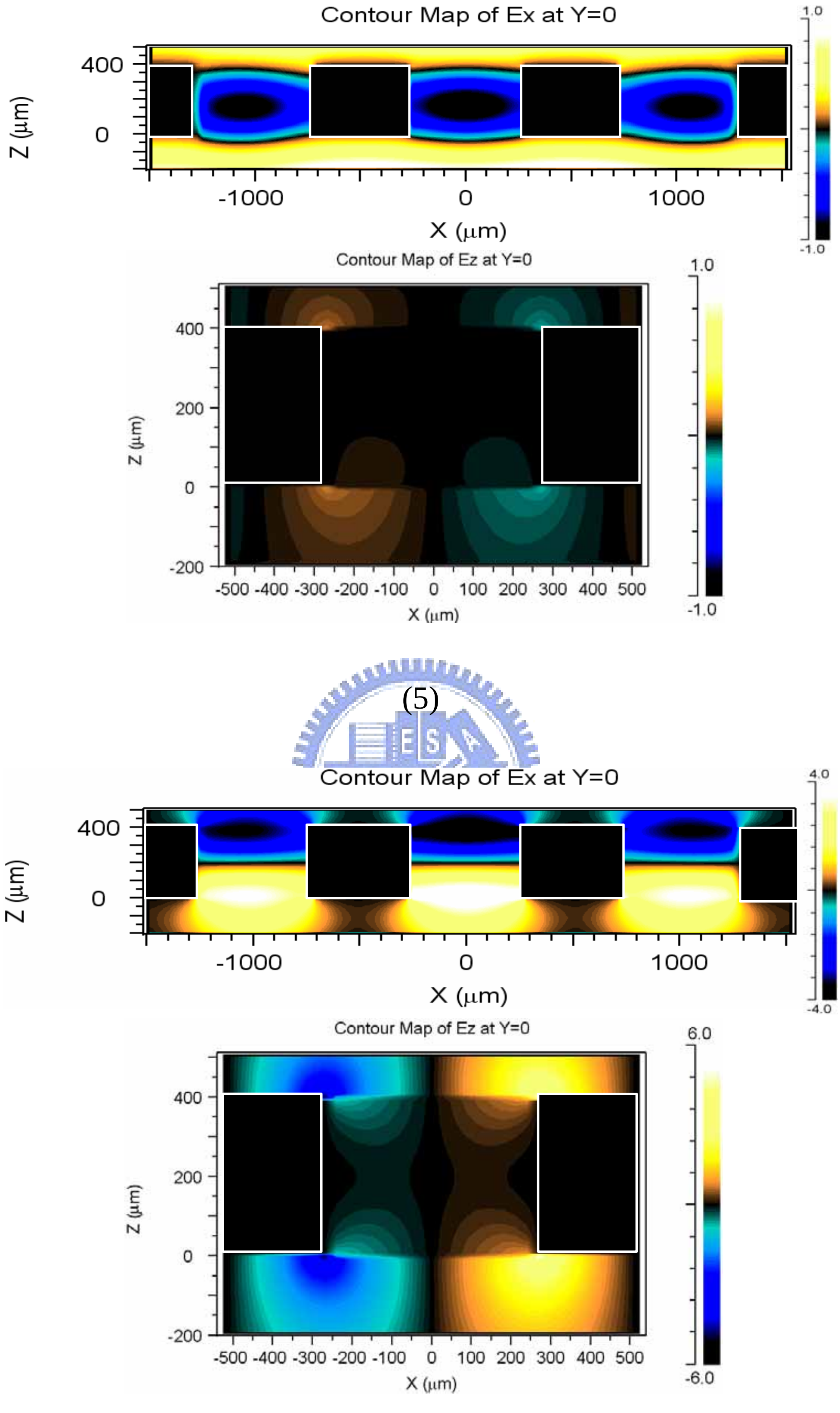

(5)

(6)

Fig. 4-16 (b) Simulated E_x and E_z for the 400μm-thick 2D-MHA at 0.276THz. (1)-(6) shows a cycle of propagation.

The intensity of electric field is normalized to the incident CW wave amplitude. The SPP-like surface wave showing in the simulations of the electric field amplitude agrees with the results studied by Miyamaru et al. [29]. Different SPP modes were also reported by Ebbesen et al. in visible light [30]. However, in our samples, the effective hole depth become deeper and the band-pass frequency region become broader owing to filling UV-gel into the holes of MHAs. Therefore, we consider this is the reason why we can observe both modes at one sample. These might be the causes of multi-peak appearance.

Details of peak frequencies and reasons of the peak drift are still not clear, but it is clear that SPPs play an important role in enhanced transmission characteristics.

5. Conclusions and Future Works

We experimentally and numerically investigate the role of material in the holes on transmission characteristics of the 2D-MHA. New phenomena appeared when holes of the MHA are filled with dielectric material. The effect of filling dielectric material into the holes cannot simply be explained by increased effective hole diameter of the 2D-MHA and SPP model also cannot predict the peak frequencies. When the holes filled with UV-gel, the transmission peak broadened and multi-peak features are observed. The transmittance of the peaks are reduced, but they are still larger than those according to the porosity. Further, with the thickness becomes thinner, all peaks shift to high frequencies and disappear when they approach the diffraction limit. Finally, multi-peaks return to one when the thickness reaches around $100\mu m$. Peaks shift to the left and decrease as the SPP resonances approach the cutoff frequencies when we attach translucent Scotch^{TM} tapes on the incident side of 100μm-thick 2D-MHA filled with UV-gel. Upon increasing the number of the tape, a side peak on the high frequency side grew gradually and red-shifted and for the number of tapes up to fifteen layers, the trend of shift still persists. For deeper holes, SPP can exhibit two distinct modes, coupled and uncoupled types as confirmed in the simulated results for the electric field.

In the future, we want to design a sensor using 2-D MHA for detecting the absorption line.

References

1. Mourou G, “Picosecond microwave pulse generation,” *Appl. Phys. Lett.*, vol. 38, pp. 470-472, 1981.
2. Auston D H, “Picosecond photoconducting Hertzian dipoles,” *Appl. Phys. Lett.*, vol.45, pp. 284-286, 1984.
3. Q. Wu, “Ultrafast electro-optic field sensors”, *Appl. Phys. Lett.*, vol. 68, pp. 1604-1606, 1996.
4. G. Gruner, *Millimeter and submillimeter wave spectroscopy of solids.* Berlin, Springer-Verlag, 1998.
5. Carsten Winnewisser, “Characterization and Application of Dichroic Filters in the 0.1–3-THz Region,” *IEEE Trans. Microwave Theory Tech.*, vol. 48, pp. 744–749, 2000.
6. Dongmin Wu, “Terahertz plasmonic high pass filter,” *Appl. Phys. Lett.*, vol.83, pp. 201-203, 2003.
7. Hideaki Kitahara, “Terahertz wave dispersion in two-dimensional photonic crystals,” *Phys. Rev. B*, vol.64, pp. 042502, 2001
8. T.W. Ebbesen, “Extraordinary optical transmission through sub-wavelength hole arrays,” *Nature.*, vol. 391, pp. 667–669, 1998.
9. M. M. Sigalas, ”Metallic photonic band-gap materials,” *Phys. Rev. B*, vol. 52, pp. 11744-11751, 1995.
10. H. Raether, *Surface Plasmons on Smooth and Rough Surfaces and on Gratings*. Berlin, Springer-Verlag, 1988.
11. Dongxia Qu, “Terahertz transmission properties of thin, subwavelength metallic hole arrays,” *Opt. Lett.*, vol. 29, pp. 896-898, 2004.
12. Masaki Tanaka, “Effect of thin dielectric layer on terahertz transmission characteristics for metal hole arrays,” *Opt Lett.*, to be published. 2005.
13. P. K. Benicewicz, ” Scaling of terahertz radiation from large-aperture biased photoconductors,” *J. Opt. Soc. Am. B*, vol. 11, pp. 2533–2546,

1994.

14. Zhisheng Piao, “Carrier Dynamics and Terahertz Radiation in Photoconductive Antennas,” *Jpn. J. Appl. Phys.*, vol. 39, pp. 96–100, 2000.
15. P. Uhd Jepsen, “Generation and detection of terahertz pulses from biased semiconductor antennas,” *J. Opt. Soc. Am. B*, vol. 13, pp. 2424–2436, 1996.
16. S. Nashima, “Temperature dependence of optical and electronic properties of moderately doped silicon at terahertz frequencies,” *J. Appl. Phys.*, vol. 90, pp. 837–842, 2001.
17. David K. Cheng., *Field and wave electromagnetics, 2nd*. New York, Addison-Wesley, 1989.
18. William L. Barnes, “Surface plasmon subwavelength optics,” *Nature.*, vol. 424, pp. 824–830, 2003.
19. Hua Cao, “Resonantly enhanced transmission of terahertz radiation through a periodic array of subwavelength apertures,” *Opt. Express.*, vol. 12, pp. 1004–1010, 2004.
20. Allen Taflove, *Computational Electrodynamics: The Finite-Difference Time-Domain Method, 2nd*. London, Artech House, 2000.
21. K. S. Yee, “Numerical solution of initial boundary value problems involving Maxwell’s equations in isotropic media,” *IEEE Trans. Antennas Propagat.*, vol. AP-14, pp. 302, 1966.
22. Dennis M. Sullivan, *Electromagnetic Simulation Using the FDTD Method*. New York, IEEE Microwave Theory and Techniques Society, Sponsor, 2000.
23. M. A. Ordal, “Optical properties of the metals Al, Co, Cu, Au, Fe, Pb, Ni, Pd, Pt, Ag, Ti, and W in the infrared and far infrared,” *Appl. Opt.*, vol. 22, pp. 1099–1120, 1983.
24. Dongfeng Liu, “Carrier dynamics of terahertz emission from low-temperature-grown GaAs,” *Appl. Opt.*, vol. 42, pp. 3678–3683, 2003.

25. Martin van Exter, “Terahertz time-domain spectroscopy of water vapor,” *Opt. Lett.*, vol. 20, pp. 1128-1130, 1989.
26. Eugene Hecht, *Optics 3rd*. Addison-Wesley, 1998.
27. Marek W. Kowarz, “Homogeneous and evanescent contributions in scalar near-field diffraction,” *Appl. Opt.*, vol. 17, pp. 3055–3063, 1995.
28. Henri J. Lezee, “Diffracted evanescent wave model for enhanced and suppressed optical transmission through subwavelength hole arrays,” *Opt. Express.*, vol. 12, pp. 3629–3651, 2004.
29. Fumiaki Miyamaru, “Anomalous terahertz transmission through double-layer metal hole arrays by coupling of surface plasmon polaritons,” *Phys. Rev. B*, vol.71, pp. 165408, 2005.
30. A. Degiron, “Effects of hole depth on enhanced light transmission through subwavelength hole arrays,” *Appl. Phys. Lett.*, vol. 81, pp. 4327-4329, 2002.